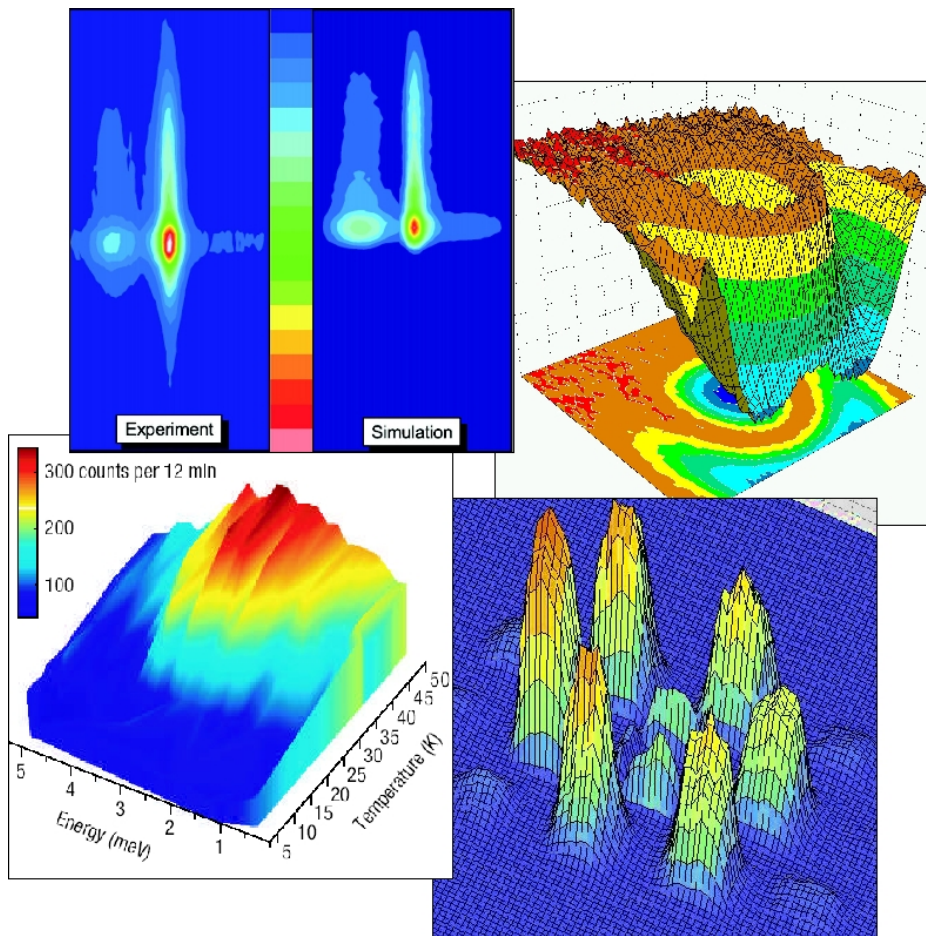




Institute for
Experimental Physics E21

Annual Report 2005
Annual Report 2005



Cover page

- Top/left: Experimental and simulation data of the neutron distribution in the focal plane of an elliptically shaped neutron guide (section 7.4).
- Top/right: DC/RF-amplitude scan at an RF-frequency of 109 kHz of the NRSE coils of the MIEZE setup at MIRA (section 3.1).
- Bottom/left: Temperature and energy dependence of the low energy Villain mode in CsMnBr₃ (Braun et al., *Nature Physics* **1**, 159 (2005)).
- Bottom/right: SANS image of the sixfold symmetry of the Niob flux line lattice measured with a 2-dimensional PSD (section 1.10).

Annual Report 2005

of the Institute for Experimental Physics E21
Prof. Dr. P. Böni
Technical University Munich

Annual Report 2005
of the Institute for Experimental Physics E21
published: Feb. 2006
Layout by Nikolas Arend, Florian Grünauer
Edited by Nikolas Arend
<http://einrichtungen.physik.tu-muenchen.de/E21/>

Technical University Munich
James-Franck-Straße
85747 Garching, Germany

Phone: +49-89-289-14711
Fax: +49-89-289-14713

Copyright:
Inquiries about copyright and reproduction etc.
should be addressed to the authors.

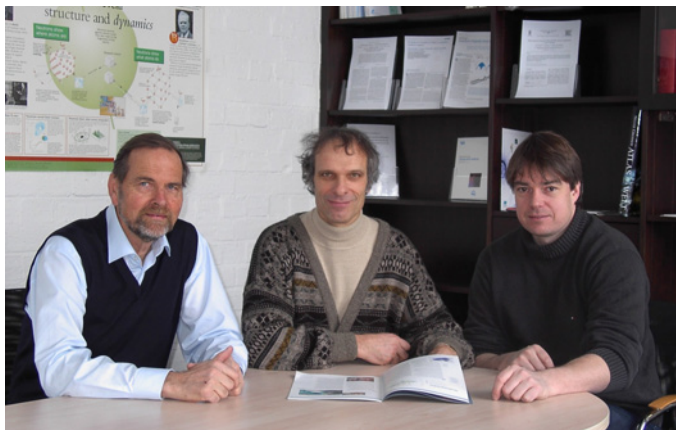
Contents

Preface	1
1 Magnetism and Superconductivity	3
1.1 Reduction of the ordered magnetic moment in YMnO_3 with hydrostatic pressure	4
1.2 Upward renormalization of CsVBr_3 in the disordered phase	5
1.3 Singlet formation in $\text{Ca}_{0.83}\text{CuO}_2$	6
1.4 Spin wave damping in the isotropic Heisenberg antiferromagnet RbMnF_3	7
1.5 The 4f multiplet in the Antiferro-Quadrupolar compound TmTe	8
1.6 The special features of the ground state in heavy fermion CeAl_3	9
1.7 Inelastic neutron scattering study of polycrystalline chromium	10
1.8 Magnetic-field induced instability in the A-Phase of MnSi : Bulk and SANS measurements	11
1.9 Low-energy magnetic excitations in Mn-doped single-crystal Cr	12
1.10 The flux line lattice in Niobium - measurements with polarised and unpolarised neutrons	13
2 Multilayers and Interfaces	15
2.1 Soft X-ray investigations of exchange coupled FM/AM bilayers	16
2.2 Polarized neutron reflectometry on Fe/Cr multilayers at MIRA	17
2.3 Correlation of magnetic domains in FM/AF/FM trilayers probed by off-specular PNR	18
3 Fundamental Physics	19
3.1 First MIEZE and Multi-MIEZE experiments at MIRA	20
4 Positron Physics	21
4.1 First Experiments at the Positron Beam Facility NEPOMUC	22
4.2 Positron remoderation facility for the slow positron beam at FRM-II	23
4.3 Measurements on Mg-Alloys with the Coincident Doppler Broadening Spectrometer CDBS	24
4.4 PAES - Positron Annihilation induced Auger Electron Spectroscopy	25
4.5 Time of flight spectroscopy of positron induced Auger electrons	26
5 Radiography and Tomography	27
5.1 Neutron phase contrast imaging at ANTARES	28
5.2 A study of oil lubrication in a rotating engine using stroboscopic neutron imaging	29
5.3 Multiple radiation measurements at the radiography facility ANTARES	31
5.4 Small-angle scattering effects in neutron radiography and tomography	34
6 Reactor Physics	37
6.1 Heavy Ion Irradiation of U-Mo/Al Dispersion fuel	38
7 Instrument Development	39
7.1 MuPAD - Spherical Neutron Polarimetry at SINQ and FRM-II	40
7.2 Spherical neutron polarimetry data analysis with FullProf: soon a reality	42
7.3 MuPAD - First tests and results	43
7.4 First Measurements with an Elliptically Shaped Neutron Guide	44
7.5 Simulations for a new neutron guide switch for the instrument MIRA	45
7.6 First Spin Echo Signal at RESEDA	46
7.7 MIRA – The beam line for very cold neutrons at the FRM-II	47
7.8 Multiple Small Angle Neutron Scattering	48

8	Activities 2005	49
8.1	Lectures, Courses and Seminars	50
8.2	Seminar "Neutronen in Industrie und Forschung" 2005	51
8.3	Workshops 2005	52
8.4	Publications 2005	53
8.5	Conference, Workshop and Seminar Contributions 2005	55
8.6	Filed Patents 2005	58
8.7	Committee Memberships	58
8.8	Accomplished PhD Theses	58
8.9	Accomplished Master's Theses	58
8.10	Accomplished Bachelor Theses	58
8.11	E21 Members	59
8.12	Associated Members at FRM-II	60
8.13	Guests	60
8.14	Guest Scientists	60
8.15	Guided Tours at FRM-II	60
	Photo of the E21 group	60
	E21 gallery	62

Preface

The year 2005 has been a turning point for E21, following a long spell of technical developments at FRM-II caused by the politically delayed start-up of the FRM-II and then the lack of funding and manpower for the scientific program. We are very glad that from a scientific point of view the year 2005 has finally been a very rewarding year. With the regular operation of the neutron source Heinz Maier-Leibnitz (FRM-II), we enjoyed for the first time the opportunity to perform experiments at our four beam lines MIRA, RESEDA, ANTARES and NEPOMUC in our immediate neighborhood! It is no surprise that due to the excellent construction of our beam lines at FRM-II we have been able to make major contributions to the success of FRM-II.



- Basic research: Observation of a new magnetic phase in the weak itinerant ferromagnet MnSi. The results were presented as an invited talk at the International Conference on Neutron Scattering ICNS'2005 in Sidney.
- Applied research: Real time imaging of running combustion engines at the radiography station ANTARES. These impressive results of the institute E21 are extensively used by many institutions, including the FRM-II for advertising neutron sources.
- Neutron instrumentation: Realization of an elliptic guide system proving the superior performance of non-linearly tapered neutron optics for the transport and the focusing of neutrons. Elliptic optics will be installed extensively at the new spallation sources SNS in the US and J-PARC in Japan.
- Polarization analysis: Fabrication of MuPAD, a device for performing three-dimensional polarization analysis in non-collinear magnetic systems. It was considered as one of the highlights within the European project on spin turning devices.
- Fundamental physics: Realization of the first double-MIEZE signal at the beamline MIRA, opening the way for fundamental studies of the neutron and the investigation of slow dynamic processes.
- Positron physics: Proof of principle that it is now possible to measure the concentration of the various constituents at the surface of Mg-alloys.

Following the rapid appointment of Christian Pfeleiderer at the end of 2004 we are very happy that he stayed in Munich despite attractive offers from other places. Along with Christian Pfeleiderer's decision, the magnetism section of E21 is steadily becoming more active having been joined by Dr. Philipp Niklowitz and a few diploma and PhD students. During 2005 a laboratory for low temperature transport and magnetization studies at high magnetic fields and high pressures was put into operation. At FRM-II first neutron experiments have been carried out with the help of high-pressure clamp cells now available at E21. In particular, preparations have been made, so that the crystal growth laboratory and the high magnetic field / ultralow temperature laboratory will become operational already during 2006. We are in turn looking forward to a wide range of experimental studies on the magnetism of intermetallic compounds.

After almost seven years comprising the decisive time of licensing procedure and start-up of the FRM-II, Klaus Schreckenbach has handed over the responsibility as Technical Director of the FRM-II to his successor Ingo Neuhaus by the end of 2005. Klaus Schreckenbach will move now also physically to the E21 institute and is looking forward with excitement to his new working field. His research interest is focussed on neutron particle physics and on physics and developments at the positron source NEPOMUC of E21 at the FRM-II.

The results of our research have been published in various refereed journals including Nature Physics and were presented at many conferences and workshops. Two members of E21 submitted a patent for the fabrication of a new type of fuel plate for research reactors. During 2005, four PhD theses, five master's theses, and one bachelor thesis have been completed. We are very happy that all candidates have found attractive new positions. Major social highlights have been a day of skiing in Achenkirch on Feb. 17 2005 and an evening of bowling on Dec. 19 2005 in the Bürgerhaus in Garching. We wish to thank Barbara Russ and Sylvia Jones for organizing these events and their efforts to organize the enjoyable morning coffee round and other get-togethers of E21.

Garching, January 2006

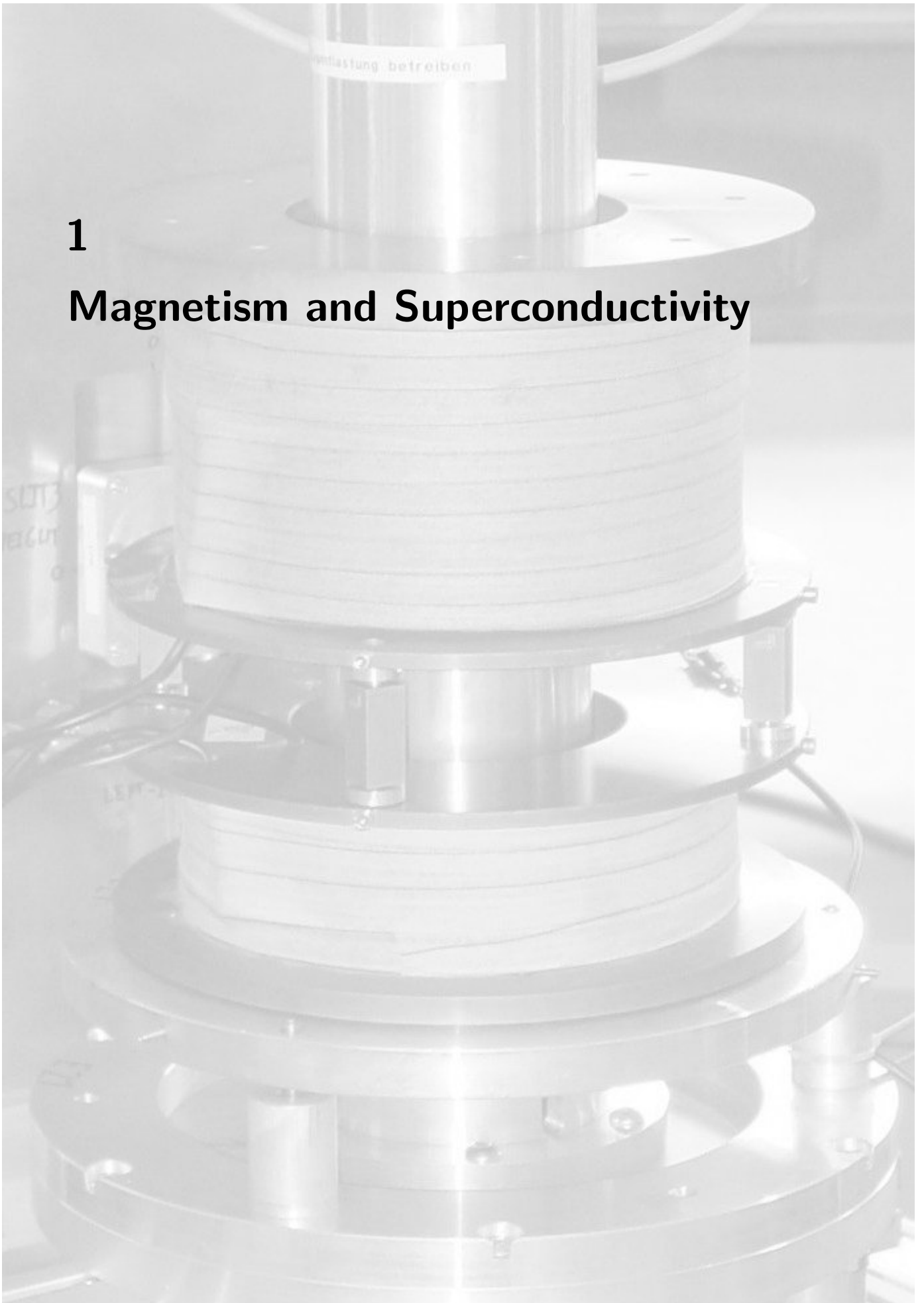
Peter Böni

Christian Pfeleiderer

Klaus Schreckenbach

1

Magnetism and Superconductivity



1.1 Reduction of the ordered magnetic moment in YMnO₃ with hydrostatic pressure

M. Janoschek^{1, 2}, B. Roessli², L. Keller², S. Gvasaliya², K. Conder³, E. Pomjakushina³

¹Physics Department E21, Technical University Munich, 85747 Garching, Germany

²Laboratory for Neutron Scattering ETHZ & Paul Scherrer Institut, CH-5232 Villigen PSI, Switzerland

³Laboratory for Developments and Methods, Paul Scherrer Institut, 5232 Villigen PSI, Switzerland

Yttrium manganite belongs to the the family of rare-earth manganites $RMnO_3$ (R = rare earth element) which have both ferroelectric and magnetic order. These compounds crystallize in the hexagonal space-group $P6_3$ cm below the paraelectric-ferroelectric phase transition ($T_C \approx 900$ K). The six Mn^{3+} magnetic moments in the unit cell are located in planes separated by ≈ 7 Å along the hexagonal axis. Because of the large distance between adjacent triangular layers, $YMnO_3$ is a good candidate for a geometrically frustrated 2D antiferromagnet although small exchange interactions along the hexagonal axis drives magnetic ordering at $T_N \approx 70$ K. The coupling between adjacent layers is reported to be antiferromagnetic and the ordered magnetic moment of the Mn-ions was found to be $\mu = 2.9\mu_B$ at saturation [1]. The $RMnO_3$ ferroics have received renewed interest since anomalies in the dielectric constant ϵ are found at the magnetic ordering temperature T_N [2] indicating a strong coupling between ferroelectric and magnetic properties. The origin of the magnetoelectric (ME) effect in these compounds is still not fully understood but spin-lattice interaction might play an important role in these materials. For example, anomalies of the structural parameters were reported at T_N that yields evidence that strong coupling between spin and lattice degrees of freedom is at the origin of the ME effect in $YMnO_3$ [3, 4].

In order to get more insight into the coupling between spin and structural parameters and their possible relationship on the magnetic and dielectric properties of ferroic materials, we investigated the influence of hydrostatic pressure on the magnetic ordering in $YMnO_3$ at the cold neutron powder diffractometer DMC located at the neutron spallation source SINQ.

A first series of measurements were done at ambient pressure in the temperature range $1.5 \text{ K} < T < 300 \text{ K}$. The neutron diffraction patterns were analyzed with the Rietveld method [5] implemented in the program FullProf [6]. The value of the ordered magnetic moment at $T = 1.5 \text{ K}$ is $3.09(15)\mu_B$, in good agreement with the results of reference [1]. The temperature dependence of the staggered magnetization is shown in Fig.1. The applied pressure was 7.8 kbar at $T = 1.5 \text{ K}$ and increased only slightly to 8.3 kbar up to the antiferromagnetic transition temperature $T_N \approx 70 \text{ K}$ of $YMnO_3$. Least-square refinements of the diffraction pattern at 1.5 K yielded best agreement factors when the same magnetic structure as for ambient pressure was assumed, namely (magnetic) $R_{Bragg} = 9.95$ and $\chi^2 = 4.73$, respectively. Hence, the spin arrangement of $YMnO_3$ is not modified by hydrostatic pressure up to $p \approx 8$ kbar. However, the magnitude of the ordered magnetic moments is significantly reduced from $\mu \approx 3\mu_B$ at ambient pressure to $\mu = 2.50(5)\mu_B$ at $p \approx 8$ kbar. The temperature dependence of the ordered magnetic moment is shown in Fig. 1. Although from neutron powder measurements it is difficult to determine the value of T_N precisely, we conclude from our data that the difference of T_N is less than $\approx 5 \text{ K}$ at $p = 8$ kbar as compared to

ambient pressure.

A possible model to describe the magnetic and ferroelectric properties of ferroic materials was proposed by Gong *et al.* [7] that includes antiferromagnetic Heisenberg exchange interactions and a double well potential for the lattice displacements giving rise to ferroelectricity. In that approach, the Néel temperature is reduced by the ME-coupling, but the value of the magnetic moment $\langle S^z \rangle$ in the ground-state is essentially unaffected [8]. Therefore the model does not explain our results for $YMnO_3$. The reduction of the ordered magnetic moment in $YMnO_3$ by application of hydrostatic pressure suggest that coupling between the size of the magnetic moment and the volume of the unit cell is important in ferroic materials, especially as the magnetic structure does not change. The application of hydrostatic pressure increases the spin fluctuations in $YMnO_3$ and enhances the 2D character of the magnetic properties of that compound. We suggest that application of pressure leads to a renormalisation of the temperature dependence of the staggered magnetisation, i.e. the strain influences the sublattice magnetisation [9]. The complete work was published in [10].

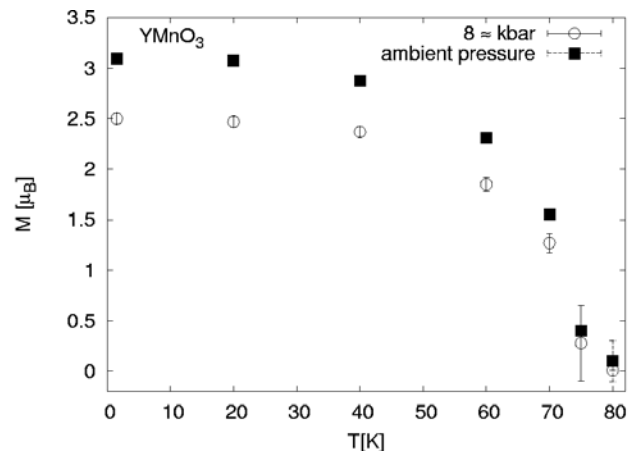


Figure 1: Temperature dependence of the magnitude of the Mn magnetic moments for ambient pressure and $p \approx 8$ kbar.

References

- [1] A. Munoz, M. T. Casais, J. A. Alonso, M. J. Martynez-Lope, J. L. Martynez, and M. T. Fernandez-Dyaz. *Phys. Rev. B*, 62(14), 2000.
- [2] Z. J. Huang, Y. Cao, Y. Y. Sun, Y. Y. Xue, and C. W. Chu. *Phys. Rev. B*, 56(5):2623–2626, 1997.
- [3] S. Lee, A. Pirogov, J. H. Han, J.-G. Park, A. Hoshikawa, and T. Kamiyama. *Phys. Rev B*, 71(180413), 2005.
- [4] P. A. Sharma, J. S. Ahn, S. Park, S. B. Kim, S. Lee, J. G. Park, S. Guha, and S. W. Cheong. *Phys. Rev. Lett*, 93(177202), 2004.
- [5] H. M. Rietveld. *J. Appl. Crystallogr.*, 2:65, 1969.
- [6] J. Rodriguez-Carvajal. *Physica B*, 192:55, 1993.
- [7] S. J. Gong and Q. Jiang. *J. Magn. Magn. Mater.*, 285(3):367, 2005.
- [8] C. Zhong and Q. Jiang. *Solid State Commun.*, 122(11):601, 2002.
- [9] D. C. Mattis and T. D. Schultz. *Phys. Rev.*, 129:75, 1963.
- [10] M. Janoschek, B. Roessli, L. Keller, S. Gvasaliya, K. Conder, and E. Pomjakushina. *J. Phys.: Condens. Matter*, 17:425–430, 2005.

1.2 Upward renormalization of CsVBr₃ in the disordered phase

V. Kargl¹, P. Böni¹, B. Roessli², K. Krämer³

¹Physics Department E21, Technical University Munich, 85747 Garching, Germany

²Paul Scherrer Institut, 5232 Villigen PSI, Switzerland

³Universität Bern, 3000 Bern 9, Switzerland

A change in magnetic long range properties of a system to one dimensional behavior can be evoked by an external parameter such as pressure, doping or temperature. In this sense, increasing temperature destroys in ABX_3 compounds the magnetic correlations perpendicular to the preferred spin coupling and only the exchange measured along one direction holds. We report on CsVBr₃ ($S = 3/2$) that is expected to feature quasi 1D behavior when crossing its Néel temperature of 20.4 K [1]. The compound belongs to the hexagonal space group $Pm\bar{3}/mmc$ with the lattice constants $a = b = 7.57 \text{ \AA}$ and $c = 6.32 \text{ \AA}$. Below T_N the compound is characterized as a triangular frustrated antiferromagnet with a small XY-like anisotropy [2]. Vanadium spins are confined to the hexagonal basal plane ab . In order to resolve the frustration of the spins on the triangular lattice, the spins arrange in a 120° structure. Direct exchange along the c axis favors antiferromagnetic spin chains that are also antiferromagnetically coupled perpendicular to the c axis. In the ordered phase the ratio of the intrachain to the interchain exchange yields $J/J' \simeq 1040$ [3, 4], which turns CsVBr₃ an ideal candidate for investigating quasi 1D magnetism in the paramagnetic phase.

In order to elucidate the quasi 1D behavior of CsVBr₃, we performed an experiment on the cold triple axis spectrometer TASP (Paul Scherrer Institut, Switzerland) using a fixed final wavevector of 1.97 \AA^{-1} and a collimation of open-80'-sample-open-open. The cylindric single crystal (height 22 mm, diameter 8 mm) was mounted into an aluminum sample can. The orange cryostat operated in a temperature range of 1.7 K to room temperature and provided a temperature stability of better than 0.1 K.

We probed the temperature dependence of the excitation energy at the magnetic (003) Bragg reflection between T_N and 100 K by means of constant- Q scans. Data were analyzed using a double Lorentzian in terms of the damped harmonic oscillator model that has already been successfully applied for describing the lineshape of one phonon processes [5]. The fitting parameters ω_q (frequency of the damped harmonic oscillator), Γ_q (linewidth) and an overall scaling parameter were extracted from the data.

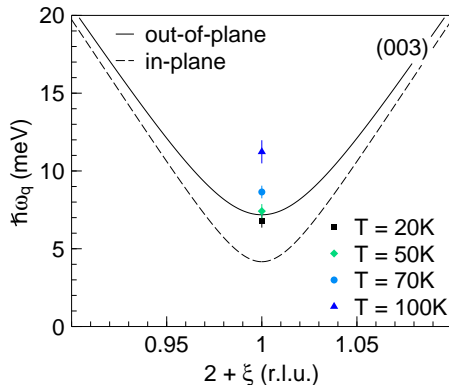


Figure 1: Energy gap of the in-plane branches at the magnetic zone center (003).

The excitation energy at the zone center corresponds to $\omega_q = \sqrt{\Omega_q^2 - \Gamma_q^2}$, where Ω_q denotes the eigenfrequency of the system.

Fig. 1 displays the excitation energy of the degenerate in-plane modes around (003) for particular temperatures. For illustration purposes the optic out-of-plane and the acoustic and optic in-plane branches of the 3d magnon dispersion are included. We observe a shift of the frequency ω_q to higher energies upon raising temperature. This upward renormalization of the dispersion follows a linear increase in the temperature range between 20 K and 100 K. Similarly, the eigenfrequency Ω_q of the undamped oscillator and the linewidth Γ_q linearly increase with temperature (see Fig. 2).

The observed increase in the gap energy cannot be explained by conventional spin wave theory or dipolar exchange. Instead, a recently developed approach using a hexagonal Heisenberg spin system predicts this upward renormalization of the excitation energy [6]. Since the model emphasizes 3D correlations, the observed behavior should be independent of the spin value of the magnetic system. In this sense, upward renormalization was also found in the isomorphic compounds CsMnBr₃ [7] and CsNiCl₃ [8] with spin quantum numbers $5/2$ and 1 , respectively.

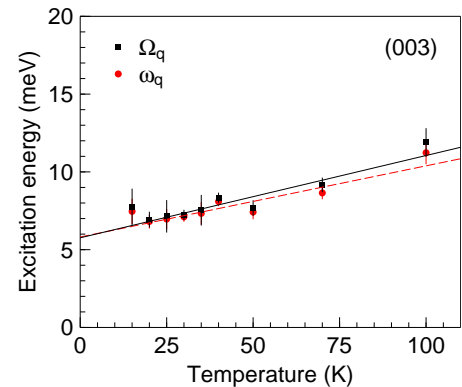


Figure 2: Both the eigenfrequency Ω_q and the frequency of the damped harmonic oscillator model ω_q linearly increase with temperature in the disordered phase.

The work was performed at the spallation source SINQ, Paul Scherrer Institut, Villigen, Switzerland.

References

- [1] M. F. Collins and O. A. Petrenko. *Can. J. Phys.*, 75:605, 1997.
- [2] A. Hauser, U. Falk, P. Fischer, and H. U. Güdel. *J. Solid State Chem.*, 65:343, 1985.
- [3] R. Feile, J. K. Kjems, A. Hauser, H. U. Güdel, U. Falk, and A. Furrer. *Solid State Comm.*, 50:435, 1984.
- [4] S. E. Nagler, D. G. Mandrus, and D. A. Tennant. *Physica B*, 241-243:561, 1998.
- [5] B. Fåk and B. Dorner. *Physica B*, 234-236:561, 1997.
- [6] E. Rastelli and A. Tassi. *Phys. Rev. B*, 70:214407, 2004.
- [7] C. Reich, P. Böni, and B. Roessli. *Phys. Rev. Lett.*, 91:157203, 2003.
- [8] I. A. Zaliznyak, L.-P. Regnault, and D. Petitgrand. *Phys. Rev. B*, 50:15824, 1994.

1.3 Singlet formation in $\text{Ca}_{0.83}\text{CuO}_2$

V. Kargl¹, P. Böni¹, M. M. Koza², H. Mutka²

¹Physics Department E21, Technical University Munich, 85747 Garching, Germany

²Institut Laue-Langevin, 6 rue Jules Horowitz, B.-P. 156, 38750 Grenoble, France

Charge doping remains one of the most fascinating aspects of low dimensional magnetism. In particular, cuprate compounds allow for hole doping into its edge-sharing or corner sharing CuO_2 chains [1]. Upon doping, these chains become diluted and singlet pairing of adjacent spins may occur. From an experimental point of view, copper oxide compounds of such crystal structures thus serve as model system for the $S = 1/2$ 1D Heisenberg spin chain.

For instance, $\text{Ca}_{0.83}\text{CuO}_2$ features within its orthorhombic CuO-sublattice edge sharing CuO_2 chains [2]. The lattice constants of the magnetic subcell are $a = 2.787(3)$ Å, $b = 6.300(1)$ Å and $c = 10.571(1)$ Å. Based on the formal copper valence of the compound (+2.34) 66% of the Cu sites carry a magnetic moment. We expect dimerization of adjacent spins in the diluted CuO_2 spin chains that are antiferromagnetically coupled along the chain direction a [3].

We performed susceptibility and inelastic neutron scattering measurements, in order to reveal the 1D character of the spin chain compound $\text{Ca}_{0.83}\text{CuO}_2$. For the first type of measurements a conventional calorimeter of Quantum Design, Inc., was used. D. C. magnetization was measured in an external field of 1 T. Neutron spectroscopy was performed on the thermal time of flight spectrometer IN4 (Institut Laue-Langevin, $\lambda_i = 2.3$ Å). Besides the sample vanadium and the cylindrical empty aluminum can was investigated in the temperature range of 2 K to 80 K. In order to derive the scattering law $S(Q, \omega)$, we normalized the data to vanadium, corrected for the empty can and self absorption and interpolated the data to constant wavenumbers.

Fig. 1 shows the susceptibility of $\text{Ca}_{0.83}\text{CuO}_2$. The Curie Weiss law fitted in the paramagnetic phase yields 66(1)% magnetic copper spins and an antiferromagnetic Curie Weiss temperature of 37.5(9)°.

We further analyzed the experimental data below 200 K based on the alternating 1D Heisenberg chain that leads to

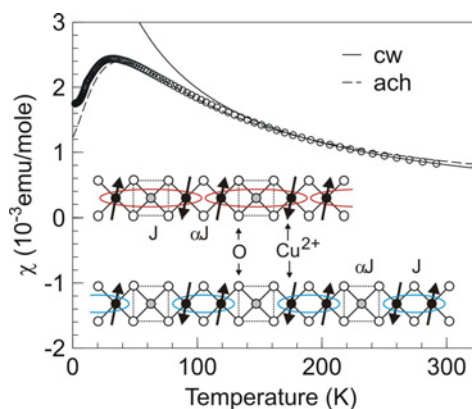


Figure 1: Susceptibility of $\text{Ca}_{0.83}\text{CuO}_2$, obtained by D.C. magnetization measurements in 1 T. The solid and the dashed line indicate the fit with respect to the Curie Weiss law (cw) and the alternating 1D Heisenberg spin chain (ach). The inset illustrates the two possible exchange paths in case of dimerization.

58(1)% magnetic copper spins within the chain and an exchange correlation of 61(1) K [4].

Moreover, the alternating parameter, that is a measure of the isotropic magnetic correlation of one spin to its left and right neighbor, was estimated to be 0.98(1) close to the uniform chain. This result agrees well with literature [5]. Both derived values of Cu^{2+} ions approximately coincides with the value that is expected from the copper valence. In this sense, every third copper moment in the chain is zero. Adjacent antiferromagnetic spins may thus form spin singlets via the exchange path Cu-Cu or Cu-O-Cu (see inset of Fig. 1).

The structure factor obtained by neutron scattering reveals typical intradimer distances [6]. The first maximum in $S(Q)$ corresponds to the distance of the two coupled spins along the chain. In order to account for the incoherent background, a Q independent term was used besides the 1D Heisenberg model. The fit to the 2 K and the 25 K data reveal an intradimer distance of 5.4(1) Å and 5.7(1) Å, respectively. Both results correspond to two times the copper distance along the chain. We thus conclude that singlet formation takes place along the Cu-O-Cu exchange path. The experimentally observed next nearest neighbor coupling of spins coincides to the intradimer distances found in the cuprates $\text{Sr}_{0.73}\text{CuO}_2$ [7] and $\text{Sr}_{14}\text{Cu}_{24}\text{O}_{41}$ [8].

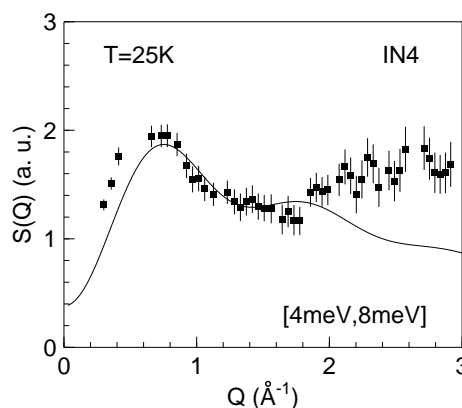


Figure 2: Structure factor of $\text{Ca}_{0.83}\text{CuO}_2$ at 25 K, measured by means of time of flight spectroscopy on IN4 ($\lambda_i = 2.3$ Å). The fit yields an intradimer distance of 5.7(1) that is approximately equivalent to two times the copper distance along the chain.

We acknowledge S. Kazakov, ETH Zürich, Switzerland, who synthesized the $\text{Ca}_{0.83}\text{CuO}_2$ sample.

References

- [1] T. M. Rice. *Z. Physik B*, 103:165, 1994.
- [2] A. Shengelaya et al. *Phys. Rev. Lett.*, 80:3626, 1998.
- [3] G. I. Meijer et al. *Phys. Rev. B*, 58:14452, 1998.
- [4] W. E. Estes et al. *Inorg. Chem.*, 17:1415, 1978.
- [5] G. J. Meijer et al. *Europhys. Lett.*, 42:339, 1998.
- [6] T. Barnes et al. *Phys. Rev. B*, 59:11384, 1999.
- [7] G. I. Meijer et al. *Phys. Rev. B*, 60:9260, 1999.
- [8] R. Eccleston et al. *Phys. Rev. Lett.*, 81:1702, 1998.

1.4 Spin wave damping in the isotropic Heisenberg antiferromagnet RbMnF_3

Sebastian Stüber¹, Marc Janoschek^{1, 2}, David P. Belanger³, Peter Böni¹

¹Physics Department E21, Technical University Munich, 85747 Garching, Germany

²Laboratory for Neutron Scattering, ETHZ & PSI, CH-5232 Villigen PSI, Switzerland

³University of California, Santa Cruz, Physics Department, CA 95064, USA

RbMnF_3 is a simple cubic antiferromagnet, ordering below the Néel temperature $T_N = 83$ K, and its magnetic moments are oriented along the [111] direction [1]. This systems spin dynamics have already been studied in the 1970ies [2], however because of limited energy resolution (0.2 meV), these measurements remain deficient, especially for low temperatures.

The work presented here is the continuation of last years research, extending available data. Neutron Resonance Spin Echo (NRSE, invented by R. Golub and R. Gähler [3] in 1987, for an introduction see e.g. [4]) offers the possibility to significantly improve the data quality, as it increases energy resolution by at least an order of magnitude, compared to the stated limitations of standard triple axis spectrometry. Our main scientific case was to check the compliance between theory and experiment, which for this system has been started by S. Rezende and R. White [5]. The numerical simulations of Rezende and White predict a strong temperature dependence of the magnon line widths, but as a major result of our experiment it is found that the line width does not decrease with decreasing temperature below a saturation value that depends on the magnon momentum.

Exemplarily, the combined data for one measured magnon are shown in Fig. 1. The scaling of the line width with temperature is in agreement with the data of Windsor [2]. The effect that we find two different saturation line widths - sample independent - is not understood yet, and will be the target of future research.

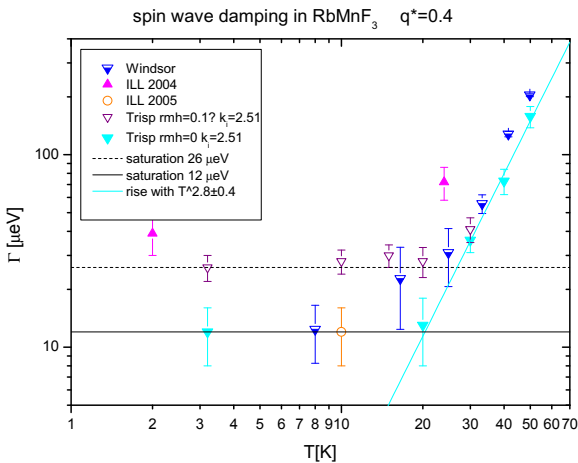


Figure 1: Spin wave damping of the transverse magnon [0.4 0.4 0.6]. Data shown is from Windsor [2], and multiple measurements on two samples of RbMnF_3 . Included are the approximate values of the saturation line width and the scaling $\propto T^{2.8}$ with temperature.

The experiments were performed at the thermal triple-axis spectrometers with spin echo option Trisp at the FRM-II, and ZETA/IN20 at the ILL.

Comparable measurements were done for different magnons, transverse and longitudinal, resulting in the saturation line widths of Fig. 2.

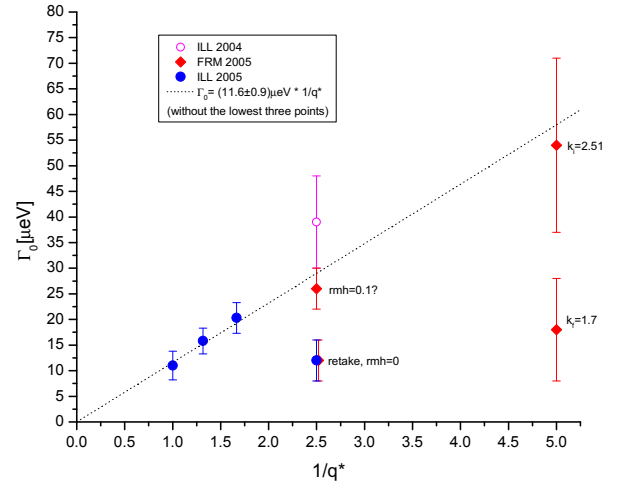


Figure 2: Saturation line widths plotted against $\frac{1}{q^*}$ for the magnons studied, q^* is the spin wave momentum transfer in units of the magnetic zone boundary wave vector. The line widths of the two experiments are compatible. The respective trend is sketched.

The relation found for these saturation values is [6]

$$\Gamma_0 = C \cdot \frac{1}{q^*}, \quad (1)$$

with $C = 11.6 \pm 0.9 \mu\text{eV}$, and q^* the spin wave momentum transfer in units of the magnetic zone boundary wave vector, $q^* = \frac{q}{0.25}$. For this fit we did not consider the lower saturation levels of $q^* = 0.4$ and 0.2 , but the remaining points extrapolate to zero linewidth for infinite q^* , which seems reasonable.

The NRSE technique proved to be a valuable and reliable tool for the study of dynamic magnetic properties.

References

- [1] D. Teaney, M. Freiser, and R. Stevenson. *Phys. Rev. Lett.*, 9:212–4, 1962.
- [2] C. Windsor, D. Saunderson, and E. Schedler. *Phys. Rev. Lett.*, 37(13):855–8, 1976.
- [3] R. Golub and R. Gähler. *Phys. Lett. A*, 123, 1987.
- [4] T. Keller, R. Golub, and R. Gähler. *Scattering*, pages 1264–86. San Diego: Academic Press, 2002.
- [5] S.M. Rezende and R.M. White. *Phys. Rev. B*, 18:2346–9, 1978.
- [6] S. Stüber. Spin wave damping in the isotropic heisenberg antiferromagnet RbMnF_3 . Master's thesis, Physik-Department, Technische Universität München, 2005.

1.5 The 4f multiplet in the Antiferro-Quadrupolar compound TmTe

E. Clementyev¹, A. Podlesnyak²

¹Physics Department E21, Technical University Munich, 85747 Garching, Germany

²Laboratory for Neutron Scattering, ETHZ & PSI, CH-5232 Villigen PSI, Switzerland

The Tm monochalcogenide family displays exotic physical properties including valence instabilities and quadrupolar ordering. In particular TmTe was reported to undergo a phase transition at $T_Q = 1.7$ K above the magnetic ordering temperature ($T_N = 0.4$ K) [1]. This transition was ascribed to the onset of long-range ordering among the Tm quadrupolar moments, but the exact mechanism is still controversial. The most crucial question is the origin of the ground state of the Tm 4f multiplet in TmTe. One problem is the lack of experimental consensus regarding the crystal field level scheme. Tm is divalent in this compound. In a cubic point symmetry the ground state multiplet splits into one quartet and two doublets. A few attempts to measure the crystal field transitions yielded conflicting results with different magnitude of splitting (up to 19 meV), different sequences of levels or even no detectable excitations at all (see [2] and references therein). Obviously, the experimental situation requires some clarification.

Experimental data collected on pure TmTe show relatively broad crystal field transitions below 1 meV [3]. To avoid this broadening due to the quadrupolar correlations the measurements on a diluted compound, namely 10% Tm impurity in the nonmagnetic YbTe have been performed on the time-of-flight spectrometer FOCUS. Yb is in the 2+ state in YbTe, that is why it is equivalent to the nonmagnetic Lu ion in the current situation. The incoming neutron energy was 3.27 meV yielding the energy resolution at the elastic position of about 0.1 meV. Be filter was used to suppress the second order contribution to the scattering.

For the first time a TmTe-based system clearly demonstrated sharp crystal field transitions from the ground state which is very likely the Γ_8 quartet (see Fig. 1). Such a spectrum is unique since the total magnitude of the crystal field splitting is only 0.9 meV, one or even two orders of magnitude smaller than in the majority of the 4f systems. Usually insulating Tm compounds demonstrate the total magnitude of 20 to 100 meV, while some metallic systems show the crystal field splitting of about 10 meV due to the screening of the electrostatic potential by the conduction electrons. The total magnitude of 0.9 meV is indeed a very puzzling feature of TmTe.

Two distinct crystal field transitions have been observed in $\text{Tm}_{0.1}\text{Yb}_{0.9}\text{Te}$ at $E \approx 0.3$ meV and $E \approx 0.9$ meV. Since

the matrix element of the transition between two doublets is zero, the only possibility to see two transitions at low temperature is to place the Γ_8 quartet as a ground state. The arrangement of the excited levels, the doublets Γ_6 and Γ_7 , has to be clarified by a careful fitting of the data. Absorption correction is required for TmTe-based compounds due to a huge neutron capture cross-section of Tm (100 barn). The neutron absorption is very dramatic in the case of low values of the incoming neutron energy (5 meV or less) and the outgoing neutron energy (down to 1 meV).

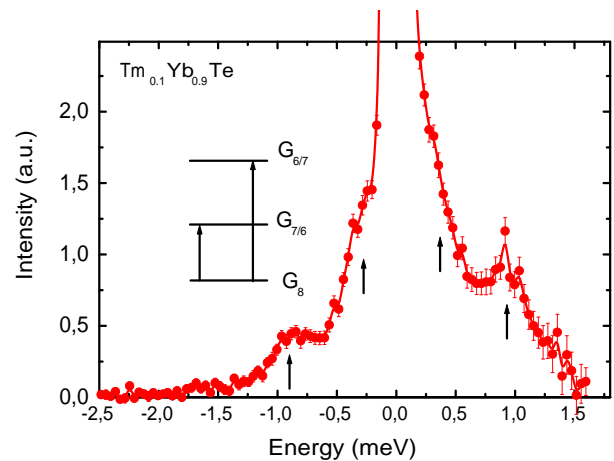


Figure 1: Neutron scattering spectrum of $\text{Tm}_{0.1}\text{Yb}_{0.9}\text{Te}$ measured on FOCUS at $T = 4$ K and $E_f = 3.27$ meV. The crystal field transitions are indicated by arrows. Insert: the splitting scheme for the Tm ions in TmTe.

In conclusion, the result of our inelastic neutron scattering study clearly indicate that the Γ_8 quartet is a ground state of any crystal field splitting scheme or any theory of the quadrupolar ordering in TmTe based on the doublet ground state has to be ruled out. The observed effects are opposite to the prediction of the point charge model. The puzzling small magnitude of the total crystal field splitting in this compound will be a subject of the forthcoming study.

References

- [1] T. Matsumura et al. *Physica B*, 206&207:380, 1995.
- [2] T. Matsumura et al. *Phys. Rev. B*, 66:104410, 2002.
- [3] E. Clementyev et al. *Physica B*, 230-232:735, 1997.

1.6 The special features of the ground state in heavy fermion CeAl_3

N.Tiden², E.Clementyev¹, A.Podlesnyak³

¹Physics Department E21, Technical University Munich, 85747 Garching, Germany

²Russian Research Centre Kurchatov Institute, 123182 Moscow, Russia

³Laboratory for Neutron Scattering, ETHZ & PSI, CH-5232 Villigen PSI, Switzerland

CeAl_3 is a classical dense Kondo compound extensively studied during the last 30 years. The origin of the ground state in this compound is still an open question. Well-defined oscillations of the integrated intensity of the quasielastic magnetic spectral response as a function of the momentum transfer have been observed in CeAl_3 in the recent inelastic neutron scattering (INS) experiments [1]. These oscillations take place at $T > T_K$ (T_K = Kondo temperature).

To study the origin of the modulated spectral response INS experiment on polycrystalline $\text{Ce}_{0.9}\text{Y}_{0.1}\text{Al}_3$, $\text{Ce}_{0.9}\text{La}_{0.1}\text{Al}_3$ and CeAl_3 as a reference compound have been performed on the time-of-flight spectrometer FOCUS (SINQ, PSI) at $T = 4$ K. A CCR has been used instead of the Orange Cryostat in order to reduce the background contribution. The incoming neutron energy and the energy resolution at the elastic line were 3.27 meV and 0.1 meV, respectively. A Beryllium filter has been used to suppress the second order contamination to the scattering. The measurements of an empty cell and vanadium have been performed in order to estimate the background contribution and to perform absolutisation of the INS data. It is known from the previous measurements on LaAl_3 that the phonon contribution is negligible. The range of the scattering angles was $20 - 125^\circ$, that corresponds to the momentum transfer range $0.5 - 2.2 \text{ \AA}^{-1}$. The transmission for all the samples has been estimated as about 93% and no absorption correction has been performed. The detectors located at Bragg's angles have been masked. All other detectors have been grouped into 25 subgroups and normalized by their efficiency.

The magnetic spectral response has been estimated by the subtraction of the background contribution (empty cell) from the INS spectra (see inset on Fig. 1.). Fig. 1 shows typical magnetic spectra of $\text{Ce}_{0.9}\text{Y}_{0.1}\text{Al}_3$ measured at $T = 4$ K for $\langle Q \rangle = 0.521, 0.9$ and 1.66 \AA^{-1} . The magnetic excitation spectra were fitted by a Lorentzian spectral function multiplied by the temperature factor. The full width at half maximum (FWHM) for CeAl_3 was estimated as $\Gamma = 1.36$ meV, in a good agreement with the previous data [2]. The intensity of the quasielastic magnetic scattering was estimated by integration over the energy transfer range $-5 - 5$ meV for every one of the 25 subgroups. The dependencies of the integrated intensities on the momentum transfer at $T = 4$ K are shown in Fig. 2. It is clear that there is no difference in the Q -dependence between the samples with Y and La dilution. At the same time CeAl_3 has a steeper gradient but the period of oscillations is the same for all compounds.

To sum up, similar to pure CeAl_3 , a modulation of the integrated intensity has been observed in the diluted compounds $\text{Ce}_{0.9}\text{Y}_{0.1}\text{Al}_3$ and $\text{Ce}_{0.9}\text{La}_{0.1}\text{Al}_3$. This modulation is indicative of strong magnetic correlations in the paramagnetic CeAl_3 -based compounds above the characteristic Kondo temperature.

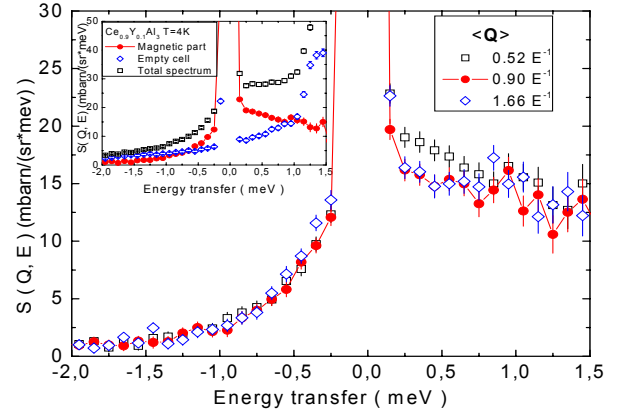


Figure 1: Magnetic spectral response of $\text{Ce}_{0.9}\text{Y}_{0.1}\text{Al}_3$ at $T = 4$ K and $\langle Q \rangle = 0.52, 0.9$ and 1.66 \AA^{-1} . Inset typical INS spectra: squares and rombs - background contributions, circles - the magnetic component.

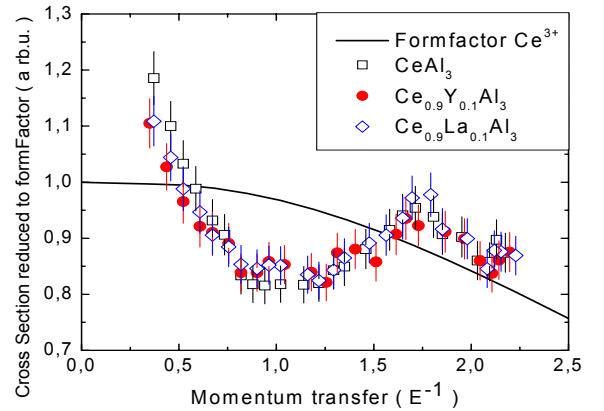


Figure 2: Momentum transfer dependence of the intensity of the quasielastic scattering in CeAl_3 , $\text{Ce}_{0.9}\text{Y}_{0.1}\text{Al}_3$ and $\text{Ce}_{0.9}\text{La}_{0.1}\text{Al}_3$ at 4 K. Solid line - cerium squared magnetic formfactor.

References

- [1] V.N. Lazukov et al. *JETP Letters*, 76:353, 2002.
- [2] A.P. Murani et al. *Solid State Commun.*, 80:523, 2002.

1.7 Inelastic neutron scattering study of polycrystalline chromium

E. Clementyev¹, P. Böni¹, I. L. Sashin²

¹Physics Department E21, Technical University Munich, 85747 Garching, Germany

²Frank Laboratory of Neutron Scattering, Joint Institute for Nuclear Research, 141980 Dubna, Russia

Cr is one of the most thoroughly studied itinerant antiferromagnets (see [1] and references therein). In particular, many studies have been carried out on Cr by the inelastic neutron scattering (INS) technique. Recent interest has been focused on the unusual spectral features of chromium, namely the low-energy Fincher-Burke (FB) excitations around the commensurate positions observed in the energy transfer range 4 meV to 8 meV [2]. The origin of these modes is unclear as well as their relevance with respect to incommensurate order. A series of high-resolution INS measurements was performed recently to characterize the behavior of the FB-excitations [3, 4]. However, these single crystal experiments on triple-axis spectrometers were extremely time-consuming and provided spectra only for a limited volume in the Q -space and a limited temperature range. This is not surprising since the FB mode shows up as a relatively weak peak and collecting the INS data could easily take many weeks (or even months) on a conventional triple-axis spectrometer.

Time-of-flight (TOF) spectrometers (especially the ones without detectors with a fine spatial resolution) are not very competitive in mapping out the Q -dependence of the magnetic excitations. However these instruments are very powerful excitation scanners in terms of the density of states. A huge detector with a sizable solid angle as well as a huge sample mass are two factors in favor of the TOF measurements. The main goal of the current measurement was a feasibility study of a TOF experiment using 250 g of polycrystalline chromium. The second goal was to investigate the effect of strain in the sample on the FB excitations. In the preceding experiment these excitations have been observed only on the samples without strains.

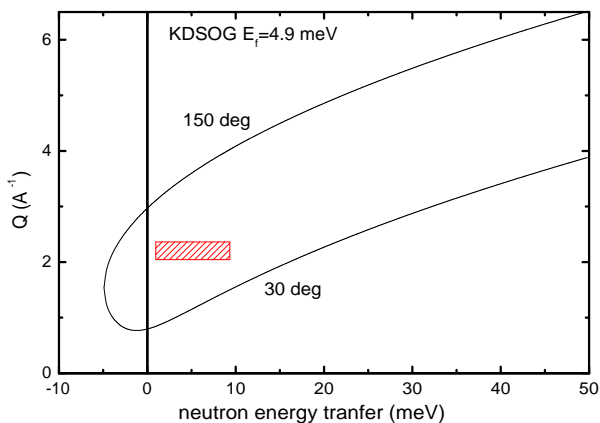


Figure 1: The region in the Q -Energy space accessible on KDSOG for the scattering angles between 30° and 150° for the fixed final energy 4.89 meV. Dashed area shows the $Q - E$ range to scan the FB excitations.

The sample (Cr pieces, 99.995% pure according to Alfa-Aesar) has not been annealed so we assume severe internal strains in it. The INS spectra were measured at $T = 230$ K on the TOF spectrometer of inverted geometry KDSOG (JINR, Dubna). The final neutron energy $E_f = 4.89$ meV was provided by PG analyzers yielding an energy resolution of 0.5 meV at the elastic position and $\approx 7\%$ at high energy transfer. A Be filter was used to reduce the higher order contamination. Since the FB mode is only visible in a relatively small Q -range (see Fig. 1) we take into account only detectors located at certain scattering angles starting from 50° . The INS spectra of the Cr sample and Al empty sample holder collected in about 24 hours are shown on Fig. 2. In addition to the peaks of the phonon density of states in Cr two low-energy peaks have been observed at ≈ 2.7 meV and ≈ 6.2 meV. It is well-known that the phonon contribution to the INS spectra in Cr does not show any peaks below 15 meV.

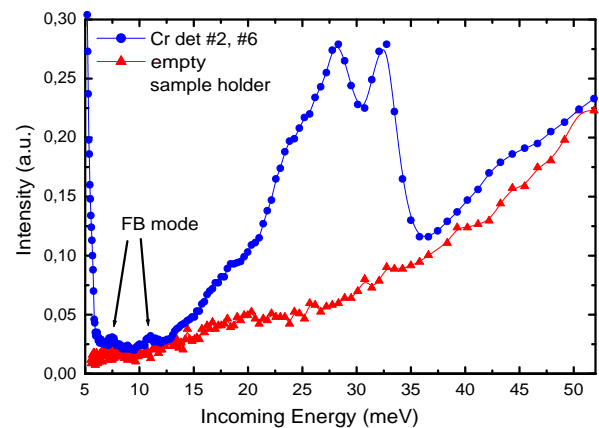


Figure 2: Inelastic neutron scattering spectra of Cr and empty sample holder measured at $T = 230$ K and $E_f = 4.89$ meV. The positions of the FB excitations are indicated by arrows. Please note that the energy transfer $E = E_f - 4.89$ meV.

To sum up, the FB excitations have been observed for the first time on a polycrystalline Cr sample. The TOF spectrometer KDSOG is well suited to study in detail the temperature dependence of the low-energy magnetic density of states in Cr. Such measurements are in progress now.

References

- [1] E. Fawcett. *Rev. Modern Physics*, 60:209, 1988.
- [2] S.K. Burke et al. *Phys. Rev. Lett.*, 51:494, 1983.
- [3] P. Böni et al. *Applied Physics A*, A 74 suppl.:716, 1988.
- [4] H. Hiraka. *Phys. Rev. B* 70, 70:144413, 2004.

1.8 Magnetic-field induced instability in the A-Phase of MnSi: Bulk and SANS measurements

Daniel Lamago^{1, 2}, Robert Georgii^{1, 2}, Christian Pfleiderer¹, Peter Böni¹

¹Physics Department E21, Technical University Munich, 85747 Garching, Germany

²ZWE FRM-II, Technical University Munich, 85747 Garching, Germany

MnSi develops itinerant-electron magnetism below $T_c = 29$ K that supports a long wavelength helical modulation. In recent years the properties of MnSi have attracted great scientific interest [1, 2]. Motivated by recent efforts [3] we revisited the reorientational processes of the helical modulation in MnSi at ambient pressure as function of field. We combine small-angle neutron scattering with AC susceptibility data. This provides unexpected new insights into the nature of the helical modulation and its possible connection to the NFL phase and the partial magnetic order at high pressure [2].

The AC susceptibility of a single crystal of MnSi has been measured by means of a 9 T Quantum Design PPMS System. SANS-experiments were carried out at the diffractometer MIRA at FRM-II in Garching.

Fig. 1(a) shows typical AC-susceptibility data as measured in the A-phase used for determining the phase boundaries of the A-phase. As function of the magnetic field, the AC susceptibility displays an abrupt change of slope and a minimum that signifies the A-phase. The onset of this minimum has been mapped out as function of temperature and is shown in the phase diagrams in Figs. 1(b), (c) and (d).

Typical small-angle neutron scattering data are shown in Fig. 2. At a temperature $T = 28.5$ K, just below T_c , we observe well defined spots due to the helical magnetic order (lower panel) as reported in numerous studies before. With increasing magnetic field, we observe as an additional feature a ring of scattered intensity with a radius corresponding to $|\mathbf{Q}|$, that was not present at $B = 0$.

The appearance of this ring of intensity is only gradual from the $B = 0$ -phase into the A-phase. Interestingly, we observe the same qualitative behaviour also for $B \parallel \langle 110 \rangle$ and $B \parallel \langle 111 \rangle$.

Therefore, the behaviour is isotropic and not related to a particular initial direction of the helical order that is enforced at low T by anisotropies enforced by the lattice.

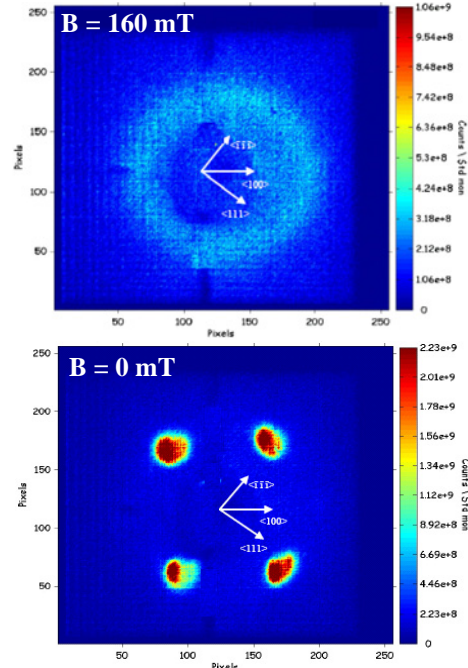


Figure 2: Neutron SANS intensity of MnSi at $T = 28.5$ K (just below T_c) recorded at the diffractometer MIRA at FRM-II. Lower panel: data at $B = 0$. Four resolution-limited spots are characteristic of long-range helical order, consistent with previous work. Upper panel: data at 0.16 T, where a ring of scattering intensity is visible.

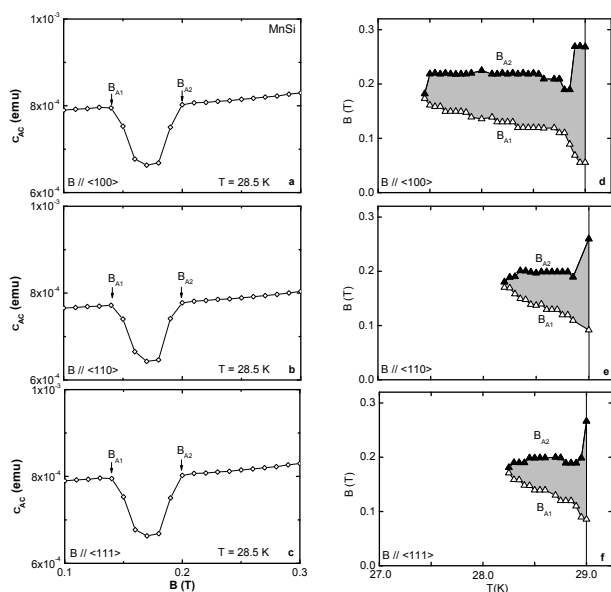


Figure 1: (a), (b) and (c) AC susceptibility as measured in MnSi using a magnetic field with $B \parallel \langle 100 \rangle$, $B \parallel \langle 110 \rangle$ and $B \parallel \langle 111 \rangle$ respectively. Panels (d), (e) and (f) show the phase boundary of the A-phase for $B \parallel \langle 100 \rangle$, $\langle 110 \rangle$, and $\langle 111 \rangle$, respectively.

The distinct change of slope of the AC susceptibility as well as the sharp peaks in the specific heat (not shown) indicate a well defined phase transition into the A-phase that shows up in the SANS-experiments as a ring of scattering intensity.

Our experiments show that combining SANS measurements at the new diffractometer MIRA at FRM-II with bulk measurements helps resolving the microscopic nature of the reorientation transition in MnSi. The results indicate the appearance of a new form of magnetic ordering that may be interpreted in terms of skyrmions. Presently, a device for 3-dimensional polarisation analysis, MuPAD, is being installed at MIRA and will help to resolve the microscopic magnetic structure in the A-phase of MnSi and distinguish between the various models.

References

- [1] B. Roessli, P. Böni, W.E. Fischer, and Y. Endoh. *Phys. Rev. Lett.*, 88:237204, 2002.
- [2] C. Pfleiderer, D. Reznik, L.Pintschovius, H.v. Löhneysen, M. Garst, and A. Rosch. *Nature*, 427:227, 2004.
- [3] A.I. Okorokov, S.V. Grigoriev, Yu.O. Chetverikov, S.V. Maleyev, R. Georgii, P. Böni, D. Lamago, H. Eckerlebe, and K. Pranzas. *Physica B*, 356:259, 2005.

1.9 Low-energy magnetic excitations in Mn-doped single-crystal Cr

P. G. Niklowitz¹, P. Böni¹, C. Niedermayer²

¹Physics Department E21, Technical University Munich, 85747 Garching, Germany

²Laboratory for Neutron Scattering ETH & PSI, 5232 Villigen PSI, Switzerland

The low-energy excitations of the archetypal transverse spin-density wave (TSDW) phase of elemental Cr consist mainly of steeply dispersive excitations around the incommensurate ordering wave vector and excitations (Fincher-Burke (FB) modes) at (100) [1, 2, 3, 4]. V doping leads to a suppression of magnetism, while Mn doping leads at higher temperatures to the appearance of a phase with a commensurate spin-density wave (CSDW) [1]. To better understand the physical origin of the low-energy excitations in Cr we want to follow their evolution when passing through different magnetic phases. Therefore, we have measured magnetic scattering of a $\text{Cr}_{0.993}\text{Mn}_{0.007}$ single crystal in the plane defined by the [100] and [010] crystallographic axis of its bcc crystal structure using the triple-axis spectrometer RITA2 at PSI. The experimental configuration was guide-40'-sample-60'-open-PSD, with vertically focussing monochromator, flat analyser ($E_f = 5.57$ meV), and position sensitive detection (PSD).

A characterization of the crystal by neutron diffraction confirmed commensurate magnetic order at (1,0,0) above 180 K, and incommensurate order at $(1 - \Delta q, 0, 0)$ and symmetrically equivalent positions below 180 K (Δq close to 0.035). In particular, at 100 K and 140 K the spin-density wave is transversely polarized (TSDW phase), while at 40 K longitudinal polarization (LSDW phase) is observed (in agreement with the results of Ref. [5]).

In this study we have focused on the TSDW phase of $\text{Cr}_{0.993}\text{Mn}_{0.007}$ by doing inelastic neutron scattering at 100 K, since the FB mode has been observed in the corresponding phase of elemental Cr. Q -scans have been performed for an energy loss of 2 meV (see Fig. 1), 4 meV, and 7 meV, and E -scans at (100) (see Fig. 2).

The q -scan of Fig. 1 and the scans with $\Delta E = 4$ meV and $\Delta E = 7$ meV are qualitatively similar. Peaks at the satellite positions are due to steeply dispersive low-energy excitations of the incommensurate order like in elemental Cr.

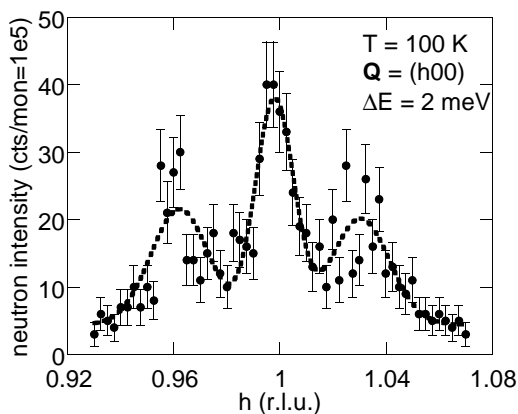


Figure 1: Representative inelastic q -scan in the TSDW phase. The peaks at the positions of incommensurate ordering wave vectors are fitted with Gaussians with identical widths. The counting time per data point was 230 s.

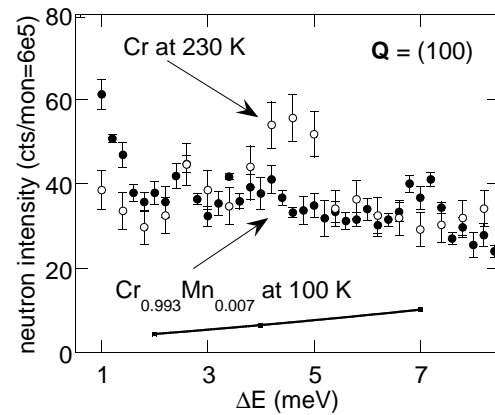


Figure 2: Inelastic scattering at (100) in the TSDW phase. The FB-mode at 4 meV in elemental Cr (empty circles [4], data scaled down) is suppressed in $\text{Cr}_{0.993}\text{Mn}_{0.007}$ (filled circles). The peak at 7 meV is a spurion. The background for the $\text{Cr}_{0.993}\text{Mn}_{0.007}$ data (squares) has been estimated from the tails of the q -scans around (100).

This study shows that the excitations around the satellite positions are robust against Mn doping. In particular, no significant broadening of the inelastic peaks at the satellite positions is observed up to 7 meV, indicating that the average dispersion shows a slope similar to elemental Cr. A central peak appears in elastic measurements of $\text{Cr}_{0.993}\text{Mn}_{0.007}$ and can be traced back to scattering from satellites captured by the vertical resolution. In this study this effect has been observed directly for elastic and inelastic scattering by the PSD. Partially, the inelastic scattering at (100) is caused by low-energy excitations of residual commensurate order.

Figure 2 shows that the FB mode is very sensitive to Mn doping and clearly suppressed, as can be seen from a comparison of E -scans at (1,0,0) of $\text{Cr}_{0.993}\text{Mn}_{0.007}$ with equivalent data from elemental Cr.[4] The FB mode has not been detected in the CSDW phase either.

This work is based on experiments performed at the Swiss spallation neutron source SINQ, Paul Scherrer Institute, Villigen, Switzerland. This research project has been supported by the European Commission under the 6th Framework Programme through the Key Action: Strengthening the European Research Area, Research Infrastructures. Contract no.: RII3-CT-2004-505925.

References

- [1] E. Fawcett. *Rev.Mod.Phys.*, 60:209, 1988.
- [2] Jr. C. R. Fincher, G. Shirane, and S. A. Werner. *Phys. Rev. Lett.*, 43:1441, 1979.
- [3] S. K. Burke, W. G. Stirling, K. R. A. Ziebeck, and J. G. Booth. *Phys. Rev. Lett.*, 51:494, 1983.
- [4] P. Böni, E. Clementyev, Ch. Stadler, B. Roessli, G. Shirane, and S. A. Werner. *Appl. Phys. A*, 74:S716, 2002.
- [5] B. J. Sternlieb, E. Lorenzo, G. Shirane, S. A. Werner, and E. Fawcett. *Phys. Rev. B*, 50:16438, 1994.

1.10 The flux line lattice in Niobium - measurements with polarised and unpolarised neutrons

Sebastian Mühlbauer¹, Robert Georgii², Peter Böni¹, Christian Pfeleiderer¹

¹Physics Department E21, Technical University Munich, 85747 Garching, Germany

²ZWE FRM-II, Technical University Munich, 85747 Garching, Germany

Objectives

Recent polarized SANS measurements [1, 2] of the flux line lattice (FLL) of superconducting niobium showed clear polarization dependent scattering that cannot be explained by means of the ideal model of the FLL. In isotropic superconductors no spin dependent scattering occurs, because the flux lines are orientated parallel to the applied magnetic field B as well as the polarization P of the neutrons [3], because the polarization follows the applied external field adiabatically. Spin flip scattering only occurs either i) assuming a non zero nuclear scattering length distribution with the same periodicity as the FLL (interference term) or ii) assuming a bending of the FLL, ruling out the geometrical constraint of $B \parallel P$.

Measurements

To examine whether the observed polarization dependence is an intrinsic property of pure niobium or is caused by sample impurities, polarized SANS experiments on a single crystal niobium sample were performed at the SANS-2 at the GKSS. A cylindrically shaped single crystal niobium sample was placed inside a cryostat perpendicular to the incident neutron beam. A magnetic field of 0 – 2000 G was then applied parallel to the incident neutron beam. Both the magnetic field and the sample could be rotated independently inside the scattering plane, in order to adjust the scattering geometry. The polarization direction was also chosen to be parallel to the incident neutron beam, and could be reversed using a spin flipper. Several scans through the phase diagram were performed: Constant- T scans, varying the magnetic field from 0 – 2000 G and constant- B scans, varying the temperature from 4 – 9 K. Each scan was performed for both polarization directions as well as zero field and non-zero field cooled.

Additionally bulk measurements (specific heat and susceptibility) of a second niobium sample from the same ingot were performed with a physical properties measurement system (PPMS), to obtain the pinning properties and the phase diagram of the measured sample.

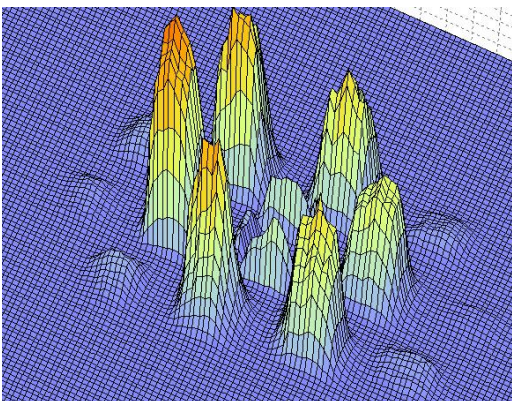


Figure 1: SANS image, measured with a two dimensional PSD of SANS-2. The sixfold symmetry of the Nb FLL is observed. The direct beam is absorbed by a beam dump.

Results and outlook

Analysing the data, the results of [1, 2] could be reproduced: A clear polarization dependent signal was observed, which was clearly connected to the Shubnikov phase of the sample. Above T_c , the differential signal was zero, contrary to the Meissner phase, where polarized SANS measurements are impossible due to the Meissner screening of the sample.

The measurements of the susceptibility showed strong pinning effects, connected to the given purity of 4 N of the sample [4]. As the behaviour of the FLL in Nb is strongly dominated by pinning effects and therefore individual sample properties, it is impossible to nominate the origin of the polarized signal. To reduce pinning effects, ultra pure samples, surface treated by oxygen glowing [5] will be measured on MIRA. A measure for the purity (and therefore for the bulk pinning potential) is the residual resistivity ratio (RRR) of a sample. Measurements with samples of a different RRR will show if either a local bending of the FLL is the origin of the polarized signal or a difference in the local scattering length, related to the pinning centres, originates the polarization dependent scattering.

Recently, measurements by [6, 7] give hints that several symmetry transitions of the FLL, i.e. a melting transition, take place near H_c . Polarized scattering of ultra pure samples will help to clarify the situation, using the very low pinning properties of these samples to examine the undisturbed behaviour of the FLL.

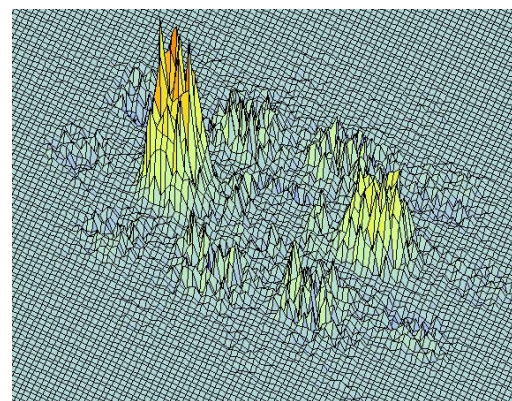


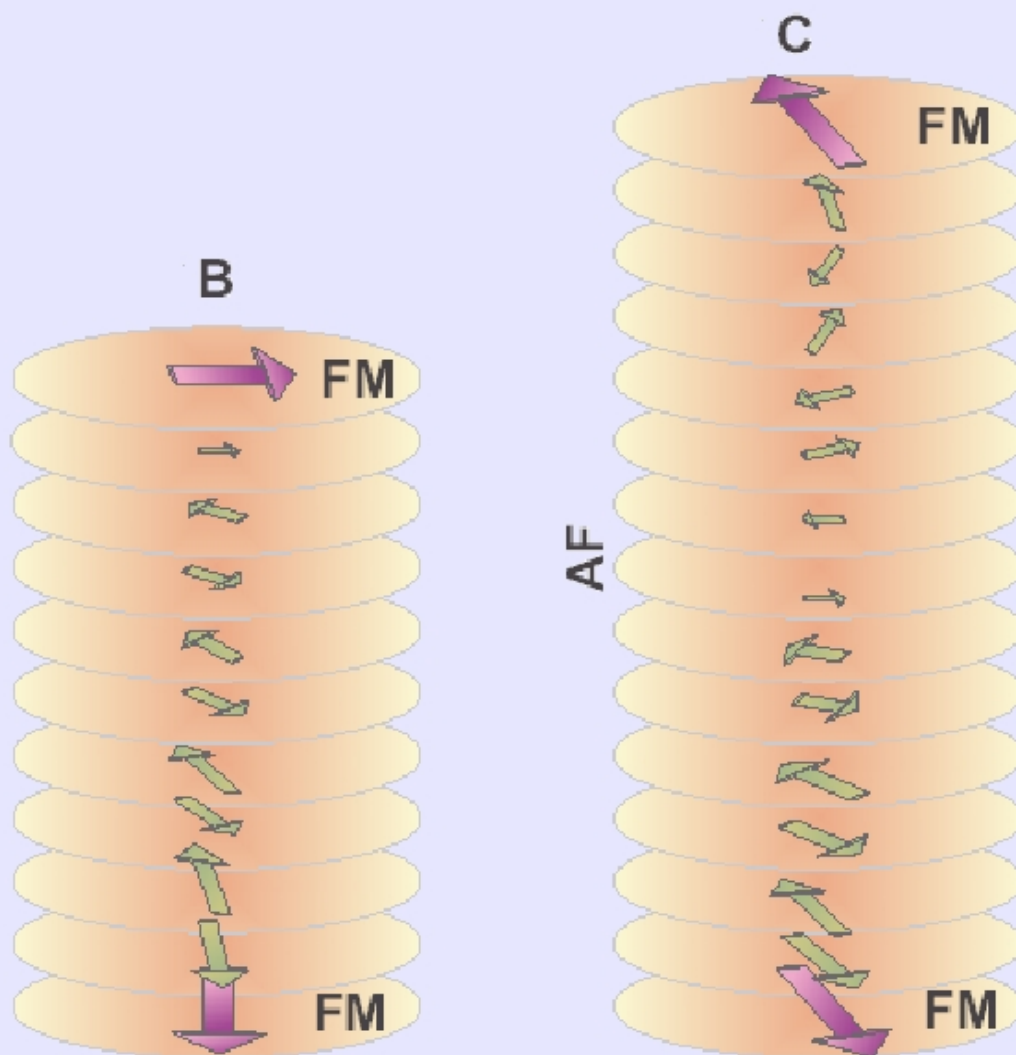
Figure 2: Polarized scattering signal, received by subtracting the two initial polarization states of the incoming neutron beam.

References

- [1] K. Neumann et al. *Eur. Phys. J. B*, **1:5–9**, 1998.
- [2] E. M. Forgan et al. Experimental Report ILL 5-51-229. 2002.
- [3] E. M. Forgan et al. *Physica B*, 115:267–268, 1999.
- [4] S. Mühlbauer. Master's thesis, Technical University Munich, 2005.
- [5] K-H. Berthel. PhD thesis, Dresden, 1976.
- [6] M. Laver et al. Spontaneous symmetry breaking vortex lattice transitions in superconduction niobium. *International Conference on Neutron Scattering ICNS, Sydney, Australia*, 2005.
- [7] M. Laver et al. Experimental report ill 5-42-121. 2004.

2

Multilayers and Interfaces



2.1 Soft X-ray investigations of exchange coupled FM/AM bilayers

V. R. Shah¹, C. Schanzer^{2,1}, S. Legl¹, J. Mayer¹, A. Gaupp³,
F. Schäfers³, S. Valencia³, P. Böni¹

¹Physics Department E21, Technical University Munich, 85747 Garching, Germany

²Laboratory for Neutron Scattering, ETHZ & PSI, CH-5232 Villigen PSI, Switzerland

³BESSY GmbH, Albert-Einstein Straße 15, D-12489 Berlin, Germany

In this report, we present X-ray Magnetic Circular Dichroism (XMCD) as well as element specific hysteresis properties of Fe, Co and Ni as a function of the thickness of antiferromagnet (AF) in an AF/FM bilayer series. Here, the ferromagnet (FM) is 20 nm of Fe₅₀Co₄₈V₂ alloy and the AF is 5 – 60 nm of NiO. We measured dichroism by performing energy scans around the absorption edges of the constituent elements at the positive and negative saturation states of the FM, for a fixed helicity of the incoming elliptically polarized light.

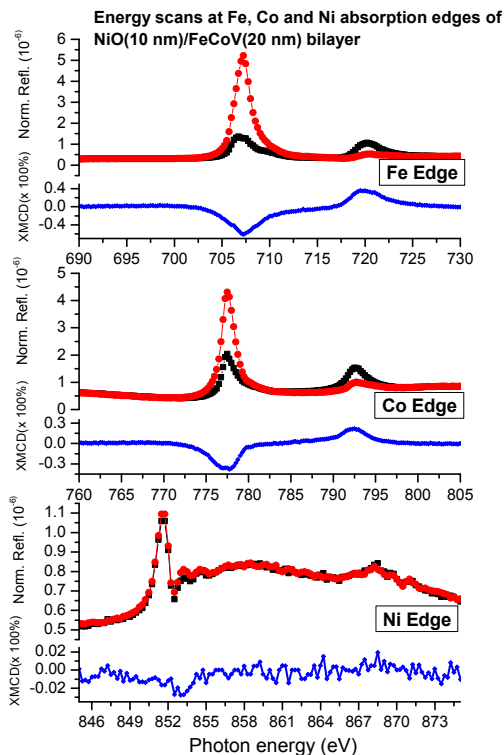


Figure 1: Energy scans of Fe, Co and Ni absorption edges of the NiO(10 nm)/FeCoV(20 nm) bilayer. Below each spectrum, the XMCD signal is shown, which is the difference divided by the sum of intensities at the saturation magnetization states of the FM at ± 300 Oe.

The experiments were performed at the undulator beamline UE56-1-PGM 1b of BESSY using the ultra high vacuum polarimeter chamber [1]. The angle of incidence was set to 70° with respect to the surface normal and specularly reflected intensity was collected. Typical energy scans around the Fe, Co and Ni absorption edges for the sample NiO(10 nm)/FeCoV(20 nm) are shown in Fig. 1, illustrating the L_{III} and L_{II} absorption edges of the respective elements. Element specific hysteresis loops are then recorded with the energy of the X-rays tuned to the respective dichroic maximum. Fig. 2 depicts a representative hysteresis behaviour obtained using the reflected intensities at Fe, Co and Ni absorption edges. In all the bilayers, both Fe and Co exhibits

ferromagnetic hysteresis loops with nearly identical shapes, indicating a uniformly alloyed Fe and Co in the magnetization process. However, a very weak ferromagnetic behaviour at the Ni absorption edge indicates the presence of traces of free Ni from the antiferromagnet NiO, as expected at the NiO surface mostly due to the oxidation-reduction process happening at the metal/oxide interface [2]. However, traces of Ni was detectable only in this bilayer.

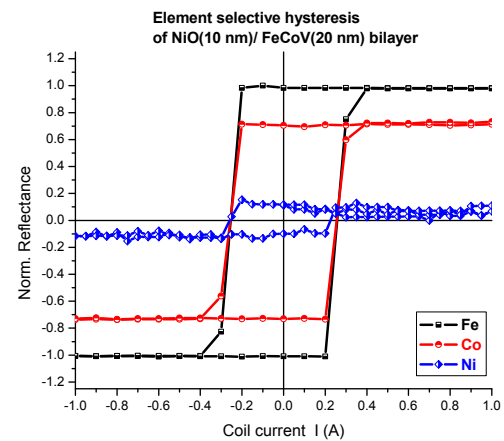


Figure 2: Element selective magnetic hysteresis of Fe, Co and Ni edges in NiO(10 nm)/FeCoV(20 nm) bilayer. The individual plots are scaled according to their relative intensities of the reflected signal.

A dramatic reduction of dichroism is observed when the thickness of NiO is increased. It is evident from bulk magnetization measurements at room temperature that bilayers with top FM layer have strong uni-axial anisotropy when the thickness of the NiO layer is very small where the easy magnetization direction (EMD) coincides with one edge of the substrate. With increasing NiO thickness, the EMD moves away from this edge presumably due to the strong exchange coupling with the NiO anisotropy axis. XMCD results corroborates this picture qualitatively [3], since it is sensitive to the relative orientation of the magnetization and the propagation vector. Detailed analysis of the XMCD and element selective hysteresis loops is in progress.

The authors thank BMBF support (05 ES3XBA/5) for the experiments at BESSY.

References

- [1] F. Schäfers, H. C. Mertins, A. Gaupp, W. Gudat, I. Packe M. Meritin, F. Schmolla, S. D. Fonzo, G. Soullie, W. Jark, R. Walker, X. Le Cann, R. Nyholm, and M. Eriksson. *Appl. Opt.*, 38:4074, 1999.
- [2] T. J. Regan, H. Ohldag, C. Stamm, F. Nolting, J. Lüning, J. Stöhr, and R. L. White. *Phys. Rev. B*, 64:214422, 2001.
- [3] D. R. Lee, Y. Choi, C-Y. You, J. C. Lang, D. Haskel, G. Srajer, V. Metlushko, B. Ilic, and S. D. Bader. *Appl. Phys. Lett.*, 81:4997, 2002.

2.2 Polarized neutron reflectometry on Fe/Cr multilayers at MIRA

V. R. Shah¹, C. Schanzer^{2, 1}, S. Mühlbauer¹, R. Georgii^{1, 3}, P. Böni¹

¹ Physics Department E21, Technical University Munich, 85747 Garching, Germany

² Laboratory for Neutron Scattering, ETHZ & PSI, CH-5232 Villigen PSI, Switzerland

³ ZWE FRM-II, Technical University Munich, 85747 Garching, Germany

Fe/Cr multilayers have been a fascinating system for many fundamental investigations such as the interlayer exchange coupling exhibited by Cr and the Giant magnetoresistance exhibited by these multilayers [1]. Bilinear and biquadratic exchange coupling have been investigated in detail by various experimental techniques and polarized neutron reflectometry has been very handy due to its high sensitivity in the elucidation of the vectorial magnetization depth profile in multilayers.

The instrument MIRA at the FRM-II has been designed for versatile operations such as reflectometry, small angle scattering and multi-MIEZE techniques employing cold neutrons [2]. MIRA has already been functional for specular reflectivity measurements with un-polarized neutrons. Recently there have been efforts to upgrade it step by step to a polarized neutron reflectometer with full polarization analysis, by including polarizer and analyzer components [3]. During the experiment described in this report, a polarizing bender placed at the analyzer stage was employed to select the reflected neutrons from the sample surface, with one spin state (+ state). This effort has been found to be partially successful as reported below. Reversal of the magnetic state of the analyzer was not possible and therefore, the measurement of one scattering cross-section only is reported here.

We investigated [Fe(4 nm)/Cr(3 nm)]₁₀ multilayer grown on glass substrate by magnetron sputtering. The layer thickness profile, the interface roughness etc. were determined by modeling the specular X-ray reflectivity. Individual layer thicknesses of Fe and Cr are determined to be close to 4 and 3 nm, respectively. The magnetization measurement at room temperature and 2 K reveals a very weak antiferromagnetic coupling between the Fe layers.

Fig. 1 depicts the experimental neutron reflectivity data for the Fe/Cr multilayer at magnetic saturation i.e., at 3000 Oe. Specularly reflected neutrons were analyzed by a polarizing bender, kept at + state. The data clearly shows the Kiessing fringes that arise from the total thickness of the multilayer and the first order Bragg reflection that arises from the multilayer periodicity. A simple analysis as shown in Fig. 1 renders a total thickness of 71.6 nm and a multilayer periodicity of 6.9 nm that are rather close to the nominal values and those obtained from x-ray reflectivity analysis.

Using these preliminary values, neutron reflectivity curves are simulated [4] for both spin states of the polarizer and analyzer and the ++ scattering cross-section is compared with the experimental data. A good agreement between the simulation and the experimental data indicates that the polarization analysis works qualitatively. The simulation complements the layer profile obtained from the X-ray reflectivity analysis. In addition the saturation magnetization of the layers is obtained as 2.1 Bohr magneton. It is intended to study biquadratically coupled Fe/Cr layers and the films are being prepared on single crystal substrates to obtain the epitaxy with well defined interfaces and less thickness fluctuations. It is anticipated that full polarization analysis at MIRA is possible in the very near future.

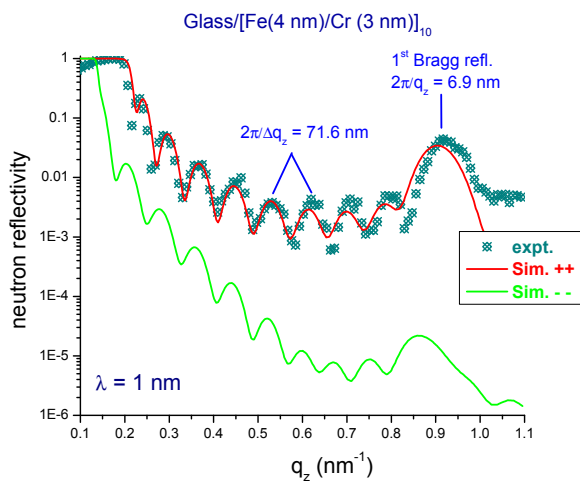


Figure 1: Neutron reflectivity of Fe/Cr multilayers with experimental data compared to the simulation.

References

- [1] S. S. P. Parkin, N. More, and K. P. Roche. *Phys. Rev. Lett.*, 64:2304–2307, 1990.
- [2] MIRA. <http://www.frm2.tum.de/mira/index.shtml>.
- [3] R. Georgii, S. Mühlbauer, and P. Böni. *Private communication*.
- [4] F. Ott. Simulreflec: Reflectivity curve simulations and fitting. <http://www.llb.cea.fr/prism/programs/simulreflec/simulreflec.html>.

2.3 Correlation of magnetic domains in FM/AF/FM trilayers probed by off-specular PNR

C. Schanzer¹, V.R. Shah¹, Andrew Wildes², P. Böni¹

¹Physics Department E21, Technical University Munich, 85747 Garching, Germany

²Institut Laue-Langevin, 6 r. Jules Horowitz, BP 156, 38042 Grenoble Cedex 9, France

We employed off-specular polarized neutron reflectometry with polarization analysis to probe the magnetic configurations of ferromagnetic (FeCoV)/antiferromagnetic (NiO)/ferromagnetic (FeCoV) trilayers during the reversal of magnetization. Experiments were conducted at the reflectometer D17 using a ³He spin filter as analyzer in combination with a 2D-position sensitive detector. Significant diffuse scattering in the spin flip channel indicates the presence of magnetic roughness originating from lateral domains. The obtained results confirm the feasibility of using off-specular polarized neutron reflectivity to unravel the lateral distribution of magnetic domains in such trilayers.

We study the properties of FeCoV/NiO (t_{NiO})/FeCoV trilayers in order to examine a possible coupling between the ferromagnetic (FM) layers mediated by the antiferromagnetic (AF) spacer [1]. DC magnetization measurements show a strong dependence of the magnetization reversal on the NiO layer thickness t_{NiO} [2]. For $t_{\text{NiO}} < 20$ nm the reversal occurs via a single transition whereas for $t_{\text{NiO}} \geq 40$ nm the reversal occurs in two steps, separated by a plateau of nearly zero net magnetization. Within this plateau, the magnetization vectors of adjacent FeCoV layers are aligned antiparallel as it is deduced from specular polarized neutron reflectivity (PNR) measurements [3]. The NiO spacer with $t_{\text{NiO}} \geq 20$ nm represents an intermediate scenario between a combined and distinct magnetization reversal of both FM layers. Specular PNR on this sample shows a reduced magnetic moment of the FeCoV layers during the magnetization reversal indicating the presence of a multi-domain state. Off-specular PNR enables to probe the domain distribution depth resolved, thus providing an insight of the coupling between FeCoV layers across the NiO spacer.

Off-specular PNR with polarization analysis was measured at the reflectometer D17 at ILL with a polarized monochromatic beam (5.5 Å) from a polarizing Fe/Si multilayer monochromator. Neutron spin flippers in the incident and reflected beam enable to invert the polarization of the neutron beam. Taking advantage of the ³He neutron spin filter and a 2D-position sensitive detector the polarization of the specular and diffuse scattered neutrons is analyzed and detected simultaneously for each incident angle of the neutron beam. The data are corrected for the individual efficiencies of the detector pixels and the finite efficiencies of the polarizing monochromator, spin flippers and the ³He neutron spin filter [4].

We measured off-specular reflectivities for all four combinations (+, +, -, -) of the spin states of the incident and the reflected beam with its polarization being parallel (+) or antiparallel (-) to the applied magnetic field \vec{H} . Experiments are performed on the trilayer with $t_{\text{NiO}} = 20$ nm at various

applied fields within the range of magnetization reversal and at magnetic saturation. The sample has been saturated in a magnetic field of ≈ -5000 Oe prior to the experiments. After this the field has been increased to the desired positive value. Fig. 1 shows the reciprocal space maps obtained for $H = 150$ Oe. Significant diffuse signal is observed in all four cross-sections. Only Yoneda scattering is present since the trilayers does not comprise a superlattice structure, which can lead to dynamical features like Bragg sheets. The diffuse scattering in the non-spin flip cross-sections does not allow to discriminate structural roughness from magnetic roughness unambiguously. Spin flip scattering is of pure magnetic origin. Thus, the observed diffuse scattering here indicates magnetic roughness, which is due to the formation of lateral domains when the magnetization reverses. A quantification of the distribution of domains will be obtained from modeling the 2D off-specular reflectivity maps using DWBA formalism [5].

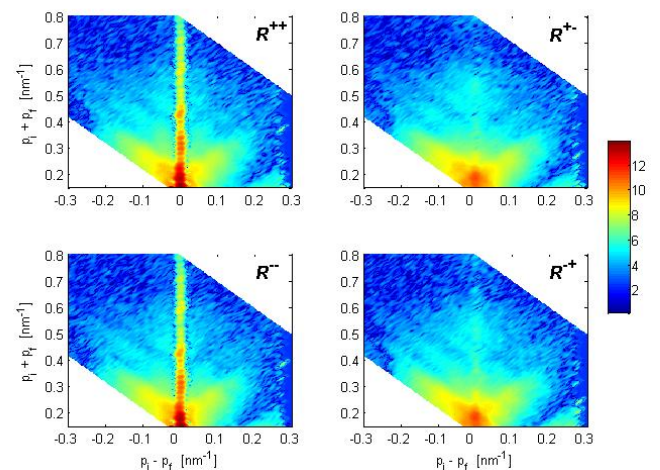


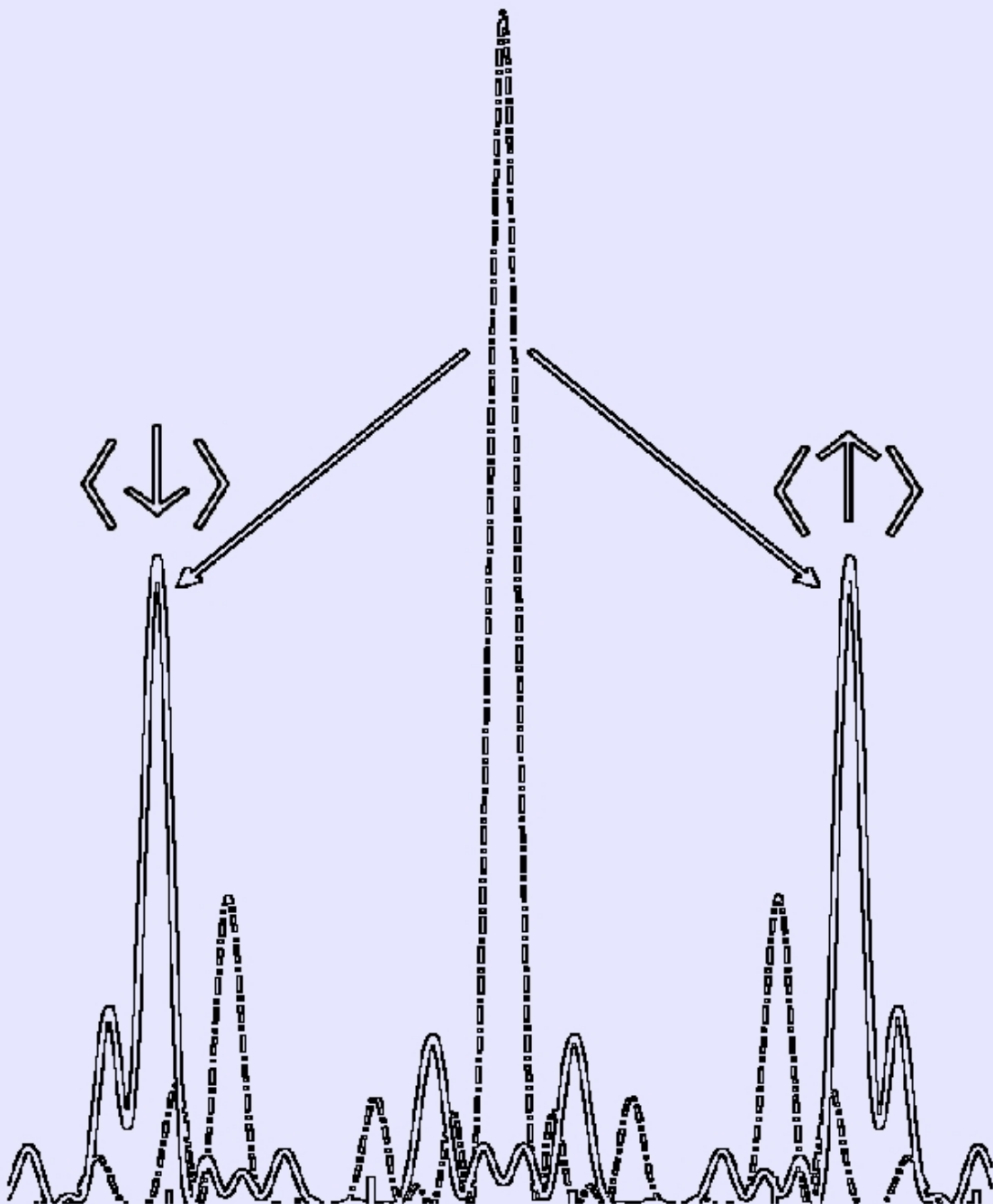
Figure 1: Reciprocal space maps of FeCoV/NiO(20 nm)/FeCoV trilayer. The four off-specular reflectivity maps are measured in a field of 150 Oe after the sample was saturated in a field of -5000 Oe. The intensities are colour coded in a logarithmic scale and $p_{i(f)} = k \sin(a_{i(f)})$.

References

- [1] F.Y. Yang and C.L. Chien. *Phys. Rev. Lett.*, 85:2597, 2000.
- [2] V. R. Shah, C. Schanzer, P. Böni, and H.B. Braun. Magnetization reversal in FM/AF/FM trilayers: dependence of AF thickness. *JMMM*, 286:484, 2005.
- [3] C. Schanzer, V.R. Shah, T. Gutberlet, M. Gupta, P. Böni, and H. B. Braun. *Physica B*, page 46, 2005.
- [4] K.H. Andersen, R. Cubitt, H. Humblot, D. Jullien, A. Petoukhov, F. Tasset, C. Schanzer, V. R. Shah, and A. R. Wildes. *submitted at ICNS 2005*.
- [5] B. Toperverg, O. Nikonov, V. Lauter-Pasyuk, and H. J. Lauter. *Physica B*, page 169, 2001.

3

Fundamental Physics



3.1 First MIEZE and Multi-MIEZE experiments at MIRA

Nikolas Arend¹, Robert Georgii^{1, 2}, Wolfgang Häußler^{1, 2}, Sebastian Mühlbauer¹,
Reinhard Schwikowsky², Heinz Wagensohner², Andreas Mantwill², Peter Böni¹

¹Physics Department E21, Technical University Munich, 85747 Garching, Germany

²ZWE FRM-II, Technical University Munich, 85747 Garching, Germany

In November 2005 a two-level Multi-MIEZE (Modulation of Intensity by Zero Effort) [1, 2] experiment was successfully performed at the instrument MIRA, using newly developed NRSE bootstrap coils and 10 Å neutrons. The whole assembly is shown in Fig. 1, including the two magnetic shieldings, coupling coils, polarizers, the scintillation detector and some of the electronic equipment.



Figure 1: Two-level MIEZE at MIRA.

Crucial components of any Resonance Spin Echo-based instrument are the NRSE coils. MIRA's bootstrap coils, one shown in Fig. 2, consist of two B_0 and RF coils each and were designed to allow for the usage of lower DC current by increasing the winding density. Furthermore, they feature high neutron transmission and low small angle scattering and should therefore be suitable for SANS measurements at MIRA in the future.

In order to verify the proper functioning of the coils and to find the exact resonance condition for the superimposed B_0 and RF fields (π -flip condition), the DC current is scanned against the RF amplitude. Fig. 3 shows a 3D plot of such a scan. The π -flip of the spins of the polarized neutrons happens at the minimum visible at the plot center. The well pronounced minimum and high symmetry of the plot indicate good homogeneity of both the B_0 and RF fields.

Fig. 4 shows the signals of the first single MIEZE stage (blue) and the two-level MIEZE (red). The RF synthesizers were phase-locked and running at frequencies of 54.5/109 kHz



Figure 2: One of MIRA's NRSE bootstrap coils, mounted inside the magnetic shielding and on top of the positioning mechanics.

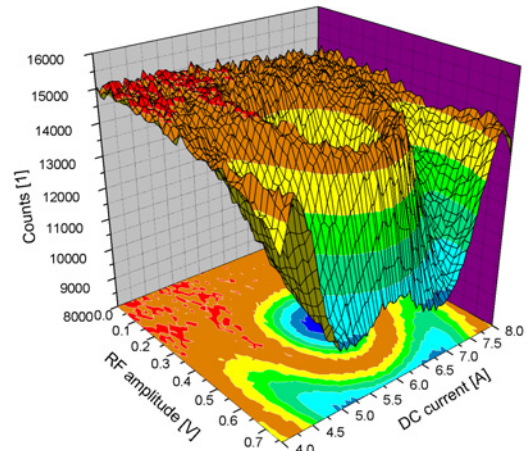


Figure 3: DC/RF amplitude scan at 109 kHz RF frequency.

(first level) and 109/218 kHz (second level). Please mind that due to beam time restrictions the two signals could not be measured with equivalent statistics. In the plot however they appear equally scaled for better viewing. The MIEZE signals had a polarization of approx. 41%. The Multi-MIEZE signal depicted here obviously does not show the predicted form calculated in [2], where a sharpening of the peaks was expected. The simple reason is that the phase of the RF synthesizers of the first and second MIEZE was not correctly adjusted. The signal as seen in Fig. 4 is the product of the signal from the first stage and the one from the second having twice the frequency, but the position of the peaks, time-wise, was out of sync. In that respect the observed signal does make perfect sense and measurements with properly tuned phases, resulting in the expected signal form, will be performed shortly at the beginning of 2006.

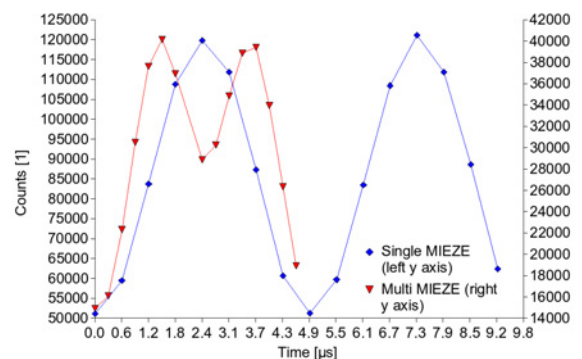


Figure 4: Measured MIEZE and Multi-MIEZE signals.

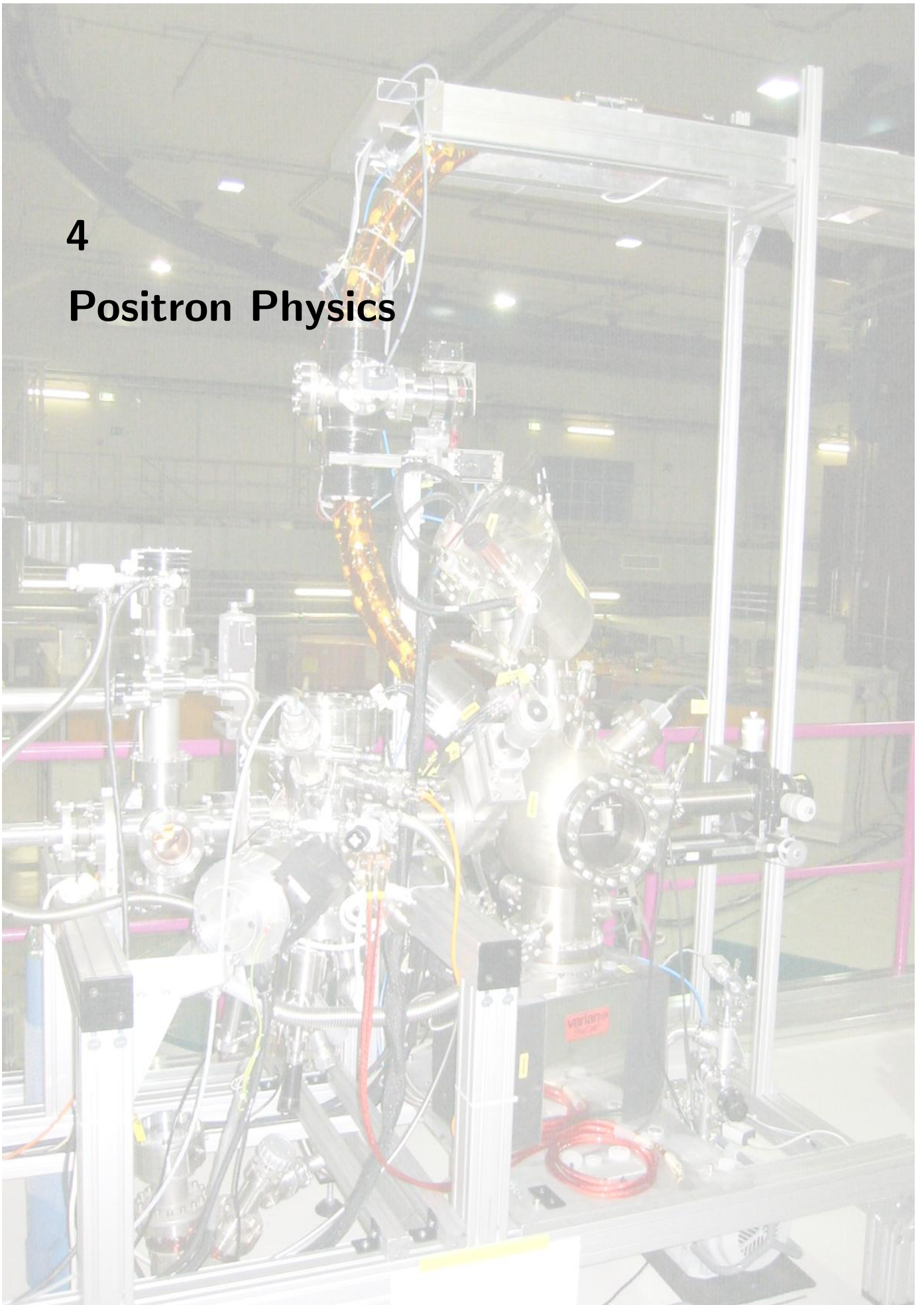
This work is kindly supported by the EU FP6 project under contract number HII3-CT-2003-505925, project JRA5/PNT.

References

- [1] Thomas Keller, Robert Golub, and Roland Gähler. In *Scattering and Inverse Scattering in Pure and Applied Science*, pages 1264–86. Academic Press, San Diego, CA, 2002.
- [2] N. Arend, R. Gähler, T. Keller, R. Georgii, T. Hils, and P. Böni. *Physics Letters A*, 327/1:21–27, 2004.

4

Positron Physics



4.1 First Experiments at the Positron Beam Facility NEPOMUC

Christoph Hugenschmidt^{1,2}, Thomas Brunner¹, Stefan Legl¹, Jakob Mayer¹, Christian Piochacz², Reinhard Repper², Martin Stadlbauer¹, Klaus Schreckenbach^{1,2}

¹Physics Department E21, Technical University Munich, 85747 Garching, Germany

²ZWE FRM-II, Technical University Munich, 85747 Garching, Germany

The mono-energetic positron beam of high intensity at NEPOMUC

In 2005 several positron experiments were performed at the high intensity positron beam facility at NEPOMUC (NEutron induced POsitrone source MUniCh). After adjustment of the positron beam the beam parameters such as diameter and intensity were determined at the first accessible position outside the biological shield. The positron yield was improved to a maximum beam intensity of $5 \cdot 10^8$ at a positron energy of 1 keV. The diameter in the longitudinal magnetic guide field of 6 mT was found to be less than 15 mm. We also succeeded to extract a low-energy positron beam at 15 eV with the world highest intensity of $4 \cdot 10^7$ moderated positrons per second.

The positron beam facility was extended by several components: μ -metal shielding at the straight sections of the beam line, a new adjustable aperture and an adiabatic beam switch in order to divide the beam line into five subsections. With this new switch up to five different positron experiments can be connected to the evacuated beam facility at the same time. This beam switch works in the energy range of 15 eV to 1 keV without considerable intensity loss.

Positron Experiments at NEPOMUC

The present arrangement of the experiments at NEPOMUC is shown in Fig. 1.

The positron beam is extracted at 1 keV for the coincident Doppler-broadening spectroscopy (CDBS), where the beam is focused to 1 mm at the sample position. Several material systems were studied – partially with external users – in or-

der to investigate the chemical surrounding at atomic defects: GaAs(Zn), Fe and Fe-alloys, and Mg-alloys (section 4.3).

The low-energy beam (15 eV) is required for positron annihilation induced Auger-electron spectroscopy (PAES) with low positron induced electron background. With this novel spectrometer positron annihilation induced Auger-electron emission was investigated at the surface of single crystalline silicon and poly-crystalline copper (section 4.4).

Within a diploma thesis a completely new time-of-flight configuration was connected to the beam line in order to enable PAES-measurements with much higher efficiency, that would lead to two orders of magnitude lower measurement time (section 4.5).

This year an apparatus for the production of the negatively charged positronium (Ps^-) was transferred from the Max-Planck-Institute for nuclear physics to the FRM-II. Recently this experimental set up was connected to the open beam port of the positron beam line in order to determine the diameter of the 500 eV positron beam at the position of the (Ps^-) production target.

In September 2005 we hosted the 1st user-meeting at TUM: *Workshop on Positron Physics*. Besides the visitation of the new positron beam facility NEPOMUC several talks from international experts in positron physics as well as fruitful discussions were concerned with the future of experiments with the high-intensity positron beam.

Acknowledgements

We acknowledge the support of our positron projects by BaCaTeC (68190-5) and by DFG HU 978/5-1.

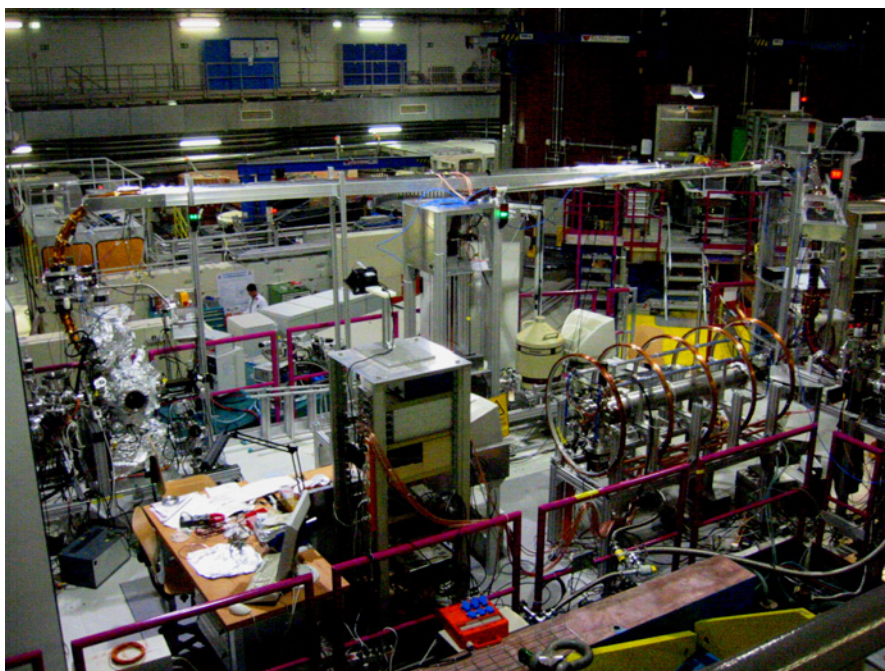


Figure 1: Overview of the positron beam facility NEPOMUC and the first installed experiments. CDB spectrometer and the PAES set ups are built and operated by E21/TUM. The (Ps^-) is operated by the Max-Planck-Institute for nuclear physics.

4.2 Positron remoderation facility for the slow positron beam at FRM-II

Christian Piochacz^{1, 2}, Christoph Hugenschmidt^{1, 2}, Klaus Schreckenbach^{1, 2}

¹Physics Department E21, Technical University Munich, 85747 Garching, Germany

²ZWE FRM-II, Technical University Munich, 85747 Garching, Germany

In summer 2004 the positron source NEPOMUC at the FRM-II has been set into operation. In order to enhance the brightness of the beam, a positron remoderator will be installed. The idea of using remoderation for brightness enhancement was first described by [1].

For the remoderation process, positrons are guided and focused on a solid, where they stop and thermalize. There is a certain possibility that thermalized positrons diffuse to the surface where they leave the solid with a sharp energy and a small angular divergency. The whole process depends on the properties of the solid, which is used for moderation. Materials, such as tungsten, nickel and platinum are known to be efficient positron moderators. There are basically two possibilities for remoderating a positron beam, depending on which surface the positrons are emitted: reflection or transmission geometry.

The moderator built up works in transmission geometry with a 100 nm thin tungsten single crystalline foil. The moderated positrons leave the foil surface with an energy of about 3 eV and an angular spread of about 8°.

Experimental setup

The setup is shown in Fig. 1. The positrons are focused by adiabatic magnetic field compression, i.e. the positrons follow the compressed magnetic field by a gyration motion leading to a smaller beam. The increasing magnetic field is achieved by conventional copper coils whereas the high magnetic field of about 268 mT is realized by a water cooled copper coil. The positrons leave the high magnetic field after moderation non-adiabatically in order to conserve the small diameter of the beam. This magnetic field termination is implemented by an aperture made of mu-metal.

Advantages of the chosen design

Transmission remoderators require much simpler beam guiding fields unlike the reflection geometry solutions. Due to the small beam diameter after moderation the termination of the magnetic field is done just by an aperture made of mu-metal. Beams with a great transversal impulse and/or a broad energy spread can be focused and hence remoderated. This is more difficult with electric or magnetic lenses and would lead to complex lens systems in order to avoid lens aberrations.

The working parameters of the moderator (e.g. coil currents) depend only on the properties of the primary positron beam.

Results

After successful simulations of the magnetic and electric fields the device was built up and the magnetic fields were measured. Based on these measurements the magnetic fields were optimized and the compression capability demonstrated with the assistance of an electron beam source. A beam diameter of about 1.3 mm was achieved. Also the remoderation of positrons was successfully accomplished at the ²²Na based positron beam in the laboratory but the remoderation efficiency was lower than expected and also the extracted beam didn't show the expected parameters. This is basically attributed to the insufficient quality of the remoderation foil. Further the field termination might not be efficient enough and due to that the remoderated positrons are not extracted completely out of the high magnetic field.

Thus further examinations are necessary. Especially measurements with a superior foil and raytracing simulations in the area of field termination are needed.

References

- [1] A. P. Mills Jr. Brightness enhancement of slow positron beam. *Appl. Phys.*, 23:189, 1980.

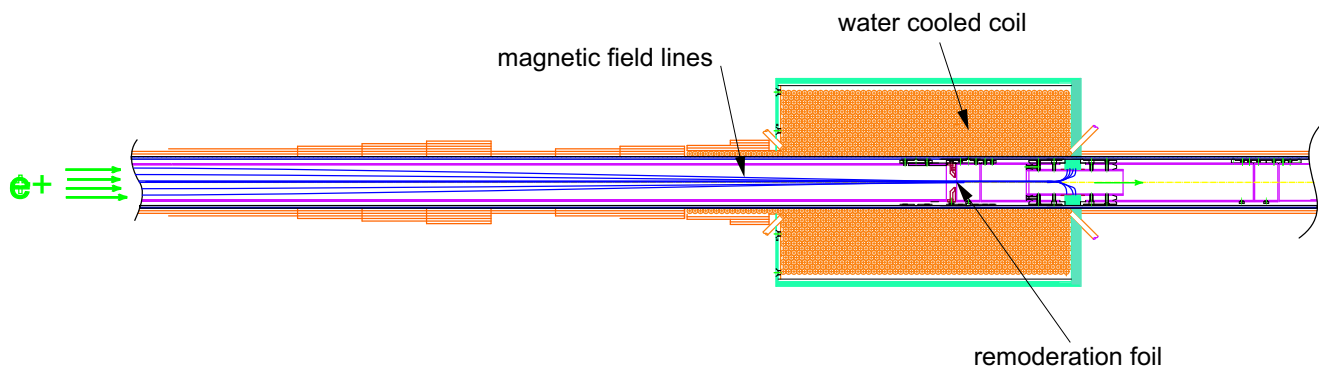


Figure 1: Cross-sectional view of the positron beam remoderator. The primary beam from the left is focused by the compressed magnetic field lines. After moderation the positrons leave the area of high magnetic field non-adiabatically in order to conserve the small diameter of the beam. The moderating foil (100 nm W(100)) is near the centre of the big coil block. The magnetic field lines (blue) are only schematically.

4.3 Measurements on Mg-Alloys with the Coincident Doppler Broadening Spectrometer CDBS

Martin Stadlbauer¹, Christoph Hugenschmidt^{1, 2}, Klaus Schreckenbach^{1, 2}, Peter Böni¹

¹Physics Department E21, Technical University Munich, 85747 Garching, Germany

²ZWE FRM-II, Technical University Munich, 85747 Garching, Germany

Experimental Setup

During 2004 a new coincident Doppler broadening spectrometer (CDBS) was set into operation at the high intense positron source NEPOMUC. The positron beam is guided in a longitudinal magnetic field to the analysis chamber and nonadiabatically released from this field by a magnetic field termination. After passing an aperture of 3 mm diameter, electrical lenses focus the divergent positron beam onto the sample where a focus diameter of 1 mm was achieved.

Since the high momenta of the electrons in the sample endue high momenta compared to the thermalized positrons, the 511 keV annihilation radiation is Doppler-shifted. By measuring this Doppler shift with high purity germanium detectors, the electron momentum distribution at the annihilation site can be investigated. At high Doppler shifts, i.e. regions of the annihilation line with very low count rate, information about the chemical surrounding of the annihilation sites - for example open volume defects - can be revealed [1, 2]. Therefore, the CDBS is equipped with two facing germanium detectors in coincidence in order to reduce background.

Characterization of the Focus

In order to investigate the focus parameters at the sample position, an aluminum sample with glued on tungsten stripes was investigated with the CDBS since aluminum and tungsten have very different electron momentum distributions. The S-parameter - a quantity that measures the width of the annihilation lines - was recorded depending on the position of the positron beam spot on the sample at a potential of -20 kV. The result is shown in Fig. 1.

The sharp edges of the borders between aluminum and tungsten become smooth transitions in the S-parameter picture since the beam diameter shows a certain extension. The area of this transitions allows to estimate the beam diameter

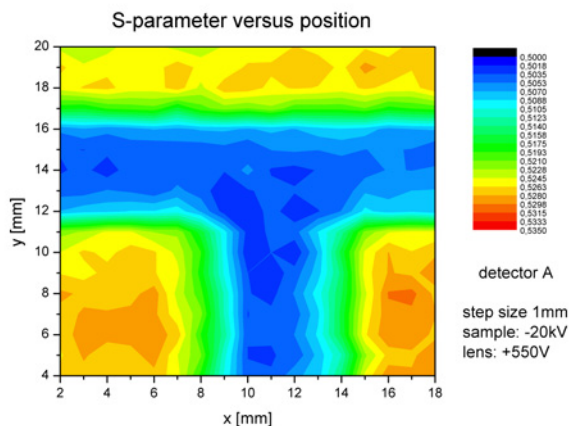


Figure 1: S-parameter vs. position of the focused positron beam on an aluminum sample with glued on tungsten stripes. This picture was recorded at a sample potential of 20 kV with a focal diameter of 2 mm.

in the x and y direction. Fig. 1 shows clearly a beam diameter of about 2 mm. By inserting an additional aperture a focus of 1 mm was achieved.

Measurements on Mg-Alloys

Mg-alloys experience an increasing interest for industrial applications due to their very low specific weight, high elasticity and mechanical strength. The CDBS is an ideal tool for investigating the behaviour of the alloy constituents, i.e. aluminum and zinc. If the concentration of one of the alloy constituents changes in the vicinity of open volume defects, the structure of the annihilation line should change in the high momentum region.

First measurements were recorded of the pure and annealed metals aluminum, zinc and magnesium in order to get reference spectra. These annihilation lines were compared with AZ31, a diecast Mg-alloy consisting of 1% wt. zinc and 3% wt. aluminum and normalized to magnesium. The result is shown in Fig. 2.

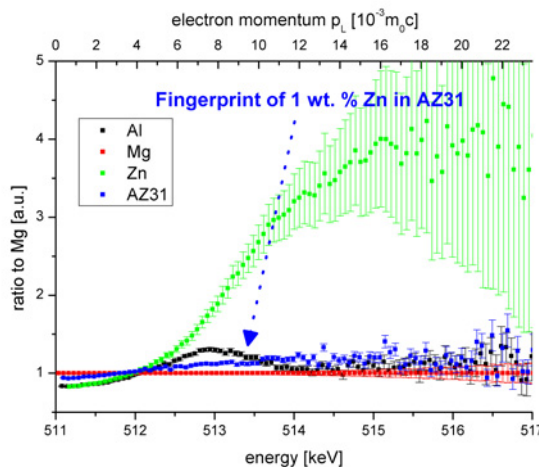


Figure 2: Annihilation lines of annealed aluminum, zinc, magnesium and AZ31-samples, normalized to magnesium. The line of AZ31 is shifted towards the line of zinc, which proves that even in defect free material, 1% wt. of zinc can be detected.

The lines of the pure elements can be clearly separated from each other. Especially zinc shows a large deviation compared to magnesium and aluminum at high momenta. The structure of the AZ31-line is clearly shifted towards the line of zinc due to the 1% wt. zinc atoms in the sample. Consequently even in defect-free samples zinc can be detected.

References

- [1] P. Asoka-Kumar, M. Alatalo, V. J. Ghosh, A. C. Krusemann, B. Nielsen, and K. G. Lynn. *Phys. Rev. Lett.*, 77:2097-2100, 1996.
- [2] M. Stadlbauer, C. Hugenschmidt, C. Piochacz, B. Strasser, and K. Schreckenbach. Spatially resolved investigation of thermally treated brass with a coincident doppler-spectrometer. *Appl. Surf. Science*, accepted for publication.

4.4 PAES - Positron Annihilation induced Auger Electron Spectroscopy

Jakob Mayer¹, Christoph Hugenschmidt^{1, 2}, Benno Straßer², Klaus Schreckenbach^{1, 2}

¹Physics Department E21, Technical University Munich, 85747 Garching, Germany

²ZWE FRM-II, Technical University Munich, 85747 Garching, Germany

Principle of PAES

Auger Electron Spectroscopy (AES) is a commonly used technique in surface science. Since in AES the Auger process is induced by high energy (1 keV) electrons or X-rays, the spectra contain a large secondary electron background. Hence it is very difficult to identify Auger peaks in the low-energy region.

A new method to initiate the Auger process is the annihilation of low energy (some 10 eV) positrons with electrons. **PAES (Positron annihilation induced Auger Electron Spectroscopy)** has several advantages compared to conventional AES: First, there is no positron induced secondary electron background at $E_{e^-} > E_{e^+}$ due to the low kinetic energy of the positrons. Secondly, tightly bound adsorbates at the surface are barely destroyed by the incident e^+ -beam. The

greatest advantage of PAES is the extremely high surface sensitivity since most of the slow positrons (> 90%) annihilate with electrons of the topmost atomic layer.

The challenge in PAES is to produce a e^+ -beam of high intensity. Since usual laboratory e^+ -sources provide only about $10^4 e^+/s$ measurement times of 20 days per spectrum or more are necessary.

Experimental setup at NEPOMUC

The new positron-beam NEPOMUC at the research reactor FRM-II provides a low energy-beam of $5 \cdot 10^7$ moderated positrons per second at the analysis chamber. Due to the high beam-intensity the measurement time is reduced to several hours. The existing spectrometer (Fig. 1) was transferred to the reactor in the end of 2004.

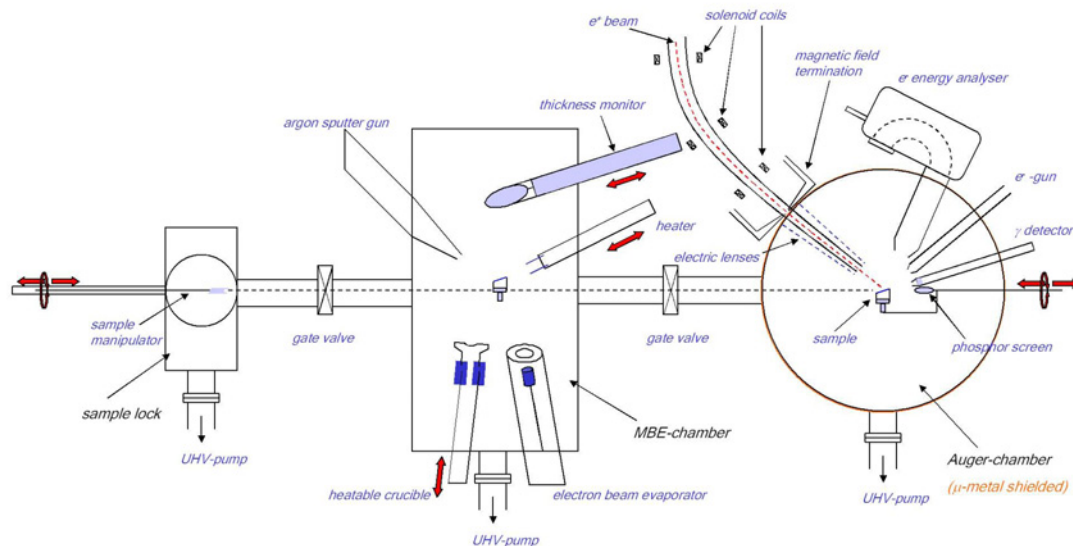


Figure 1: Drawing of the PAES-facility at the FRM-II

Measurements and results

There have already been first successful measurements and the results are shown below. The surface sensitivity of the method can be seen at the single-crystal Si sample (small spectrum plot in Fig. 2). With only one monolayer of copper on it, the Auger-peak of the Si (at 89 eV) completely vanishes. The other spectrum shows polycrystalline copper, which was Ar-sputtered for a clean surface. The measurement time for all shown spectra was 13 hours and the pressure in the chamber was about 10^{-9} mbar. Unfortunately the background was higher than expected, that might be attributed to other experiments nearby and insufficient shielding.

Outlook

In the following year, the aim is to find the true surface sensitivity (qualitatively) for different samples and coatings and to reduce the background. Besides a better shielding, coincident measurements (Auger-electron and annihilation-radiation) of

the electrons would be the best way to achieve a better signal/noise ratio.

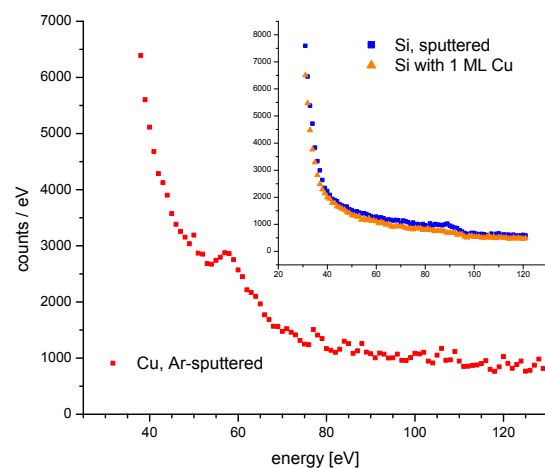


Figure 2: Cu, Si and Si with Cu using PAES.

4.5 Time of flight spectroscopy of positron induced Auger electrons

Stefan Legl^{1, 2}, Christoph Hugenschmidt^{1, 2}, Reinhard Repper²

¹Physics Department E21, Technical University Munich, 85747 Garching, Germany

²ZWE FRM-II, Technical University Munich, 85747 Garching, Germany

Auger electron spectroscopy

Auger electron spectroscopy (AES) is a widely used method in surface physics. X-rays or high energy electrons are used to excite core electrons of a material. These electrons are emitted into vacuum. When electrons from higher shells take their places binding energy is released and can be transferred to a valence bond electron which is also emitted into vacuum. This so called Auger electron has a specific kinetic energy. By analyzing these energies one can determine the elemental composition of the top layers of the sample.

Positron induced Auger electron spectroscopy (PAES) uses low energy positron annihilation (15 eV) to create the e^- hole in the inner shell. The following e^- emission process is the same as in AES.

To analyze the energy of the Auger electrons mostly hemispherical energy analyzers are used. Due to their small solid angle (typically $\geq 0,1\%$) and the necessity to scan over certain energy ranges in ≥ 0.1 eV steps one needs several hours (using an intense positron source like NEPOMUC at the FRM-II) or even weeks (at the lab with a β^+ -emitter) to obtain an Auger spectrum [1]. In order to reduce this measurement time to less than one hour we developed a new spectrometer using a time of flight method for analyzing the Auger energies.

Experimental setup

Positrons entering the flight tube are deflected in a trochoidal ExB-filter upwards (Fig. 2). When they leave the filter their longitudinal momentum lies exactly on the axis of the flight tube where also the sample is placed. Additionally the positrons are focussed onto the sample by the magnetic field gradient caused by a strong NdFeB₂ permanent magnet that is placed behind the sample. When a positron annihilates with a core electron two gamma quanta are created (511 keV) and simultaneously the Auger electron is emitted. If one of these gamma quanta hits the BaF₂ detector the timing is started. The Auger electron emitted from the surface of the sample travels through the trochoidal filter in the opposite direction of the positron trajectories. Therefore, the e^- is deflected upwards where it hits a micro channel plate (MCP) when it leaves the filter. This MCP creates the stop signal for the

timing. The recorded TOF spectrum can be transferred into an energy spectrum of the Auger electrons.

The inhomogenous magnetic field between the sample and the trochoidal filter has two important functions. Positrons leaving the filter are captured and adiabatically focussed onto the sample. The second and much more important effect is that all emitted Auger electrons from a solid angle of 2π (!) are focussed towards the filter. Hence each emitted electron can reach the micro channel plate. The physical explanation for this is the following: Due to conservation of the magnetic moment and conservation of energy, in an inhomogenous magnetic field longitudinal momentum is converted into transversal momentum (flight direction towards the stronger field) and vice versa (flight direction towards the smaller field).

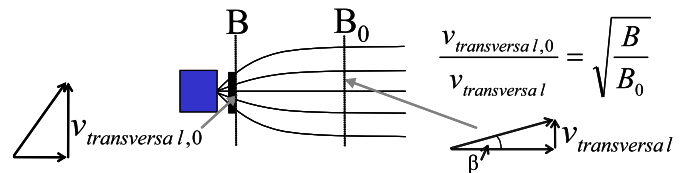


Figure 1: Momentum in an inhomogenous magnetic field

These two effects guarantee a high count rate and together with the ability to measure a large energy range simultaneously we expect a measuring time for an Auger spectrum of less than one hour.

Conclusion and Results

So far the experimental setup has been completed and first measurements at the intense positron source NEPOMUC were performed this year. Focussing positrons on the sample was optimized in a first step. Our measurements showed a number of 10^7 positrons per second hitting the sample, the intensity of the positron beam is also in this range. Therefore, it is concluded that the beam guiding system works extremely efficiently. In a second step we showed that electrons emitted from the sample reach the MCP. Presently, the electronics is adjusted in order to record first TOF spectra.

References

- [1] Benno Strasser. *Aufbau einer Anlage zu positroneninduzierten Auger-Elektronenspektroskopie*. PhD thesis, Technische Universität München, 2002.

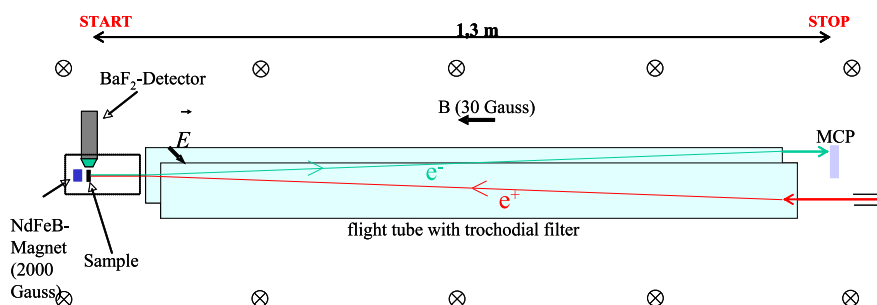
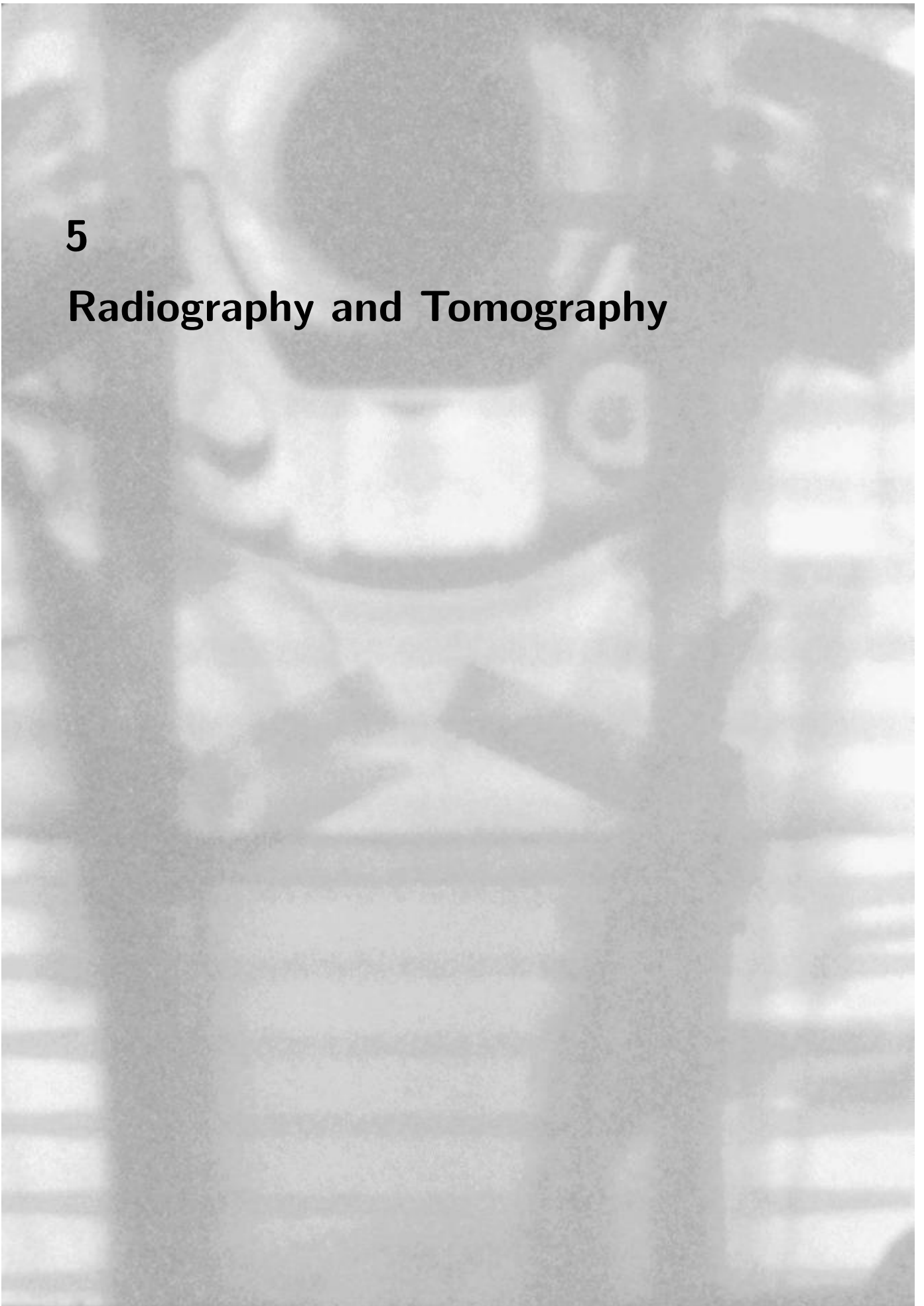


Figure 2: Experimental setup of the TOF-PAES



5

Radiography and Tomography

5.1 Neutron phase contrast imaging at ANTARES

Klaus Lorenz¹

¹ Physics Department E21, Technical University Munich, 85747 Garching, Germany

Design efforts

With the installation of the aperture wheel (Fig. 1) the facility for radiography and tomography ANTARES became ready for phase contrast imaging [1]. The aperture wheel enables the user to select quickly between eight apertures: open beam, three pinholes with diameters of 1, 2 and 7 mm, a horizontal 1 mm slit, two coded apertures and a 2 mm thick cadmium filter.

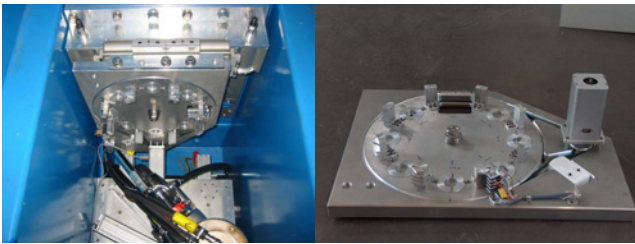


Figure 1: The new designed aperture wheel (left) at its final position in the ANTARES beam line (right).

With the pinholes the neutron beam has an L/D ratio between 2000 and 14000 at the sample position, which has a distance of about 14 m to the aperture wheel. Looking at the cold source of the FRM-II, the resulting transversal spatial coherence length is in the order of several micrometers, which is sufficient to get a clearly visible phase contrast effect (Fig. 2) [2].

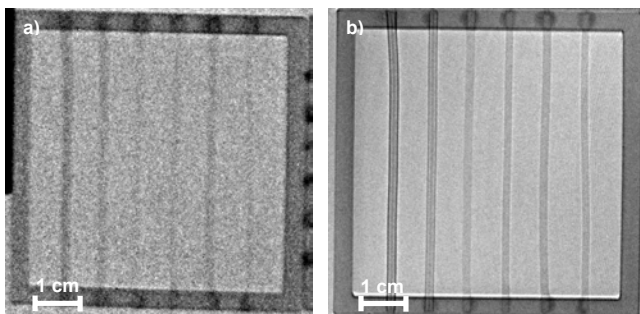


Figure 2: Comparison of a phase contrast radiography with CCD (left) and image plate detector (right) (30 min exposure time).

With the coded apertures [3] and the horizontal slit, new techniques for phase contrast imaging are investigated, which can reduce the necessary exposure times. The cadmium filter is used to suppress cold and thermal neutrons to be able to do imaging with epithermal neutrons. This is especially useful to penetrate thicker samples and to reduce the activation of the sample.

The 1 mm pinhole reduces the neutron flux at the sample position by a factor of 1000 and increases the exposure time for radiography by the same factor. First measurements with such long exposure times revealed two problems. The first is the gamma flux from the beam tube nozzle, the second is a high noise level on the CCD detector due to secondary radiation. Measurements with a MAR345 image plate detector, which SPODI has lent us for some days (thanks again!), have not shown this high background level (Fig. 2). A new camera box for our CCD detector system with a $40 \times 40 \text{ cm}^2$ scintillator is under construction, where high effort is made to suppress the secondary radiation problem.

To solve the first mentioned gamma ray problem, a bismuth filter was constructed and will be installed at the end of this year. With a thickness of 50 mm it reduces the neutron flux by a factor of three, while 99% of the gammas up to 800 keV are blocked.

Applications

Besides for non-destructive testing of metal foams, phase contrast imaging has proven to be a powerful technique to separate different aluminium alloys. Fig. 3 shows a phase contrast radiography of the sample which is sketched on the right side. The material of the inner step wedge (AlMg_{4.5}Mn) has a very similar attenuation coefficient like the material that was cast around it (AlSi₉Cu₄). The plateaus have the same mean grey values, but due to the fact that Manganese causes a negative and Copper a strong positive phase shift, phase contrast occurs at the steps.

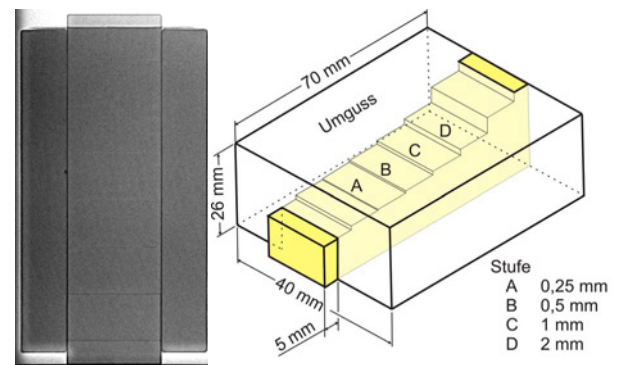


Figure 3: Phase contrast radiography and schematic of an AlMg_{4.5}Mn/AlSi₉Cu₄ test phantom.

References

- [1] John M. Cowley. In *Diffraction Physics*. Elsevier, Amsterdam, Netherlands, 1995.
- [2] Eberhard Lehmann, Klaus Lorenz, Erich Steichele, and Peter Vontobel. Non-destructive testing with neutron phase contrast imaging. *Nucl. Instr. and Meth. in Phys. Res. A*, 542:95–99, 2005.
- [3] A. R. Gourlay and N.G. S. Young. Coded aperture imaging: a class of flexible designs. *Applied Optics*, 23:4111, 1984.

5.2 A study of oil lubrication in a rotating engine using stroboscopic neutron imaging

Burkhard Schillinger^{1, 2}, Johannes Brunner^{1, 2}, Elbio Calzada^{1, 2}

¹Physics Department E21, Technical University Munich, 85747 Garching, Germany

²ZWE FRM-II, Technical University Munich, 85747 Garching, Germany

Even at modern high-flux neutron sources, the required exposure time for one neutron radiography image with high counting statistics is in the order of one second. Continuous time-resolved imaging of objects in motion is thus very limited in time resolution and signal dynamics. However, repetitive motions can be recorded with a stroboscopic technique: A trigger-able accumulating detector is triggered for many identical time windows of the cyclic motion until sufficient fluence is accumulated for one image. The image is read out, the delay for the time window is shifted and the recording repeated until a complete movie of the cyclic motion can be put together. We report about a study of oil flux in a running, electrically driven BMW engine out of current production.

Introduction

The neutron radiography facility ANTARES at FRM-II delivers a cold flux of $108 \text{ n/cm}^2\text{s}$ at a collimation ratio of $L/D = 400$. Considering a time window as long as one millisecond and a scintillator detection efficiency of 30%, only $3.3 \times 10^5 \text{ n/cm}^2\text{s}$ are detected on a square centimeter. If an area of $0.3 \text{ mm} \times 0.3 \text{ mm}$ is imaged onto one pixel of the detector, only 300 are detected on a single pixel. This signal is not sufficient for a useful radiography image with attenuations from zero to a factor of 1000.

The only way to increase the counting statistics is to use a stroboscopic imaging technique to record a periodic motion. The signal of many time windows identical within the cycle of the examined motion is accumulated on a trigger-able detector before the signal is digitized and read out, until sufficient counting statistics is achieved.

Experimental setup

For our studies, we obtained a NG4 BMW engine out of current production. The engine was stripped of the intake and exhaust system and was coupled to a 2 kW electric motor with a transmission belt. The spark plugs were removed, so that the engine would not generate compression in its cylinders. Only this way, the comparatively weak electric motor was capable of turning the engine at low rotation speeds, and due to the reduced heat production, the water cooling could be omitted. Instead of using the spark distributor to generate a synchronization signal, we mounted a hall sensor close to the transmission wheel on the camshaft. The generated pulse was used to trigger the image intensifier of a cooled CCD camera. With the camera electronics and software, the trigger signal could be delayed in order to shift the time window within the cycle of the engine.

Measurements at ANTARES

The detection system was an Andor iStar MCP intensified CCD camera with 1024×1024 pixels [1]. Of special interest is the visualization of the oil cooling of the piston bottoms.

Since the pistons are only connected to the engine body via the piston rings with very low heat dissipation, a continuous oil jet is directed from below at the piston bottoms, lowering the piston temperature by more than $200 \text{ }^\circ\text{C}$.

Because of the limited flux, the time window was selected as high as one millisecond, the rotation speed was selected as 600 rpm, which is well below the nominal idle speed of the engine. The images thus show motion unsharpness, but good definition on the stationary parts.

At this rotation speed, the oil pump did not produce its nominal pressure, the oil pressure was pulsed and produced blobs in the cooling oil jet. In the field of view of $25 \text{ cm} \times 25 \text{ cm}$, the nozzles for the cooling oil jets were visible along with the horizontal pressure tube. The area between the pistons contains the vertical tubes for the pressure-free backflow of oil from the camshaft on top to the oil pan at the bottom of the engine. In the car, these tubes are mostly empty, because the engine is mounted at a 30 degree tilt angle. On our test stand, the engine was mounted vertically, resulting in a fill-up of these tubes.

Fig. 1 shows a static radiography of the engine, showing valves, pistons, piston rods, piston pins and piston rings, with the pressure tubes and backflow channels empty. Fig. 2 shows one single frame of the engine in motion, viewing different cutouts. An oil blob is visible on its way to the piston bottom, the horizontal pressure tube for the supply of the oil ejection nozzles and the vertical backflow tubes are filled up.

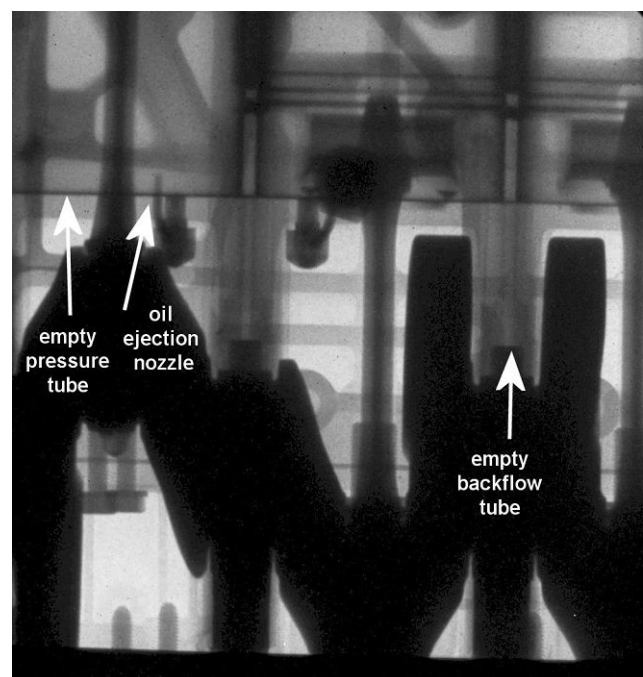


Figure 1: Static neutron radiography image of the engine.

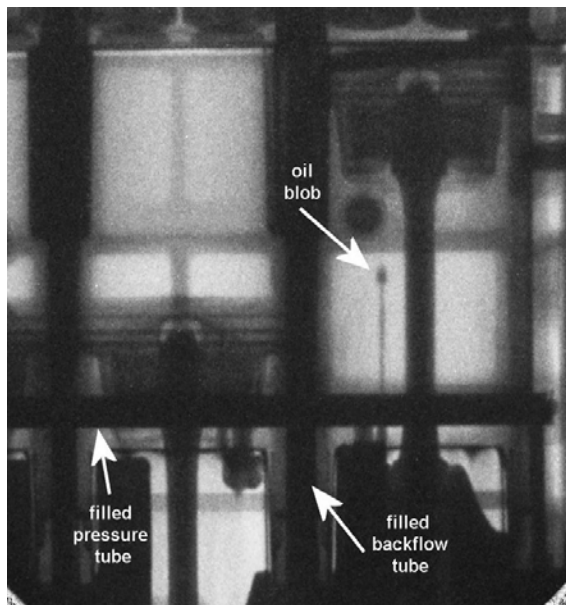


Figure 2: Dynamic neutron radiography image of the engine.

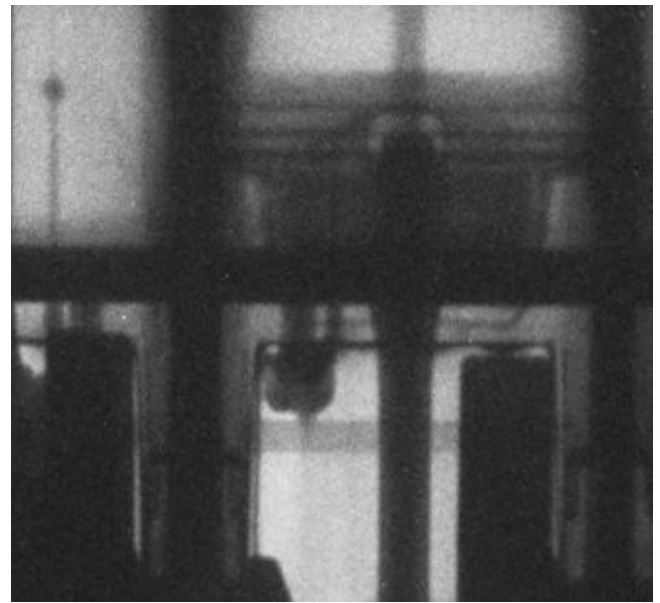


Figure 4: Dynamic neutron radiography cutout.

Fig. 3 and 4 show a static and a dynamic cutout for comparison. The vertical backflow tubes which are mounted on the outside of the engine block extend beyond the edges of the cylinder bore and cover the edges of the pistons, making it impossible to observe the oil film on the pistons in motion in this 90° view.

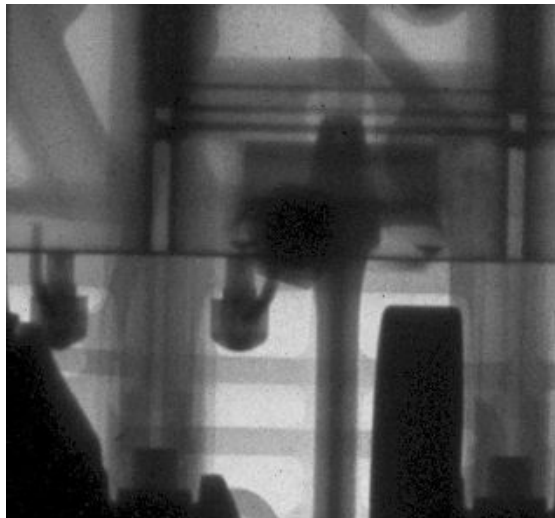


Figure 3: Static neutron radiography image cutout.

In the running engine, the transmission through the free areas besides the crankshaft is only half of the static transmission, meaning non-repetitive oil splashes and foams obstruct the view. As repetitive phenomenon, curtains of oil are visible flowing down the cylinder walls.

The lubrication of the camshaft bearings would also have been of interest, but the engine has a plastic cover on top which obstructs the neutron view to this area. Further tests will be performed with an Aluminium replacement cover.

Outlook

Stroboscopic neutron radiography has proved its potential for further examinations of the lubrication of running engines. In a realistic experiment with compression, heat generation will cause difficulties, as filling the cooling system with water will obstruct part of the view. A partial solution may be the use of heavy water in the cooling system. To avoid exhaust fumes in the reactor hall, an external electric motor will be required which must equal the nominal power of the engine to drive it at high rotational speeds.

References

- [1] Andor. <http://www.andor.com>.

5.3 Multiple radiation measurements at the radiography facility ANTARES

Burkhard Schillinger^{1, 2}, Elbio Calzada^{1, 2}, Martin Mühlbauer^{1, 2}, Michael Schulz^{1, 2}

¹Physics Department E21, Technical University Munich, 85747 Garching, Germany

²ZWE FRM-II, Technical University Munich, 85747 Garching, Germany

Although the neutron radiography and tomography facility ANTARES is designed for measurements with thermal and cold neutrons, the use of additional filters and an X-ray tube allows for measurements with epithermal neutrons, with 300 kV X-rays and with gamma radiation from the reactor core and from the beam nozzle.

Thermal and cold neutrons

ANTARES (Fig. 1) is situated at the beam line SR4b, facing the cold source of the reactor. A vertical secondary shutter contains two steel collimators of 1 m length and roughly 20 mm and 40 mm diameter to optimize between high resolution and high flux (Fig. 2).

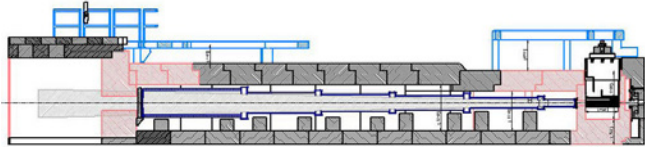


Figure 1: Vertical cross section of the ANTARES facility.

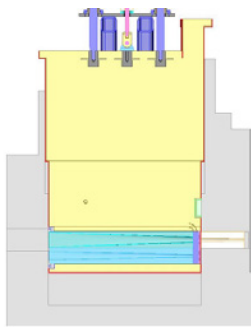


Figure 2: Vertical cross section of secondary shutter.

Fig. 3 shows a neutron radiography of a pressure reducer. Thermal and cold neutrons are ideally suited to penetrate thick layers of Aluminium and to show organic compounds like sealants, O-rings and adhesives. Fig. 4 shows a neutron radiography of an oil-filled pump. The oil layer is practically impenetrable for cold neutrons, and also the steel parts show a lot of attenuation. On the top left, a plastic plug is visible in a valve.

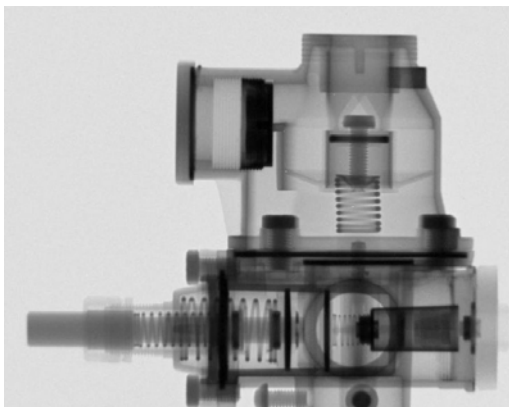


Figure 3: Thermal/cold neutron radiography of a pressure reducer.

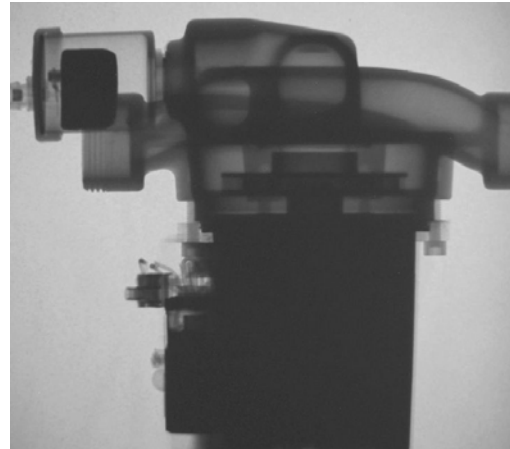


Figure 4: Thermal/cold neutron radiography of an oil-filled pump.

Epithermal neutrons

After the secondary shutter, a filter wheel with different pinhole diaphragms is installed. One of the positions is equipped with a 2 mm Cadmium sheet (Fig. 5), which will absorb all neutrons with energies below 0.4 eV. The scintillation screen employed in the detection system is sufficiently sensitive for epithermal neutrons as well, although the measuring time increases by a factor of ten. In Fig. 6, the steel parts show better penetration, and some outlines are visible through the oil.

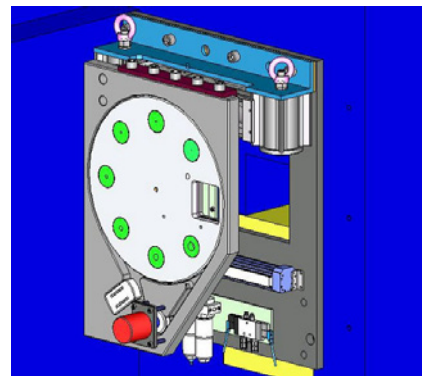


Figure 5: The selector wheel with the Cadmium filter.

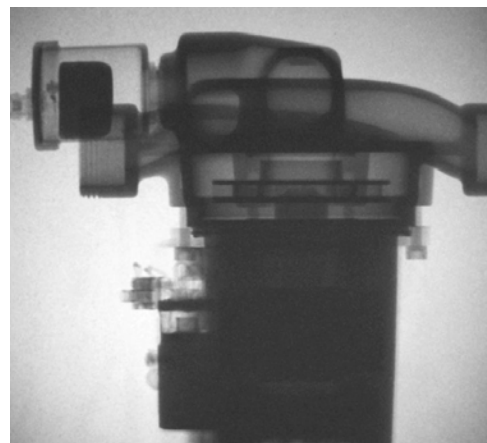


Figure 6: Epithermal neutron radiography of the pump.

Gamma radiation

Between the secondary shutter and the filter wheel, a pneumatic fast shutter (Fig. 7) is installed to shut off the thermal and cold flux during short breaks such as repositioning or rotating of the sample or data readout times in order to keep the sample activation as low as possible. It consists of a container filled with boron carbide. The shutter will absorb all cold and thermal and a wide range of epithermal neutrons, but can be easily penetrated by fast neutrons and gamma radiation originating from the reactor core and from the neutron absorption in the beam tube nozzle.

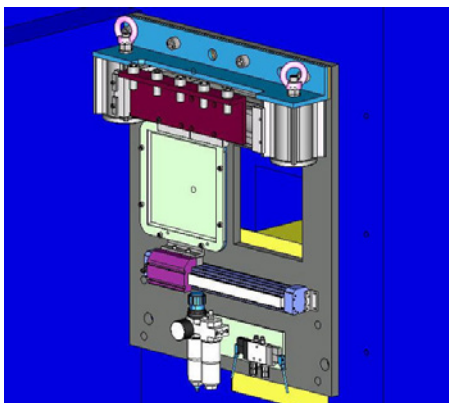


Figure 7: The Boron Carbide fast shutter.

The prompt gamma radiation from neutron capture in Aluminium has a very high energy up to 8 MeV. If the neutron scintillation screen is replaced by a standard medical X-ray scintillation screen made of Gadolinium oxysulfide, we can obtain gamma radiographies with a very high penetration also for steel (Fig. 8). The efficiency of the screen drops towards high energies, the exposure time is in the order of minutes. Fig. 8 shows high penetration even for the steel body of the pump, the plastic body in the valve is faintly outlined, probably due to some remaining sensitivity for fast neutrons, the oil filling is virtually invisible. Some fingerprints on the scintillation screen were removed only after the measurement.

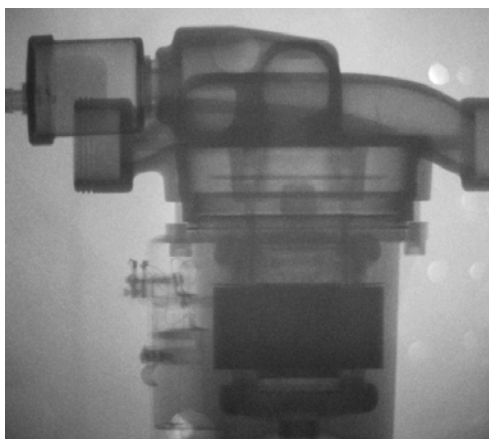


Figure 8: Gamma radiography of the pump.

X-ray tube

For standard measurements, a removable 320 kV X-ray tube (Fig. 9) has been mounted on a sliding system between the filter wheel and the flight tube. With the X-ray scintillation screen mentioned above, high-quality X-ray images can be

obtained in about 30 seconds measuring time. Fig. 10 shows a ski boot as an example.

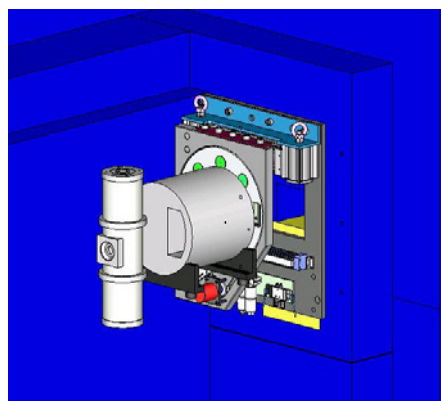


Figure 9: The X-ray tube in the beam path.

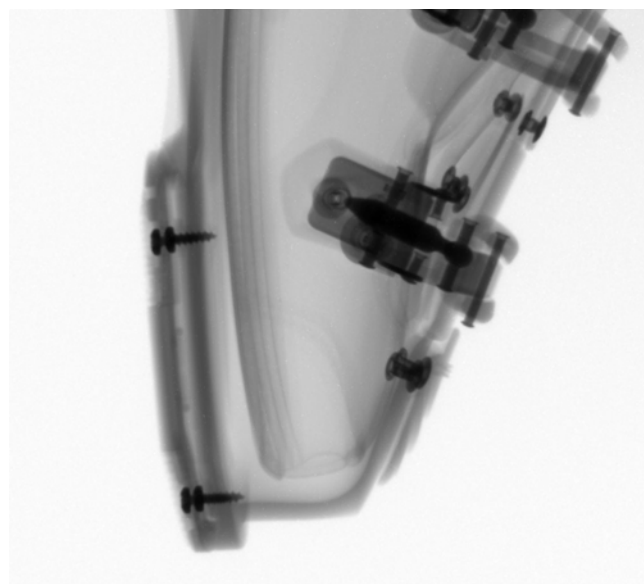


Figure 10: X-ray radiography of a ski boot.

The positioning of the tube in the beam path in 12 m distance wastes a lot of X-ray intensity, but assures exactly the same quasi-parallel beam geometry as for neutrons. Images recorded that way can be superposed to neutron images without the need for any adjustment or registering.

Fig. 11, 12 and 13 show a photo, a neutron and X-ray radiography of a printed circuit board, Fig. 14 shows the X-ray image subtracted from the neutron image.

Conclusion

ANTARES offers a multitude of possibilities for measurements with different radiations, which can be selected according to the problem at hand. While the instrument is of course optimized for thermal and cold neutrons, a lot of additional information can be obtained with different radiations. All images are perfectly congruent and can be superposed without further adjustment.

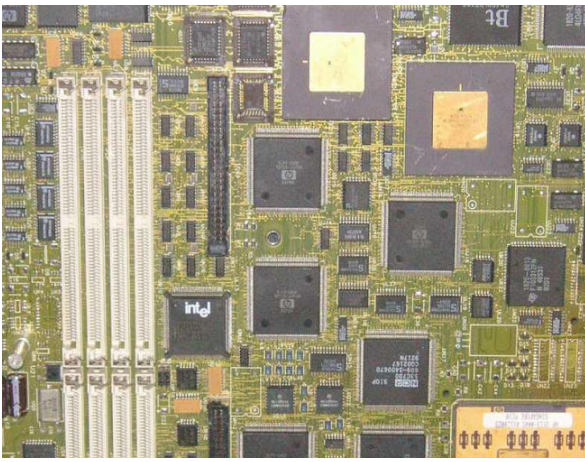


Figure 11: Photo of a computer board.

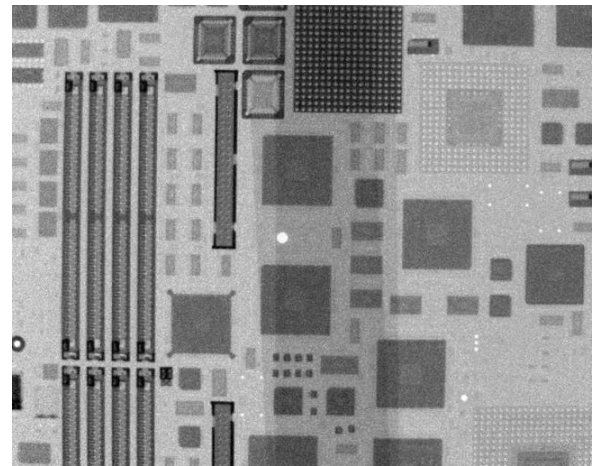


Figure 13: Neutron radiography.

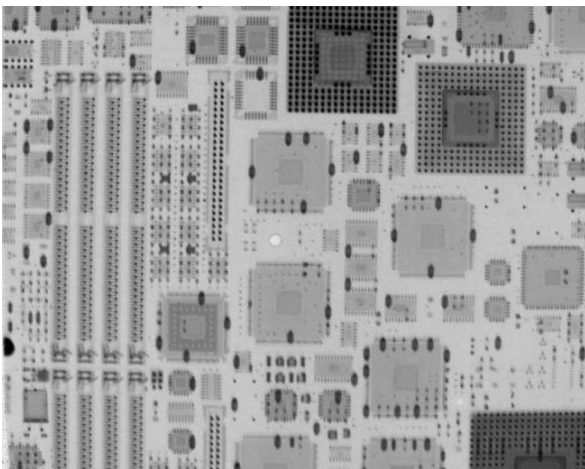


Figure 12: X-ray radiography.

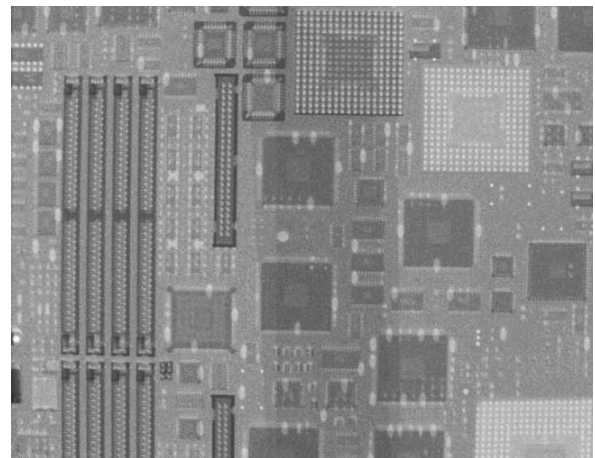


Figure 14: The X-ray image subtracted from the neutron image.

5.4 Small-angle scattering effects in neutron radiography and tomography

Burkhard Schillinger^{1, 2}, Elbio Calzada^{1, 2}, Roland Gähler³, Hongyun Li^{1, 4},
Martin Mühlbauer^{1, 2}, Michael Schulz^{1, 2}

¹ Physics Department E21, Technical University Munich, 85747 Garching, Germany

² ZWE FRM-II, Technical University Munich, 85747 Garching, Germany

³ Institut Laue-Langevin, F-38042 Grenoble, France

⁴ Northwest Institute of Nuclear Technology, Beijing, P. R. China

Introduction

Due to the very parallel beam collimation at the neutron radiography facility ANTARES, the distance between sample and detector can be increased to 0.5–2 m distance while still obtaining unblurred images. At these large distances, small angle scattering effects in otherwise homogenous and plane samples build up to intensity variations that can be detected in a radiography image. We have examined different aluminium and steel samples with texture variations induced by plastic deformation.

Motivation

Quantitative stress measurements are performed with the Stress-Spectrometer STRESS-SPEC, where crystal lattice reflexes can be examined to a depth of several centimeters. By using small diaphragms, the incoming and outgoing neutron beam is focused to a measuring volume of about one cubic millimeter. By scanning the sample volume, the internal stress is mapped due to shift of the reflexes compared to the unperturbed material. Scanning of a large volume may take hours up to days. With neutron radiography and tomography, it is intended to do a qualitative scan of the sample as a whole and to determine regions of interest to be scanned quantitatively by STRESS-SPEC.

Working principle

The beam at ANTARES has a very high parallel collimation ratio of $L/D = 800$. With the use of a selector wheel with pinhole apertures, this collimation can be increased to values between 2300 and 16000. Small texture changes in an otherwise flat and homogeneous sample will lead to locally increased small angle scattering, deviating neutrons from their straight path. The effect is not visible in standard radiography with the sample close to the detector. If the sample–detector distance is increased to 0.5–2 m, even faint effects become visible in a radiography or tomography.

Radiographic examination of smooth-polished car chassis numbers in steel plates

The German Federal Police brought us test samples of steel plates which had contained car chassis numbers hammered into the metal. Fig. 1 (left) shows a photo of the steel plates with a size of about 5 cm. The plates were sanded to a smooth surface, no trace of the chassis numbers is visible by eye. Fig. 1 (right) shows a standard neutron radiography with a few centimeters distance to the detector, revealing nothing but homogeneous material. The distance was then increased to two meters, the collimation ratio to 2300. Fig. 2 shows enhanced images of the plates with most of the original imprinted numbers visible.

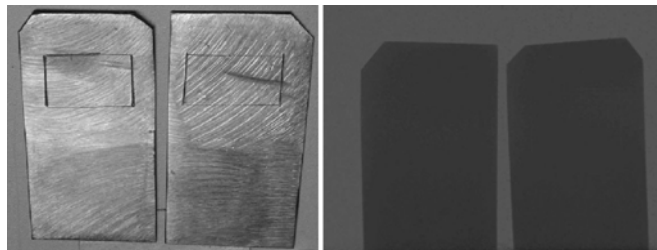


Figure 1: Photo of the sanded steel plates (left); standard neutron radiography (right).

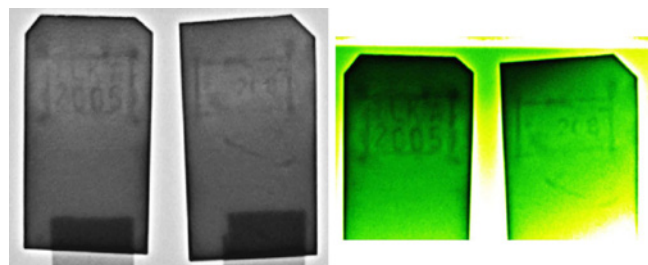


Figure 2: Large distance radiography (left); false colours of the radiography image (right).

Tomographic examination of a cold-expanded rivet hole in Aluminium

Aircraft parts are riveted, not welded together. The rivet holes are subjected to high stress during operation. To increase their stability, holes are drilled to less than the required diameter, then cold expanded by about 4% by a mandrel. This process introduces plastic deformation and a negative pre-stress into the hole edges. If pulling forces are introduced by the rivets during aircraft operation, the negative stress is first compensated before positive stress may lead to cracks. As a test sample, we examined a rolled-out Aluminium sheet with a cold expanded hole with neutron computed tomography. The sample was put in a distance of half a meter to the detector. The computed tomography returns a certain range of attenuation values or grey values for the material Aluminium. For three-dimensional visualisation, we set most of that greyvalue range to transparent and examined only the most attenuating upper greyvalue range. Fig. 3 show a standard view of the Aluminium sheet, Fig. 4 shows the same sheet with only the most attenuating parts set visible.

The tomography first reveals a wave structure originating from the rolling-out of the metal sheet. Furthermore, the edge of the cold-expanded hole shows a significant increase in attenuation compared to the surrounding material (Fig. 5). The Fig. 6, 7 and 8 show better that it is a true 3D tomography. Ordinary holes in the same samples were drilled later and re-examined. They did not show the increased attenuation at the edge.

This measurement was performed at a time when the above-mentioned pinhole selector wheel had not been available. The experiment will be repeated with even higher collimation soon.

Conclusion

A very high collimation of the neutron radiography beam allows for the examination of small angle scattering effects in neutron radiography and tomography and thus extends the range of examination methods considerably. More experiments will be done soon.

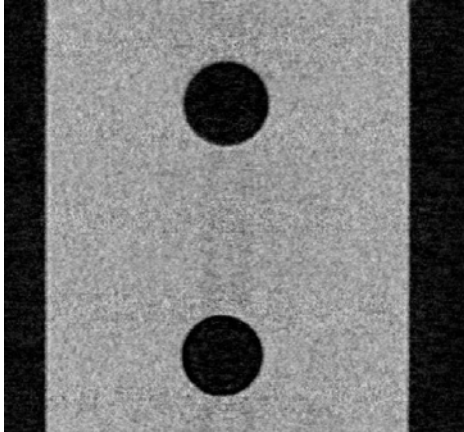


Figure 3: Standard tomographic view of the Aluminium sheet.

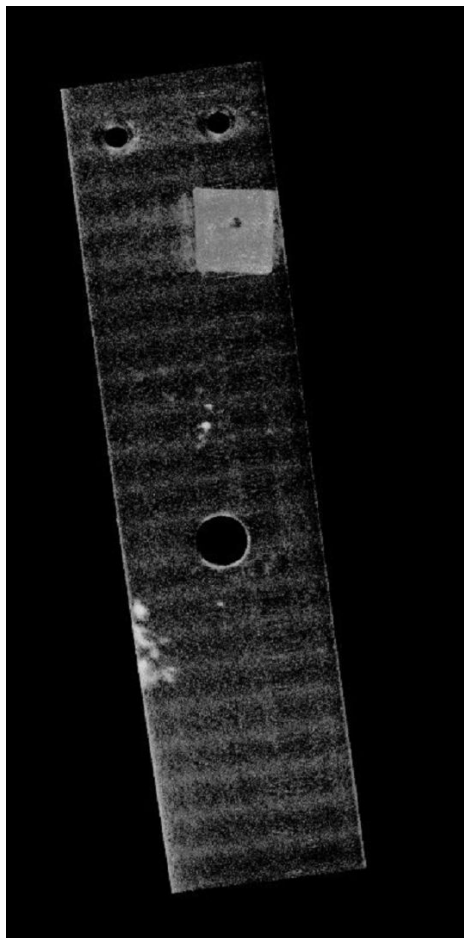


Figure 4: Only the most attenuating areas visible.

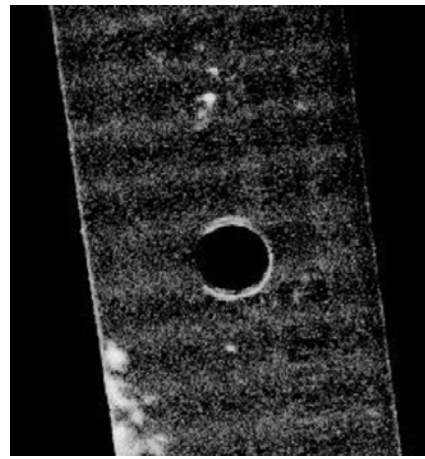


Figure 5: Increased attenuation at the hole edges.

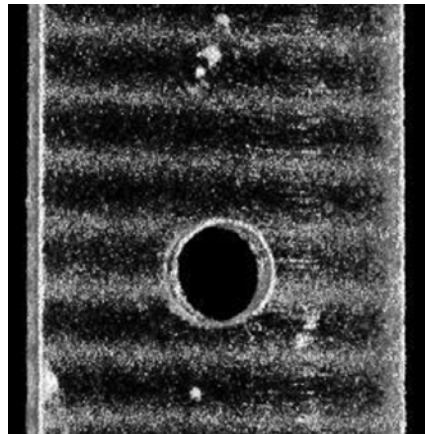


Figure 6: This image proves that it is a true 3D tomography.

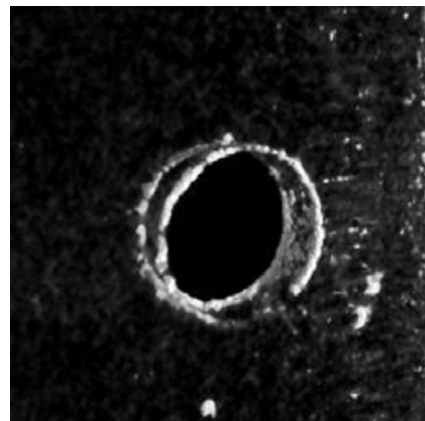


Figure 7: Another 3D view with the wave structure invisible.

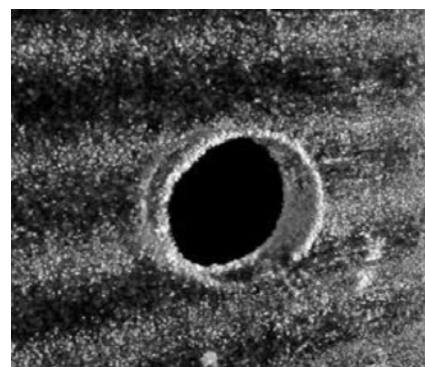
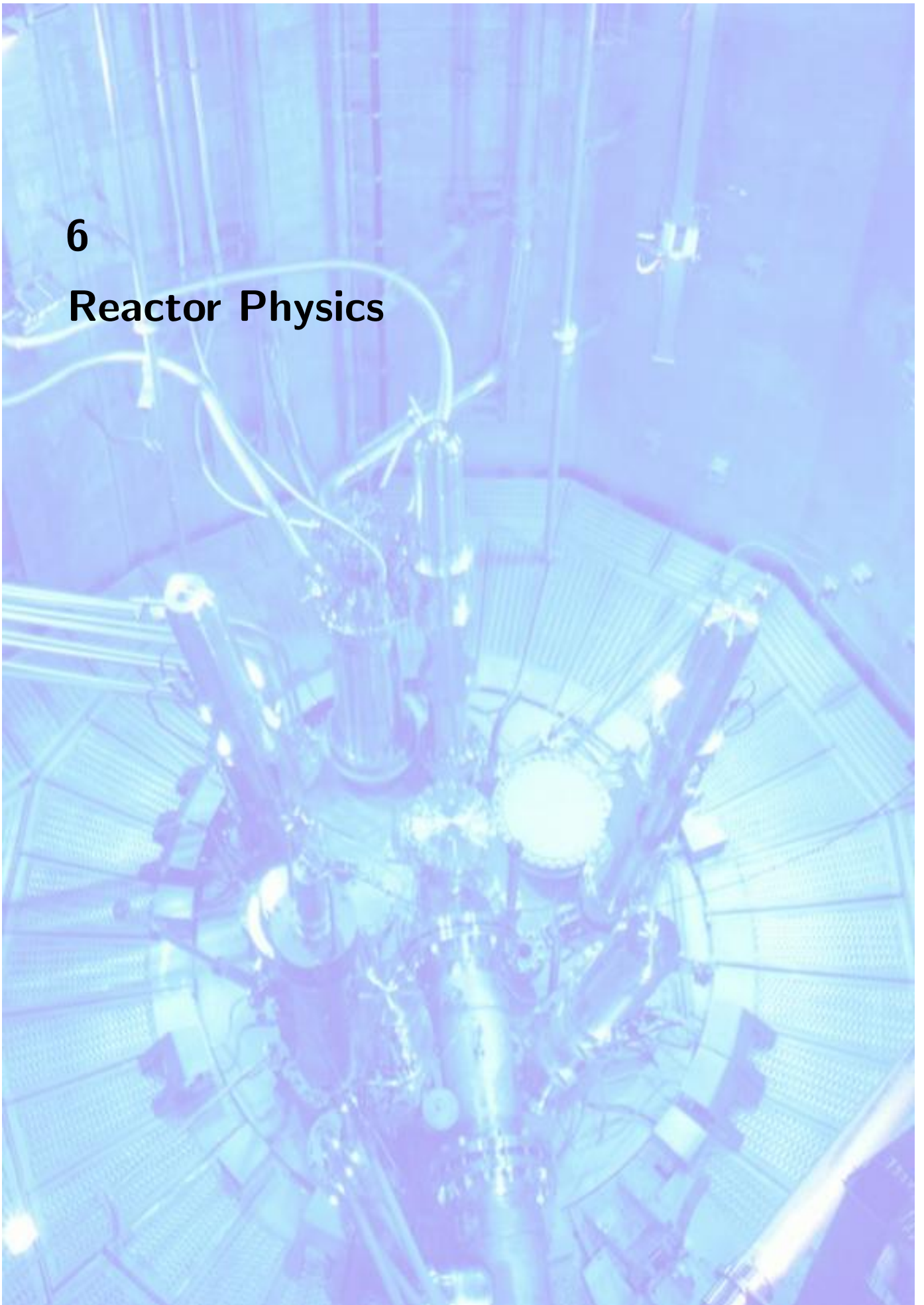


Figure 8: All hard structures together.

6

Reactor Physics



6.1 Heavy Ion Irradiation of U-Mo/Al Dispersion fuel

N. Wieschalla^{1, 2}, A. Bergmaier³, P. Böni¹, K. Böning^{1, 2}, W. Petry², A. Röhrmoser²

¹ Physics Department E21, Technical University Munich, 85747 Garching, Germany

² ZWE FRM-II, Technical University Munich, 85747 Garching, Germany

³ Institut für Angewandte Physik und Messtechnik LRT2, Werner-Heisenberg-Weg 39, D-85577 Neubiberg, Germany

Introduction

The international community has decided to use - whenever possible - Low Enriched Uranium (LEU) instead of High Enriched Uranium (HEU) fuel for research and test reactors. In order to achieve this goal high density fuels are required. One of the most promising candidates is the metallic U-Mo/Al dispersion fuel. This fuel allows a uranium density of around 8.5 gU/cm³ and is currently under worldwide development [1].

However, some concerns have appeared due to the anomalous swelling of full size plates during in-pile irradiation. Post irradiation examinations of these plates revealed an Al-rich interdiffusion layer building up at the interface between U-Mo grains and the Al-Matrix with a thickness of some 10 μ m. Furthermore, cracks which are regarded as the reason of the anomalous swelling have been observed between the interdiffusion layer and the matrix [2].

Here we show an approach to generate an interdiffusion layer by out-of-pile irradiations with heavy ions thereby simulating the radiation damage created by fission fragments during reactor irradiation without the drawback of creating highly radioactive samples.

Experimental set-up

Fuel plates containing spherical U-6wt% Mo and U-10wt% Mo dispersed in Al were provided by Argonne National Laboratory free of charge. The samples were cut (5 \times 5 mm²) and polished in order to make the meat layer accessible for irradiation with heavy ions. The irradiation-experiment has been carried out at the Munich 14 MV tandem accelerator in Garching near Munich, Germany with a heavy ion beam of I-127 at 120 MeV. The penetration depth depends on the target material, but is always in the range of the thickness of the interdiffusion layer (see Fig. 1). The flux was set in order to not exceed a sample temperature of 200 °C. The final fluence was 10¹⁷ ions/cm², which corresponds to a low burn-up.

Post Irradiation Examinations

Fig. 2 (right hand side - optical microscopy) shows a partly heavy ion-irradiated U-Mo sample. The part on the left hand side was not irradiated and therefore looks like fresh fuel, while the part on the right hand side has been irradiated. Here a new phase between the fuel and the matrix is visible. This new phase has sharp borders and a light blue colour. The blue colour could be due to the irradiation with iodine. The thickness of the new phase depends on many parameters but is always in the range of some 10 μ m. These optical properties fit with the interdiffusion layer, which has been observed after in-pile irradiation.

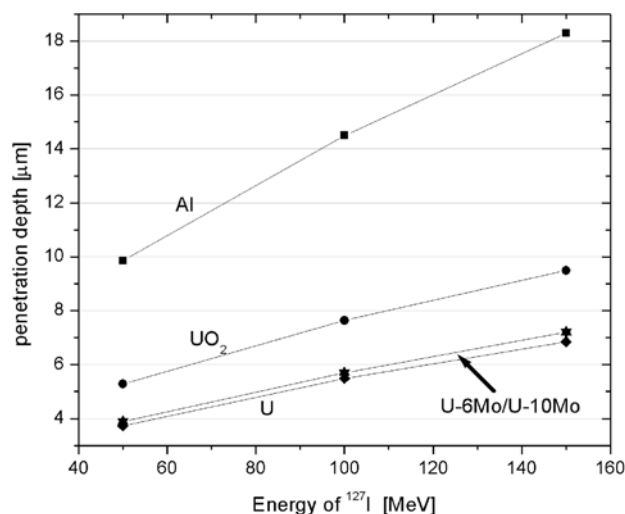


Figure 1: Penetration depth of Iodine-127 into different materials [3].

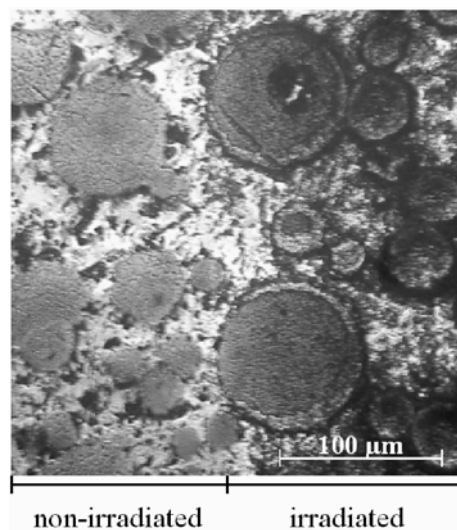


Figure 2: Optical microscopy of a partly irradiated U-6Mo sample.

Furthermore, we accomplished to file a patent (reference no. DE 10 2005 055 692) in 2005, which is dealing with a manufacturing technique for U-Mo monolithic.

References

- [1] J.L. Snelgrove, G. L. Hofman, C. L. Trybus, and T. C. Wiencek. Development of very-high-density fuels by the RERTR Program. 19th RERTR - Reduced Enrichment for Research and Test Reactors, 1996.
- [2] P. Lemoine, J. L. Snelgrove, N. Arkhangelsky, and L. Alvarez. UMo Dispersion fuel results and status of qualification programs. 8th RRFM - International Topical Meeting on Research Reactor Fuel Management, 2004.
- [3] J. F. Ziegler and J. P. Biersack. SRIM - the stopping and range of ions in matter. version srim-2003.26, computer code, 2003.

7

Instrument Development



7.1 MuPAD - Spherical Neutron Polarimetry at SINQ and FRM-II

S. Klimko^{1, 2, 3}, M. Janoschek^{1, 3}, B. Roessli³, R. Gähler⁴, P. Böni¹

¹Physics Department E21, Technical University Munich, 85747 Garching, Germany

²DRFMC, CEA-Grenoble, SPSMS-MDN, 17 rue des Martyrs, 38054 Grenoble, Cedex 9, France

³Laboratory for Neutron Scattering ETHZ & Paul Scherrer Institut, CH-5232 Villigen PSI, Switzerland

⁴Institute Laue Langevin, 6, rue Jules Horowitz, B.P.156, 38042 Grenoble, Cedex 9, France

Introduction

In 1963, Blume [1] derived the change of neutron polarization upon elastic scattering. The Blume equations show that neutron polarization transforms as a vector during an elastic scattering process with any given sample. Maleyev proved that the Blume equations also hold for the inelastic case when correlation functions depending on neutron energy transfer are introduced [2]. The Blume-Maleyev equations are then

$$\sigma = \frac{d^2\sigma}{d\Omega dE'} = \sigma_N + M^y + M^z - P_0^x C + P_0^y R^y + P_0^z R^z \quad (1)$$

for the polarization dependent partial differential cross-section and

$$\begin{aligned} \mathbf{P}' &= \tilde{\mathbf{P}}\mathbf{P}_0 + \mathbf{P}'' , \\ \sigma\tilde{\mathbf{P}} &= \begin{pmatrix} (\sigma_N - M^y - M^z) & iI^z & -iI^y \\ -iI^z & (\sigma_N + M^y - M^z) & M_{mix} \\ iI^y & M_{mix} & (\sigma_N - M^y + M^z) \end{pmatrix} , \\ \sigma\mathbf{P}'' &= \begin{pmatrix} C \\ R^y \\ R^z \end{pmatrix} , \end{aligned} \quad (2)$$

for the final polarization vector. $\tilde{\mathbf{P}}$ is the polarization tensor which describes the rotation of the initial polarization vector in the scattering process and \mathbf{P}'' is the polarization created in the scattering process at the sample. All the terms included in Eq. 1 and 2 are only determined by the sample properties which are described by the nuclear structure factor $N_{\mathbf{Q}}$ and the magnetic interaction vector $\mathbf{M}_{\perp\mathbf{Q}}$. They are summarized in Tab. 1. Usually the set of polarization axis is defined to have x parallel to the scattering vector \mathbf{Q} , z perpendicular to the scattering plane and y completing the right-handed set.

The measured quantity is the polarization matrix, namely the final polarization vector after the scattering process for all three directions of the incident beam polarization,

$$P_{ij} = (P_i\tilde{P}_{ji} + P_j'')/|\mathbf{P}_0|, \quad (3)$$

where i and j ($i, j = x, y, z$) denote the directions of the incident and final polarization vector, respectively. Such a *polarization analysis* experiment gives a lot of additional information compared to just measuring the neutron scattering

cross-section in Eq. 1. The additional data can be used to disentangle the different contributions to the scattering cross-section for each point in (\mathbf{Q}, ω) -space. In an unpolarized neutron scattering experiment all the different contributions are superposed.

Scientific scope

Over the last decade systematic polarization analysis has been used to cope with scientific questions which were intractable before. Some of them are:

- study of magneto-electric crystals such as LiCoPO_4 and MnGeO_3 [3]. These compounds characteristically rotate the polarization vector. Measuring this rotation enables to identify the relative population of the magneto-electric domains and to determine the antiferromagnetic structure factors in these compounds and hence the magnetisation distribution leading to magneto-electricity.
- study of non-collinear magnetic structures. For such compounds it is often impossible to distinguish certain possible magnetic structures by other techniques because they are not able to determine the directional information held in magnetic structure factors. One example is UPtGe [4].
- investigation of hybrid correlation functions in inelastic neutron scattering in compounds where nuclear and magnetic degrees of freedom or different magnetic degrees of freedom interfere [5].

Experimental approaches

Classical longitudinal polarization analysis [6] copes with the risk of depolarization due to residual magnetic fields by application of a magnetic guide field along the polarized neutron beam. However, this setup only allows the projection of the final polarization vector onto the direction of the guide field to be determined. Any component of the polarization turned into a direction perpendicular to the guide field upon the scattering process will be depolarized. Hence only the

σ_N	$\frac{k'}{k} \langle N_{\mathbf{Q}} N_{\mathbf{Q}}^\dagger \rangle_\omega$	the nuclear contribution
$M^{y/z}$	$r_0^2 \frac{k'}{k} \langle M_{\perp\mathbf{Q}}^{y/z} M_{\perp\mathbf{Q}}^{\dagger y/z} \rangle_\omega$	the y - and z -components of the magnetic contribution. The x -component is missing because of the geometric selection rule!
$R^{y/z}$	$r_0 \frac{k'}{k} \langle N_{\mathbf{Q}}^\dagger M_{\perp\mathbf{Q}}^{y/z} \rangle_\omega + \langle M_{\perp\mathbf{Q}}^{\dagger y/z} N_{\mathbf{Q}} \rangle_\omega$	real parts of the nuclear-magnetic interference term.
$I^{y/z}$	$r_0 \frac{k'}{k} \langle N_{\mathbf{Q}}^\dagger M_{\perp\mathbf{Q}}^{y/z} \rangle_\omega - \langle M_{\perp\mathbf{Q}}^{\dagger y/z} N_{\mathbf{Q}} \rangle_\omega$	imaginary parts of the nuclear-magnetic interference term.
C	$ir_0^2 \frac{k'}{k} (\langle M_{\perp\mathbf{Q}}^y M_{\perp\mathbf{Q}}^{\dagger z} \rangle_\omega - \langle M_{\perp\mathbf{Q}}^z M_{\perp\mathbf{Q}}^{\dagger y} \rangle_\omega)$	chiral contribution
M_{mix}	$r_0^2 \frac{k'}{k} (\langle M_{\perp\mathbf{Q}}^y M_{\perp\mathbf{Q}}^{\dagger z} \rangle_\omega + \langle M_{\perp\mathbf{Q}}^z M_{\perp\mathbf{Q}}^{\dagger y} \rangle_\omega)$	mixed magnetic contribution or magnetic-magnetic interference term

Table 1: Terms contained in the Eq. 1,2; $\langle \hat{A}_{\mathbf{Q}} \hat{B}_{\mathbf{Q}}^\dagger \rangle_\omega$ are inelastic correlation functions; \mathbf{Q} is the scattering vector and $\hbar\omega$ the energy transfer; x, y, z denote the three directions in space, where $x \parallel \mathbf{Q}$, $y \perp \mathbf{Q}$ in scattering plane and $z \perp \mathbf{Q}$ out of scattering plane.

three diagonal terms of the polarization matrix may be determined. But to handle the scientific cases presented above the information of the six off-diagonal terms is needed.

Alternatively the neutron polarization can be conserved when any residual fields are removed from the sample environment by a zero field chamber. Then any component of the final polarization vector may be determined and the full polarization matrix can be measured. This method is known as *Spherical Neutron Polarimetry* (SNP). Until now CryoPAD (Cryogenic Polarization Analysis Device), presented by Tasset et al. [7] in 1989, was the only device to perform routine SNP measurements at finite scattering angles. It is based on a zero field chamber, realized through a double superconducting Meissner-shield.

However, in June 2004 we proved successfully with a prototype of MuPAD (Mu-Metal Polarization Analysis Device) that an alternative setup based on a zero-field chamber made of highly permeable mu-metal is also feasible [8]. Advantages of MuPAD over CryoPAD are that it is more cost-efficient and easier to operate as it is a non-cryogenic device.

MuPAD

After the successful test we decided to proceed with development of MuPAD in order to be able to perform full SNP measurements at the research reactor FRM-II in Munich. Additionally a cooperation with the Laboratory for Neutron Scattering at the Paul Scherrer Institute (PSI) in Switzerland with the aim to construct a full featured MuPAD SNP device which is easily to setup on different spectrometers at the two neutron sources was started. One of these devices should be built for each neutron source.

The R & D phase for the new MuPAD was finished in May 2005. The most important features are:

- double mu-metal zero field chamber, magnetic shielding factor of $S = 1000 - 3000$ depending on direction.
- beam size: $60 \times 30 \text{ mm}^2$.
- sample space: $\varnothing = 356 \text{ mm}$ (enables to host standard ILL orange cryostat and FRM-II closed cycle cryostat).
- high quality precession coils with perfectly homogenous inner field to manipulate initial and final polarization vectors. Neutron beam does not intersect with outer stray field of the coils. Polarization vector is turned precisely for a range of wavelengths $0.8 < \lambda < 8 \text{ \AA}$. They are shown in Fig. 1.
- *MuPAD one unit system*: the MuPAD device consists of one single completely assembled unit. This guarantees simple and reproducible installation on different neutron scattering instruments.
- pneumatic mu-metall lamella system which automatically fully closes the zero field chamber independent of scattering angle.

A technical drawing of the whole device is shown in Fig. 2. The device for the PSI was assembled first and is now fully operational. It was successfully tested in September 2005 (s. article 'MuPAD - First tests and results' for more details).

The second MuPAD for the FRM-II is being assembled now and will be tested and installed on MIRA in February 2006.

Additionally the MuPAD concept allows that it can be installed easily on different spectrometers. Possible candidates are the hot single crystal diffractometer HEIDI and the three-axis-spectrometer PANDA for cold neutrons at the FRM-II.

Conclusion

The full feature SNP device MuPAD has been planned, built and tested within one year and showed good performance within the tests. MuPAD will mostly be used to disentangle magnetic and lattice degrees of freedom in modern magnetic materials, e.g. ferroics and non-collinear antiferromagnets.

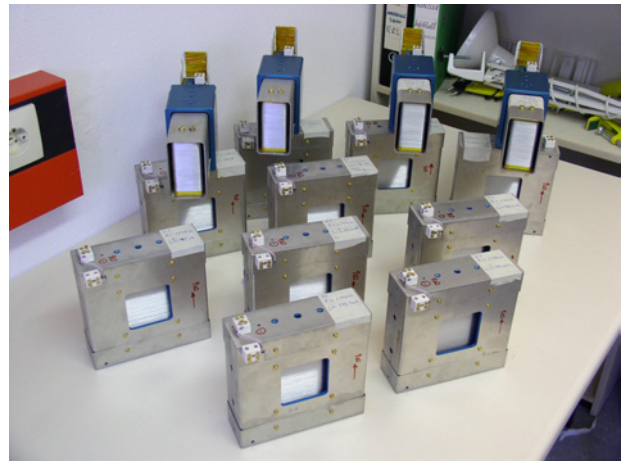


Figure 1: Coils for the two MuPADs at SINQ and FRM-II.

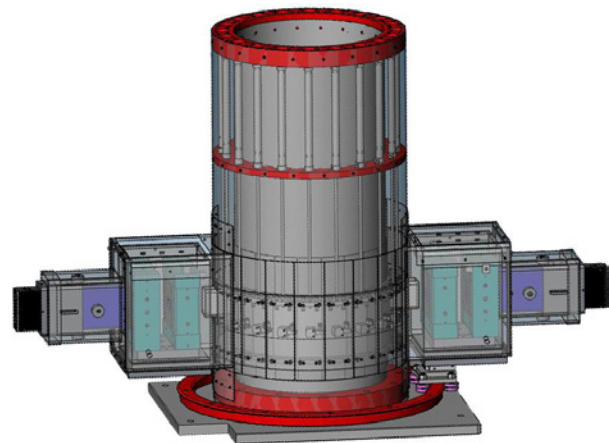


Figure 2: Technical drawing of MuPAD.

References

- [1] M. Blume. *Phys.Rev.*, 130:1670–1676, 1963.
- [2] S. V. Maleyev. *Physica B*, 267-268:236–242, 1999.
- [3] P. J. Brown, J. B. Forsyth, and F. Tasset. *Solid State Sciences*, 7:682–689, 2005.
- [4] D. Mannix, S. Coad, G. H. Lander, J. Rebizant, P. J. Brown, J. A. Paixão, S. Landgridge, S. Kawamata, and Y. Yamaguchi. *Phys. Rev. B.*, 62(6):3801–3810, 2000.
- [5] L.P. Regnault, C. Boullier H.M. Rønnow and, J.E. Lorenzo, and C. Marin. *Physica B*, 345:111–118, 2004.
- [6] R. M. Moon, T. Riste, and W.C. Koehler. *Phys. Rev.*, 181(920), 1969.
- [7] F. Tasset. *Physica B*, 156-157:627, 1989.
- [8] M. Janoschek. Master's thesis, Technical University Munich, <http://mupad.wired-things.de>, 2004.

7.2 Spherical neutron polarimetry data analysis with FullProf: soon a reality

M. Janoschek^{1, 2}, M. Medarde^{3, 2}, J. Rodriguez-Carvajal⁴

¹Physics Department E21, Technical University Munich, 85747 Garching, Germany

²Laboratory for Neutron Scattering ETHZ & Paul Scherrer Institut, CH-5232 Villigen PSI, Switzerland

³Laboratory for Developments and Methods, Paul Scherrer Institut, 5232 Villigen PSI, Switzerland

⁴Laboratoire Leon Brillouin (CEA-CNRS), CEA/Saclay, 91191 Gif sur Yvette Cedex, France

The technique of *Spherical Neutron Polarimetry* (SNP) is recently becoming more and more popular. As there are already three CryoPAD devices (two at the ILL, France and one at JAERI, Japan) and one MuPAD (PSI, Switzerland) already in operation and another being assembled at the moment for the FRM-II the demand for software being capable of analyzing SNP data sets will increase.

At present there is only one library which is enabled to treat such kind of data, namely the *Cambridge Crystallographic Subroutines Library* (CCSL) [1]. However, CCSL rather represents a framework of Fortran77 subroutines which may be used to compile programs to analyze data than a program which allows a user to easily process his data. Other pieces of software are user-made programs (in Igor, Mathematica), but are only made for particular cases.

Evidently nonspecialist users will need a user-friendly software to treat their SNP data. FullProf [2] is a program for fitting and analyzing neutron powder and single crystal data with the Rietveld method [3]. FullProf has a comfortable graphical user interface and is widely known in the neutron scattering community. One of its major advantages is that it is build on the *Crystallographic Fortran Module Library* (CrysFML) [4] written in the modern object-oriented Fortran95 and therefore is easy to extend. FullProf is already able to calculate all information necessary to obtain the polarization matrix measured by SNP devices for any given sample, namely the nuclear structure factor $N_{\mathbf{Q}}$ and the magnetic interaction vector $\mathbf{M}_{\perp\mathbf{Q}}$ (s. also article about MuPAD).

Therefore we extended CrysFML with an SNP module enabled to process the polarization matrix out of $N_{\mathbf{Q}}$ and $\mathbf{M}_{\perp\mathbf{Q}}$ by applying the Blume-Maleyev-equations [5, 6]. We wrote the small text based program PolarCalc which uses this SNP module and thus is able to simulate the polarization matrix at a single point in (\mathbf{Q}, ω) -space for any given sample. The information about the nuclear and magnetic structure of the sample is given in the form of a *.cfl input file. An example for such a file is shown in Fig. 1. Fig. 2 shows the output of PolarCalc at a single point in reciprocal space. PolarCalc is very helpful to decide on which points in reciprocal space one will be able to distinguish between two possible magnetic structures for a given sample before conducting an SNP measurement.

The next step will be to include this module into the fit-routines of FullProf to be able to fit magnetic structures with the help of the additional information obtained by SNP measurements. This part of CrysFML will be realized in the near future.

References

- [1] J. C. Matthewman, P. Thompson, and P. J. Brown. *Jour. of Appl. Crystallogr.*, 15(2):167–173, 1982.
- [2] J. Rodriguez-Carvajal. *Physica B*, 192:55, 1993.
- [3] H. M. Rietveld. *J. Appl. Crystallogr.*, 2:65, 1969.
- [4] J. Rodriguez-Carvajal and J. González-Platas. *Acta Cryst. A*, 58(C87), 2002.
- [5] M. Blume. *Phys.Rev.*, 130:1670–1676, 1963.
- [6] S. V. Maleyev. *Physica B*, 267-268:236–242, 1999.

```

TITLE MnSi (Symmetry op. of Gk)
SPGR P 21 3
CELL 4.558 4.558 4.558 90.000000 90.000000 90.000000
! Lab Scatt x y z Biso Occ
ATOM MN MN 0.13800 0.13800 0.13800 0.00000 0.33333
ATOM SI SI 0.84500 0.84500 0.84500 0.00000 0.33333

Mag_Structure
!
lattice P
!these are only the k-vectors in the plane defined by 100 011!
kvect 0.01700 0.01700 0.01700
kvect -0.01700 -0.01700 -0.01700
kvect 0.01700 -0.01700 -0.01700
kvect -0.01700 0.01700 0.01700

magcent
!symmetry operation reproducing all four MN atoms for the magnetic calculations
symm x,x,x
msym u,v,w,0.0
symm -x+0.5,-x,x+0.5
msym u,v,w,0.0
symm -x,x+0.5,-x+0.5
msym u,v,w,0.0
symm x+0.5,-x+0.5,-x
msym u,v,w,0.0

matom MN1 MMN3 0.13800 0.13800 0.13800 0.00000 1.00000
skp 1 1 -0.1633 0.08160 0.08160 0.00000 0.14140 -0.14140 0.00000
skp 2 1 -0.1633 0.08160 0.08160 0.00000 -0.14140 0.14140 0.00000
skp 3 1 -0.1633 -0.08160 -0.08160 0.00000 0.14140 -0.14140 0.00000
skp 4 1 -0.1633 -0.08160 -0.08160 0.00000 -0.14140 0.14140 0.00000
!
End_Mag_Structure

```

Figure 1: mnsi.cfl - input file for the magnetic compound MnSi for the program PolarCalc.

```

Polar information:
-----
=> initial parameters:

Qh = 1.0170 Qk = 1.0170 Ql = 1.0170
SPV = (0.000, 0.000, 1.000)
P = 1.000

=> interaction potentials:

NSF = 0.000000 + i 0.000000
MIV = (0.000000 + i 0.000000, -0.029805 - i 0.073417, -0.073416 + i 0.029801)
MSF = 0.000000

=> different contributions to the cross-section:

Nuclear Contribution = 0.000000
magnetic along y = 0.006278
magnetic along z = 0.006278
real nuclear magnetic al. y = 0.000000
real nuclear magnetic al. z = 0.000000
imag nuclear magnetic al. y = 0.000000
imag nuclear magnetic al. z = 0.000000
chiral contribution = -0.012557
magnetic magnetic = 0.000001

=> cross-section for initial polar vector:

along x = 0.025113
along y = 0.012557
along z = 0.012557

=> polarization tensor as it will be measured:

PT =
| -1.000 -1.000 -1.000 |
| 0.000 0.000 0.000 |
| 0.000 0.000 0.000 |

```

Figure 2: Output of the program PolarCalc for the compound MnSi on the magnetic satellite at (1.017, 10.17 1.017).

7.3 MuPAD - First tests and results

M. Janoschek^{1, 2}, S. Klimko⁴, B. Roessli², M. Medarde^{3, 2}, P. Böni¹

¹ Physics Department E21, Technical University Munich, 85747 Garching, Germany

² Laboratory for Neutron Scattering ETHZ & Paul Scherrer Institut, CH-5232 Villigen PSI, Switzerland

³ Laboratory for Developments and Methods, Paul Scherrer Institut, 5232 Villigen PSI, Switzerland

⁴ Département de Recherche Fondamentale sur la Matière Condensée, CEA-Grenoble, SPSMS-MDN, 17 rue des Martyrs, 38054 Grenoble, Cedex 9, France

Introduction

The construction of the first full featured version of MuPAD for the continuous neutron spallation source SINQ at the Paul Scherrer Institute in Switzerland was finished in early September of this year. Therefore several tests with and without neutrons were performed. In September and October of this year MuPAD was tested during 4 weeks mounted on the cold three axis spectrometer TASP at PSI (s. Fig. 2).

MuPAD precession coils and zero-field chamber

Before the experiments on TASP were done the properties of MuPAD's precision coils and zero-field chamber were measured accurately and compared to the prototype version built in 2004 [1]. As shown in Fig. 1 and Tab. 1 the residual fields of the coils were improved significantly. The shielding factor $S = \frac{B_0}{B_i}$ (B_0 outer field, B_i field in chamber) of the zero-field chamber is between 1000-3000 throughout the whole chamber. Therefore all areas with high stray fields in the prototype were systematically removed for the new version.

Measurements on TASP

The performance of an SNP device may be judged by measuring the polarization matrix (s. article 'MuPAD - Spherical Neutron Polarimetry at SINQ and FRM-II') on a nuclear Bragg. There, the polarization vector remains unchanged when the neutron beam is diffracted. Hence all the off-diagonal terms should be zero. During the test measurements on TASP we determined the polarization matrix on the Bragg peak (0 0 -4) of $\text{HoNi}_2^{11}\text{B}_2\text{C}$:

$$P = \begin{pmatrix} 0.87(3) & 0.02(5) & 0.00(5) \\ -0.06(5) & 0.85(3) & 0.09(5) \\ 0.06(5) & 0.04(5) & 0.87(3) \end{pmatrix} \quad (1)$$

As the off-diagonal elements are zero within the errorbars, this shows that MuPAD can be operated with good performance. The diagonal elements are reduced from one due to the finite incident polarization of the neutron beam.

	L_x	ϕ_x	L_y	ϕ_y	L_z	ϕ_z
	[mGmm]	[°]	[mGmm]	[°]	[mGmm]	[°]
old PCs	1519.7	0.62	185.3	0.08	224.9	0.09
new PCs	120.7	0.05	25.5	0.01	119.8	0.05

Table 1: Field integrals L_i of the residual fields for old and new MuPAD precession coils for an inner field integral of 20 Gcm corresponding to a $\pi/2$ -flip for 4.1 \AA^{-1} neutrons. ϕ denotes the rotation of the polarization for the same neutrons due to the residual fields.

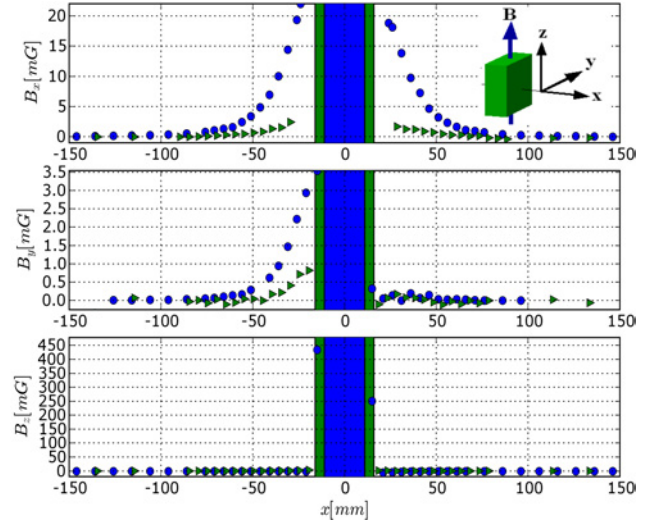


Figure 1: Comparison of residual fields of the prototype precession coils (blue) and coils for the new MuPAD (green). The shaded area represents the region of the inner field of the coils. The inset in the upper right corner shows the used coordinate frame. The size of the new coils (green) is slightly larger. The residual fields of the new coils are significantly lower (s. also Tab. 1).



Figure 2: MuPAD mounted on TASP at PSI.

References

- [1] M. Janoschek. Master's thesis, Technical University Munich, <http://mupad.wired-things.de>, 2004.

7.4 First Measurements with an Elliptically Shaped Neutron Guide

M. Stadlbauer¹, P. Böni¹, S. Mühlbauer¹, C. Schanzer², J. Stahn², U. Filges²

¹ Physics Department E21, Technical University Munich, 85747 Garching, Germany

² Paul Scherrer Institute, CH-5232 Villigen, Switzerland

First simulations with McStas showed a superior behaviour of elliptically shaped neutron guides concerning intensity gain, focal diameter and phase space homogeneity [1]. For this reason a prototype of an elliptically tapered guide was produced and measured. The length of the guide was chosen to be 2 m what also allows a much easier handling of the structure. Due to manufacturing reasons, the guide consists of four segments of each 0.5 m. The focal points of the guide are situated 80 mm from the ends of the guide as defined by the shape of the ellipse. The detailed information is given in Tab. 1.

Cross-section at entrance	$4 \times 8 \text{ mm}^2$
Cross-section at exit	$4 \times 8 \text{ mm}^2$
Largest cross-section	$10.6 \times 21.2 \text{ mm}^2$
Supermirror coating	$m = 3, R = 0.81$
Dist. focal point to guide entrance	80 mm
Distance focal point to guide exit	80 mm

Table 1: Geometrical specifications of the elliptic guide

Experiments

The focusing properties of this guide were tested at the beam line MORPHEUS at the Swiss Spallation Source SINQ. The four individual guide segments were visually aligned by means of frames. In order to define a pointlike source in the focal plane at the entrance of the guide a cadmium aperture with a 2 mm pinhole was used. This pinhole was illuminated with neutrons of 4.743 Å. A two dimensional neutron sensitive imageplate with a resolution of 50 μm was placed at 13 different positions between 5 and 160 mm from the guide exit to detect the neutron distribution. Fig. 1 was recorded in the focal plane of the guide. It can be clearly seen that the neutron beam is extremely well focused onto a spot with a diameter of approximately 0.8 mm (FWHM) whereas the misalignment causes a crosslike structure and a shoulder peak on the left side of the focal point. In Fig. 2 the dependence of the neutron intensity integrated over an area of $0.5 \times 0.5 \text{ mm}^2$ at the center of the beam is plotted versus the distance from the guide exit. Obviously the measured focal plane coincides with the expected one at $F \approx 80 \text{ mm}$. Furthermore, it can be clearly seen that flux gains of the order of 25 can be realized between the exit and the focal point.

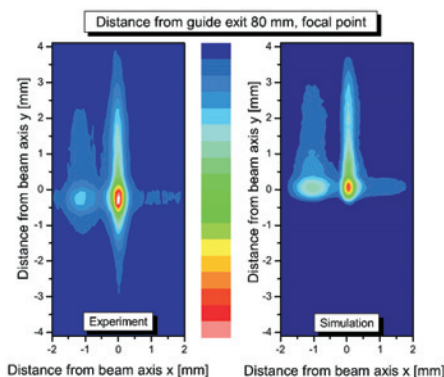


Figure 1: Neutron distribution in the focal plane [2].

Simulations

To reproduce these intensity distributions theoretically the Monte-Carlo program McStas was used with the component file *Guide tapering.comp* that we developed in 2003. This allows for simulating doubly focusing guides with elliptic [1], parabolic [3, 4] or even more general tapering with the option “ownfunction”. Taking the geometrical specifications of the guide into account several configurations of misalignment of the guide segments were investigated. Mainly the third and fourth segment of the guide turned out to be responsible for the measured neutron intensity distributions. We succeeded to reproduce the measured intensity distributions almost perfectly (Fig. 1) by tilting the third segment in the vertical and horizontal direction by 0.03° and -0.05° and the fourth segment by 0.01° and 0.05° , respectively. Also the intensity gain depending on the distance from the guide exit can be reproduced very well (Fig. 2).

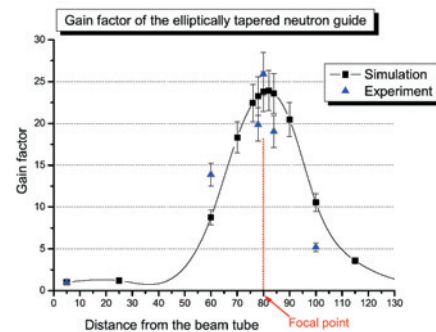


Figure 2: Neutron intensity as measured and calculated vs. distance from exit.

Conclusion

The proposed superior behaviour of an elliptically tapered neutron guide was shown, by performing first measurements on this type of guide. Furthermore, the nonsymmetric neutron distribution at several positions behind the guide exit due to misalignment during the measurements could be reproduced very nicely by using McStas and taking adequate types of misalignment into account.

Acknowledgments

We would like to thank E. Lehmann from PSI for providing the image plate and for helping to analyze the data. This work was supported by the European Union within the Sixth Framework Program FP6 under contract no. 505925.

References

- [1] C. Schanzer, P. Böni, U. Filges, and T. Hils. *Nucl. Instr. Meth. A*, 529:63–68, 2004.
- [2] S. Mühlbauer, M. Stadlbauer, P. Böni, C. Schanzer, J. Stahn, and U. Filges. Performance of an elliptically tapered neutron guide. *EL-sevier Science*, accepted for publication.
- [3] T. Hils and et al. *Physica B*, 350:166, 2004.
- [4] N. Kardjilov and et al. *Nucl. Instr. Meth. A*, 542:248, 2005.

7.5 Simulations for a new neutron guide switch for the instrument MIRA

Sebastian Mühlbauer¹, Robert Georgii², Peter Böni¹

¹ Technische Universität München, Physics Department E21, D-85747 Garching, Germany

² ZWE FRM-II, Technische Universität München, D-85747 Garching, Germany

The instrument MIRA is located at the end of neutron guide NL6B, which is connected to the cold neutron guide NL6 by means of a wavelength sensitive switch. The neutron flux at the sample position of MIRA was measured recently to be $4 \cdot 10^5 \text{ cm}^{-2} \text{ s}^{-1}$. In order to improve the neutron flux, several simulations for a new, improved neutron guide switch were performed, using the program package McStas [1]. A gain factor of 10 can be reached without the usage of neutron focusing devices. Furthermore, adding neutron focusing devices, gains of 100 compared to the actual flux are achievable. In order to calculate the losses in neutron flux for the NL6 after the rebuilt switch, additional simulations were performed.

Current neutron guide switch

The first issue to be considered is the actual geometry of the guide switch, as shown in Fig. 1. A silicon wafer, tilted at an angle of 3° relative to the beam axis is deflecting the neutrons into the neutron guide NL6B (cross section $120 \times 10 \text{ mm}^2$), which is inclined towards the guide NL6 at an angle of 6° . The silicon wafer reaches 2 cm into the neutron guide NL6 and is coated with Ni^{58} for the first quarter, supermirror $m = 2 [\Theta_c^{Ni}]$ for the second quarter and supermirror $m = 3 [\Theta_c^{Ni}]$ for the second two quarters of its length. The radius of curvature of the guide is 85 m, the supermirror coating is $m = 2 [\Theta_c^{Ni}]$. Both, the inclination of the neutron guide NL6B and the silicon wafer, as well as the radius of curvature of the guide are limiting the cutoff wavelength of the system to 7.7 \AA . The maximum of the cold neutron flux of the FRM-II cold source is located at 4 \AA , therefore only a small fraction of the neutrons can be used at the instrument.

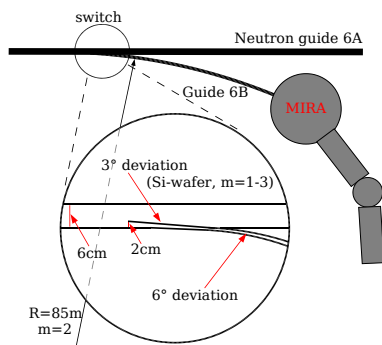


Figure 1: Current geometry of the neutron guide switch for NL6B.

Improved neutron guide switch

Improving the neutron flux without changing the cross section of the neutron guide ($120 \times 10 \text{ mm}^2$) makes it necessary to shift the cutoff wavelength of the guide system to a smaller wavelength, i.e. 4 \AA . To achieve this goal, both the guide and the switch have to be redesigned. The simulations contained several different geometries of varying inclination angles of the neutron guide, different radii of curvature of the guide and different coatings. Within the bounds of geometrical constraints as shown in Fig. 2, the guide switch can be shifted several meters towards the reactor, as well as the instrument

itself can be moved 35 cm towards the NL6. The results of the simulations are presented in Fig. 3.

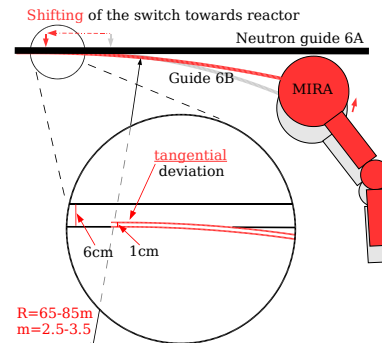


Figure 2: Improved geometry of the neutron guide switch for NL6/B.

Losses for the neutron guide NL6

In order to make assumptions for the losses of flux of the NL6, the neutrons deflected by the switch were subtracted from the flux inside NL6. As only 1 cm of the cross section of NL6 is shadowed, the maximum loss can be $\frac{1}{6}$. Additionally, the divergence of the neutron beam after the switch was analysed.

Results

As shown in Fig. 3, a gain factor in neutron flux of 10 can be reached, shifting the cutoff to shorter wavelengths, while losing only about 12 percent of neutron flux inside the NL6 (shown in the inset of Fig. 3). Furthermore, shorter wavelengths would give direct access to atomic resolution on MIRA, which is not yet possible with 10 \AA .

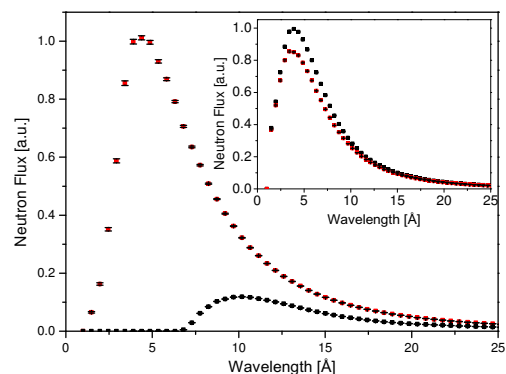


Figure 3: Gain factor for a suggested geometry of the new neutron guide switch (tangential deviation, $R = 80 \text{ m}$, $m = 2.5 [\Theta_c^{Ni}]$, cutoff 4 \AA). The inset shows the losses in the guide NL6 for the upper geometry.

This work was supported by the European Union within the Sixth Framework Program FP6 under contract no. 505925.

References

- [1] K. Nielsen and K. Lefmann. Mcstas, McStas webpage: <http://neutron.risoe.dk/mcstas>. *Physica B*, **283**, 2000.

7.6 First Spin Echo Signal at RESEDA

Wolfgang Häußler^{1, 2}, Dominik Streibl¹, Reinhard Schwikowski², Andreas Mantwill¹,
Heinz Wagensohn², Bodo Gohla-Neudecker², Peter Böni¹

¹Physics Department E21, Technical University Munich, 85747 Garching, Germany

²ZWE FRM-II, Technical University Munich, 85747 Garching, Germany

Despite the technical complexity of the Neutron Resonance Spin Echo Spectrometer (NRSE) RESEDA (Fig. 1), the very meager manpower (one scientist, half-time technician!), and problems caused by non-sufficient shielding at the beam line NOSPEC and the neutron guide, we succeeded to produce the first spin echo signal (Fig. 2) at RESEDA in November 2005.

We improved the radiation shielding of the polarizing part of the neutron guide NL 5b, built an additional shielding around the selector housing, and constructed the shutters for both instruments. A gamma shutter, a beam monitor, and three movable attenuators were constructed and fixed at the end of the neutron guide in front of the spectrometer. High radiation background produced in the first spectrometer arm, however, prevents until now measurements with the full beam.

By using the first neutrons being available at the instrument in August 2005, the primary spectrometer arm of RESEDA was aligned, and first measurements of the shape and intensity of the neutron beam were performed. The estimated intensity of the straight beam, measured by using beam attenuators of well-known attenuation strengths, is in agreement with theoretical predictions. First polarization tests were performed showing that the beam polarization is lower than predicted, most likely due to polarization losses in the Ni/Ti-neutron guide. Neutron spin echo (NSE) coils containing neutron guides made of float glass, were put on stream, and first NSE measurements showed that beam polarization was partially lost also in the attenuation/monitor zone. The guide field in this region was hence modified during the shutdown of FRM-II in September and October, and the attenuator shielding was improved.

At the same time, the RF circuits were finished and put into operation with the new RF amplifiers. The NRSE coils

were put into operation, and in November, the first NRSE echo groups could be detected. Though the beam polarization is not perfect, the NRSE data - a typical echo group plot is shown in Fig. 2 - demonstrate that all the components of RESEDA work properly.

The mean neutron wavelength of the primary beam at the selector frequency 22000 rpm is 5.3 Å, as extracted from the NRSE data, and the width of the wavelength band amounts to 13% (FWHM). The minimum wavelength at the maximum selector frequency of 28000 rpm is expected to be 4.2 Å. By turning the selector, this value can be still reduced. However, the angle of the selector is restricted by the monochromator of the instrument NOSPEC joining the same neutron guide and selector housing. The minimum available wavelength is therefore expected to be about 3.7 Å.

We finally investigated the dependence of the NRSE polarization from several parameters, as the magnetic fields in the coupling coils and the solenoids fixed at the mumetal shielding, and as a function of the RF frequency. Besides the predominantly expected results from these tests, it turned out that the polarization depends on the position of the crane in the neutron guide hall due to its stray fields. Further test measurements, especially of the polarization as a function of the wavelength of the beam and its divergence are in preparation.

Similarly as in 2004, the progress at RESEDA during 2005 was again very impressive. Within less than two years, a practically new instrument has been built, including neutron guide shielding, selector housing, beam shutters and attenuators, NRSE coils, cooling and security systems, complete cabling of the instrument, completely new instrument control software etc. Commissioning of RESEDA will presumably take place in 2006, depending on the available manpower.



Figure 1: The image shows the two secondary spectrometer arms of RESEDA. The open mumetal shielding gives free view on the NSE and NRSE coils.

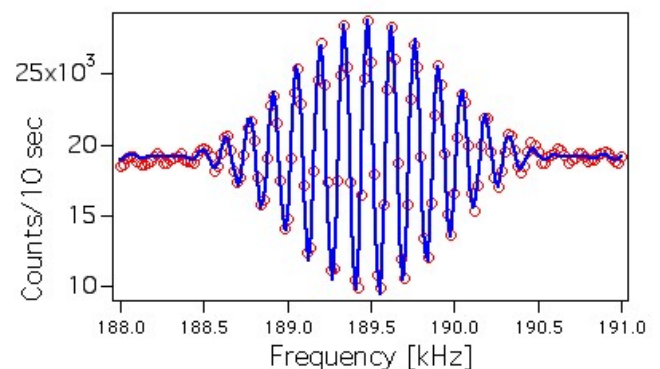


Figure 2: A typical NRSE echo group. The RF frequency in the first spectrometer arm is fixed to 189.5 kHz. The RF frequency in the second arm is scanned around the same value. The mean neutron wavelength extracted from the fit with the theoretical function is 5.3 Å, the width of the wavelength band is 13% (FWHM).

7.7 MIRA – The beam line for very cold neutrons at the FRM-II

Robert Georgii^{1, 2}

¹Physics Department E21, Technical University Munich, 85747 Garching, Germany

²ZWE FRM-II, Technical University Munich, 85747 Garching, Germany

MIRA is a versatile instrument for very cold neutrons (VCN) using neutrons with a wavelength $\lambda > 8 \text{ \AA}$ (see Fig. 1). It is situated at the cold neutron guide NL6b in the neutron guide hall of the FRM-II. As the instrument set-up can be changed quickly, MIRA is ideally suited as a testing platform for realising new instrumental set-ups and ideas. In particular, MIRA is unique in its possibilities of combining different neutron scattering methods as:

- Polarized or non-polarized reflectometry.
- Polarized or non-polarized small angle scattering (SANS).
- Classical NRSE (Neutron Resonance Spin Echo) setup as well as using the MIEZE principle.

Design of the instrument

The instrument is located at the end of an 8 m long curved ^{58}Ni neutron guide ($R = 84 \text{ m}$) with a cross section of $10 \text{ mm} \times 120 \text{ mm}$. The instrument is fed by means of a wavelength sensitive switch from neutron guide NL6. The radius of curvature of the guide and its coating limit the critical wavelength of MIRA to about 8 \AA . The monochromator mechanics at the end of the guide is situated inside a massively shielded drum. The multilayer monochromator presently used ($m = 4.3$) allows for choosing wavelengths between 8 \AA and 30 \AA . After monochromatization the neutrons are then guided through a vacuum tube to the sample position, with the desired sample environment (e.g. low temperatures, magnetic fields). The reflection geometry is vertical, so that $\vartheta - 2\vartheta$ scans can be performed.

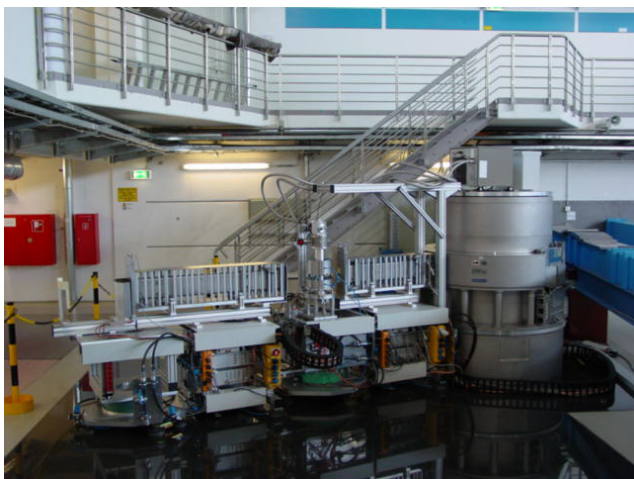


Figure 1: Mira equipped with a magnet and a cryostat. In order to reduce scattering by air, the neutrons travel in evacuated tubes before and after the sample.

Furthermore, the sample table is equipped with a 3D-goniometer for sample orientation. The scattered neutrons are detected either by means of a ^3He detector or 2-dimensional position sensitive detector (PSD). A slit system of four apertures before and behind the monochromator and the sample position is used to define the momentum resolution of MIRA. An optical bench allows for quickly changing the different instrumental set-ups.

Wavelength range	$8 \text{ \AA} - 30 \text{ \AA}$
Monochromatic flux	$4 \cdot 10^5 \text{ \AA}^{-1}\text{s}^{-1}\text{cm}^{-2}$ at 10 \AA
Momentum transfer	$0.005 \text{ \AA}^{-1} < Q < 1.1 \text{ \AA}^{-1}$
Largest observable length	$0.4 \cdot 10^{-6} \text{ m}$
Angular Resolution	0.05°
Temperature range	$180 \text{ mK} - 2000 \text{ K}$
Available magnets	$B < 0.5 \text{ T}$ vertical, horiz. $B < 10 \text{ T}$ vertical
Polarization analysis	2 multilayer benders
Detector	$180 \text{ mm} \times 180 \text{ mm}$ PSD resolution $1 \text{ mm} \times 2 \text{ mm}$ single ^3He detector

Table 1: Instrument parameters of MIRA

Furthermore, after the monochromator the neutrons may be polarized. They are guided in a guide field of 60 Gauss provided by permanent magnets. Multilayer benders with a polarization efficiency of 95% are used for determining the polarization of the neutrons before and after scattering. All moving parts, the NRSE electronics and the readout of the detectors are fully automated and controlled by the experiment software.

This year MIRA was successfully taken into user operation. In total, 6 proposals, several test and service measurements were performed, for example a test of a switchable polarization He^3 spin filter for the ILL. Two diploma theses (*The flux line lattice of Niobium* by Sebastian Mühlbauer, E21; *Entwicklung eines positionsempfindlichen Detektors für intensive Neutronenstrahlen* by Stefan Rummel, E18) and one Ph.D. thesis (*Small angle scattering on MnSi* by Daniel Lamago, FRM-II) were finished using mainly data from MIRA. Also major parts of the beam time went in another Ph.D. thesis for the development of a double MIEZE spectrometer (Nikolas Arend, E21), which will be finished next year.

This work is kindly supported by the EU FP6 project under contract number HII3-CT-2003-505925, project JRA5/PNT.

7.8 Multiple Small Angle Neutron Scattering

Thomas Hils¹, Roland Gähler², Peter Böni¹

¹ Physics Department E21, Technical University Munich, 85747 Garching, Germany

² Institut Laue-Langevin, 38042 Grenoble Cedex 9, France

Research on polymers, colloid systems, cements, microporous media, are examples of a rising field where μm -correlations play a crucial role. Small angle X-ray and neutron scattering (SAXS and SANS) typically measure lateral correlation lengths in the 0.01 to 1 μm range, the q -resolution ranging up to 10^{-3} \AA^{-1} . To measure larger μm correlations with neutrons, the q -resolution has to be improved and various specific instruments have been designed. The technique is commonly known as USANS (Ultra Small Angle Neutron Scattering). However these methods are sensitive to scattering only in one dimension and often suffer from intrinsic small angle scattering due to structure material in the beam.

Here we propose MSANS (Multi hole SANS), a new USANS option for a standard long baseline SANS instrument. It uses the common SANS infrastructure except for the detector, which requires enhanced spatial resolution. We aim at improving the q -resolution to about 10^{-5} \AA^{-1} at 10 \AA , so correlations up to 60 μm should be possible. The system is sketched in Fig. 1.

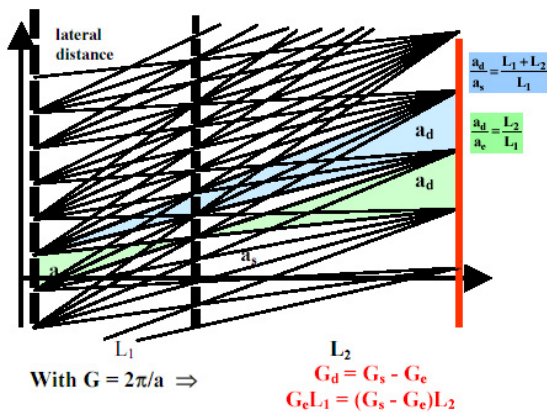


Figure 1: Condition for the lattice constants a_e and a_s and distances L_1 and L_2 for 'focussing' in the detector plane d .

It is based on multi-hole apertures at the entrance (M_e) of the collimator and near the sample (M_s) with lattice constants a_e and a_s and hole diameters d_e and d_s respectively. With the choice

$$G_{e,s} = \frac{2\pi}{a_{e,s}}; G_e \cdot L_1 = (G_s - G_e)L_2; G_d = G_s - G_e$$

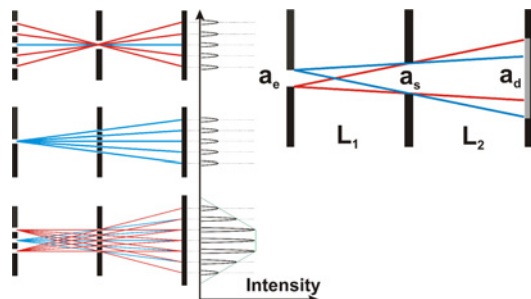


Figure 2: The number and intensity of spots depend on the number of holes of sample and entrance mask (left side); the width of spots at the detector depends on the width of entrance and sample aperture (right side).

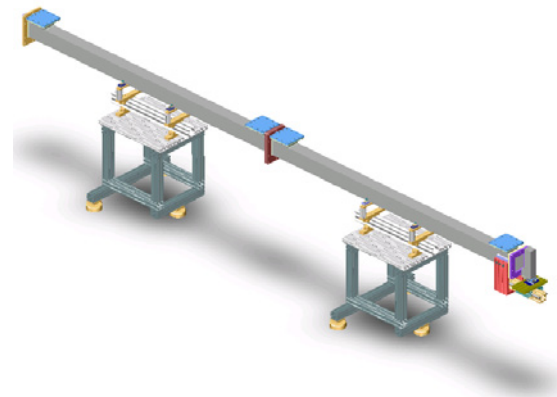


Figure 3: MSANS setup.

an intensity pattern of well separated peaks with lattice constant a_d in the detector plane is observed ($a_d=2/G_d$). Short range correlations in the sample may lead to significant overlap, however typical SANS intensities drop very rapidly with increasing q , and overlap will not be fatal in many cases. Sets of apertures with different relations $a_{e,s}/d_{e,s}$ (d diameter of hole apertures) can be used to adapt the pattern to the demand. In MSANS, resolution is decoupled from intensity, as long as the transmission of apertures is kept constant. The increase in q -resolution in MSANS is typically one order of magnitude, compared to SANS at equal intensity. The gain originates from the reduction in q -range in MSANS and the increase of the input guide cross section and its divergence. Diffraction from the aperture holes of typically 1 mm is not yet crucial, as the beam correlation length is only in the μm range.

Prototypes of a set of multihole-apertures based on cadmium and coated with typ. 13 μm ^{10}B were produced with the following properties: hole diameter $d_{e,s} = 0.5/1\text{mm}$; lattice constant $a_{e,s} = 2.5/5 \text{ mm}$. The proposed configuration at TUM leads to $\text{FWHM} \approx 1 \text{ mm}$.

In 2005 the basic test-design consisting of flight-tubes, the multihole-apertures, position-sensitive detector and the appropriate auxiliaries like tables, mountings etc have been designed and are currently manufactured.

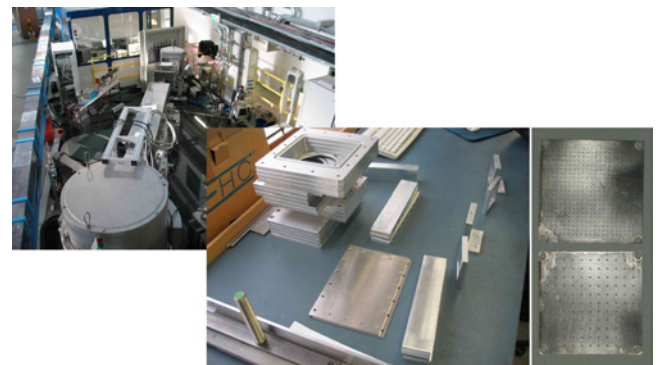


Figure 4: Basic geometry of the MIRA beamline at FRM-II (left) and manufactured aperture-frames, flanges etc (right).

8

Activities 2005



8.1 Lectures, Courses and Seminars

N. Arend	Practical course "Anfängerpraktikum für Physiker"
P. Böni	Lecture "Magnetic Excitations: Theory and Experiment I" Tutorial "Magnetic Excitations: Theory and Experiment I" Lecture "Magnetic Excitations: Theory and Experiment II" Tutorial "Magnetic Excitations: Theory and Experiment II" Lecture "Polarized Neutrons", School on Pulsed Neutron Sources, Oct. 17-28 2005, The Abdus Salam International Centre for Theoretical Physics. Seminar "Neutronen in Industrie and Forschung", together with Profs. Petry and Schreckenbach Seminar "Experimentelle Methoden in der Festkörperphysik" together with Prof. C. Pfeiderer and Dr. C. Hugenschmidt
K. Böning	Lecture "Reaktorphysik II und neue Konzepte in der Kerntechnik"
J. Brunner	Practical course "Elektronikpraktikum"
R. Georgii	Seminar "Neutronen in Forschung und Industrie" Seminar "2 nd FRM-II Workshop on Neutron Scattering - Advanced Materials, Burg Rothenfels"
F. Grünauer	Practical course "Anfängerpraktikum für Physiker"
W. Häußler	Seminar "Neutronen in Forschung und Industrie"
C. Hugenschmidt	Seminar "Experimentelle Methoden der Festkörperphysik"
V. Kargl	Tutorial "Experimental Physics II"
T. Keller	Practical course "Elektronikpraktikum"
D. Lamago	Practical course and Tutorial "F-Praktikum Superfluides Helium"
K. Lorenz	Practical course "Elektronikpraktikum"
M. Mühlbauer	Practical course "Elektronikpraktikum"
S. Mühlbauer	Tutorial "Experimental Physics II"
P. Niklowitz	Tutorial "Experimental Physics for Geodesy and Geoinformation"
C. Pfeiderer	Seminar "Quantenphasenübergänge (Theorie und Experiment)" Lecture "Experimentalphysik 1 für Geodäsie und Geoinformation"
W. Potzel	Practical course "Elektronikpraktikum"
C. Schanzer	Practical course "Demonstrationspraktikum für Lehramt Physik"
B. Schillinger	Practical course "Elektronikpraktikum"
K. Schreckenbach	Seminar "Neutronen in Industrie and Forschung", together with Profs. Böni and Petry
M. Stadlbauer	Tutorial "Experimental Physics II"
N. Wieschalla	Tutorial "Reaktorphysik II und neue Konzepte in der Kerntechnik"

8.2 Seminar “Neutronen in Industrie und Forschung” 2005

Date	Speaker	Title
Jan 17	Dirk Holland-Moritz (DLR, Institut für Raumsimulation)	Neutronenstreuexperimente an unterkühlten Metallschmelzen
Jan 24	M. Monkenbusch (Forschungszentrum Jülich)	Membranelastizität und Fluktuationen in Mikroemulsionen: SANS und NSE Untersuchungen
Feb 7	Shane Kim (ANSTO, Australia)	Current status of instrumentation at ANSTO
Feb 14	Hans Lauter (ILL, Grenoble)	Larmor precession for angular encoding and reflectometry
Mar 13	C. J. Schmidt und M. Klein (Physikalisches Institut der Universität Heidelberg)	CASCADE - Ein hochratentauglicher Flächendetektor für thermische und kalte Neutronen
Apr 1	Dr. Philipp Niklowitz (CEA, Grenoble)	Unconventional metallic behaviour of materials at the border of magnetic order
Apr 25	Dr. S. Masalovich (FRM-II)	Polarized ^3He gas: production and application in neutron instrumentation
May 2	Dr. Dan Neumann (National Institute of Standards and Technology (NIST), USA)	Backscattering spectroscopy at the NCNR and the tunneling of confined tops
May 4	Dr. Dan Neumann (NIST, USA)	Backscattering spectroscopy at the NCNR and the tunneling of confined tops
May 11	Dr. Alexander Ioffe (Forschungszentrum Jülich, Institut für Festkörperforschung)	Neutron instrumentation of the JCNS (Jülich Center for Neutron Science) at FRM-II
May 23	Maikel C. Rheinstädter (ILL, Grenoble)	Collective dynamics of lipid membranes studied by inelastic neutron scattering
May 30	Dr. Karl Zeitelhack (FRM-II)	Measurement of neutron flux and beam divergence at the neutron guide system of FRM-II
Jun 6	Prof. Dr. M. Kenzelmann (PSI, Switzerland)	Competing spin interactions as a new route to multiferroic materials
Jun 13	Dr. Mechthild Enderle (ILL, Grenoble)	Macroscopic quantum ground states in antiferromagnetic spin systems
Jun 20	Dr. S. Bayrakci and Dr. T. Keller (MPI Stuttgart)	First experiments at TRISP
Jun 27	Dr. R. Kampmann (Institute for Materials Research, GKSS Research Centre)	2D-Multi-Wire Gaseous Neutron Detectors with High Count Rate Capability and High Relative Resolution
Jul 1	Dr. Sven Vogel (Los Alamos Neutron Science Center, USA)	Das TOF Neutronendiffraktometer HIPPO
Jul 4	Prof. D. Habs (LMU München)	Proposal for a high-brilliance micro-beam of low-energy polarized neutrons
Jul 11	T. Hürlimann (TUM/ILL, Grenoble)	Design und Simulation von Neutronenleitern mit adiabatischer Formänderung
Aug 1	Prof. H. Keppler (Universität Bayreuth)	Neutronen in der geowissenschaftlichen Hochdruckforschung
Aug 18	Camden R. Hubbard (Oak Ridge National Laboratory, USA)	New Neutron Instruments for Engineering Materials Science and Strain Measurement at HFIR and SNS
Sep 26	Dr. J. Walter (Universität Bonn)	Konzept eines neuen Flugzeit-Texturdefraktometers am FRM-II zur Gefügecharakterisierung
Oct 10	Prof. M. B. Maple (University of California, San Diego, USA)	Strongly correlated electron phenomena in Pr-based filled skutterudite compounds
Nov 4	Prof. B. Lengeler (RWTH Aachen)	Refraktive Linsen für Röntgen- und Neutronenstrahlung
Nov 7	Prof. George F. Chapline (Lawrence Livermore National Laboratory, USA)	Quantum criticality, event horizons, and quantum computing

Date	Speaker	Title
Nov 14	Prof. H. Zabel (Festkörperphysik, Ruhr-Universität Bochum)	Neutron Reflectivity on Magnetic Nanostructures
Nov 21	Prof. A. Magerl (Friedrich-Alexander Universität Erlangen-Nürnberg)	Struktur und Dynamik von komplexen Flüssigkeiten unter Scherung
Dec 5	Dr. C. Hugenschmidt (FRM-II/TUM)	The Positron Beam Facility NEPOMUC and Positron Experiments at FRM-II
Dec 12	Dr. F. Pfeiffer (Swiss Light Source, Paul-Scherrer-Institut, Switzerland)	X-ray and neutron phase contrast imaging
Dec 14	F. Czeschka (TUM)	Das MuPAD - 3D Polarisationsanalyse mit Neutronen
Dec 19	Prof. W. Petry, Dr. R. Georgii, Dr. M. Hofmann (FRM-II)	Berichte von der Internationalen NeutronenstreuKonferenz ICNS

8.3 Workshops 2005

Date	Title	Location
Sep 1	Workshop on Positron Physics and Positron Experiments, 1 st User-Meeting at NEPOMUC	ZWE FRM-II, GRS Building, Technical University Munich

8.4 Publications 2005

- [1] F. Affouard, E. Cochin, F. Danede, R. Decressain, M. Descamps, and W. Häußler. Onset of slow dynamics in difluoro-tetrachloroethane glassy crystal. *Journal of Chemical Physics*, 123/8:084501, 2005.
- [2] S. Barakat, D. Braithwaite, P. Alireza, K. Grube, M. Uhlarz, J. Wilson, C. Pfleiderer, J. Flouquet, and G. Lonzarich. High Pressure Investigations of the Itinerant Ferromagnet CoS_2 . *Physica B*, 2005.
- [3] H. Bartolf, C. Pfleiderer, O. Stockert, M. Vojta, and H. v. Löhneysen. Hall effect across the Quantum Phase Transition of $\text{CeCu}_{6-x}\text{Au}_x$. *Physica B*, 2005.
- [4] A. Bogdanov, U. K. Rössler, and C. Pfleiderer. Modulated and Localised Structures in Cubic Helimagnets. *Physica B*, 2005.
- [5] P. Böni and B. Roessli. Magnetic Excitations in Incommensurate Itinerant Systems. *The Physics of Metals and Metallography*, 99:S80, 2005.
- [6] H. B. Braun, J. Kulda, B. Roessli, D. Visser, K. W. Krämer, H. U. Güdel, and P. Böni. Emergence of Soliton Chirality in a Quantum Antiferromagnet. *Nature Physics*, 1:159–163, 2005.
- [7] J. Brunner, M. Engelhardt, G. Frei, A. Gildemeister, E. Lehmann, A. Hillenbach, and B. Schillinger. Characterization of the image quality in neutron radiography. *Nucl. Instr. Meth. A*, 542:123–128, 2005.
- [8] T. Bücherl, B. Schillinger, A. Türlér, and P. Böni, editors. *Proceedings of the 5th International Topical Meeting on Neutron Radiography ITMNR-5, Garching, Germany, July 26 - 30 2004*, volume 542 of *Reprinted from Nuclear Instruments and Methods in Physics Research, Section A*. ELSEVIER, 2005.
- [9] E. Calzada, B. Schillinger, and F. Grünauer. Construction and assembly of the neutron radiography and tomography facility ANTARES at FRM II. *Nucl. Instr. Meth. A*, 542:38–44, 2005.
- [10] E. Clementyev, P. A. Alekseev, P. Allenspach, and V. N. Lazukov. Magnetic Excitations in the Singlet-Ground-State Ferromagnet PrNi. *Physics of Metals and Metallography*, 99 suppl. 1:12–14, 2005.
- [11] S. Drobnik, K. Grube, C. Pfleiderer, H. v. Löhneysen, E. D. Bauer, and M. B. Maple. AC Susceptibility Study of the Superconductivity of $\text{PrOs}_4\text{Sb}_{12}$. *Physica B*, 2005.
- [12] S. Drotziger, C. Pfleiderer, M. Uhlarz, H. v. Löhneysen, D. Souptel, W. Löser, and G. Behr. Pressure Induced Magnetic Quantum Phase Transition in CeSi_{2-x} . *Physica B*, 2005.
- [13] J. Gapinski, A. Wilk, A. Patkowski, W. Häußler, A. J. Banchio, R. Pecora, and G. Nägele. Diffusion and microstructural properties of solutions of charged nanosized proteins: Experiment versus theory. *Journal of Chemical Physics*, 123/5:054708, 2005.
- [14] T. Görlach, C. Pfleiderer, K. Grube, and H. v. Löhneysen. Low Temperature Properties of YbAl_2 . *Phys. Rev. B*, 2005.
- [15] S. V. Grigoriev, S. V. Maleyev, A. I. Okorokov, Y. O. Chetverikov, R. Georgii, P. Böni, D. Lamago, H. Eckerlebe, and K. Pranzas. Critical fluctuations in MnSi near T_c : A polarized neutron scattering study. *Phys. Rev. B*, 72:134420–1 – 134420–5, 2005.
- [16] J. P. Hague, E. M. Chung, D. Visser, G. Balakrishnan, E. Clementyev, D. M. Paul, and M. R. Lees. Spin wave dispersion and magnons from short range order in tapiolite (FeTa_2O_6); a quasi-two-dimensional antiferromagnet. *J. of Physics: Condensed Matter*, 17:7227–7235, 2005.
- [17] F. Hardy, A. D. Huxley, J. Flouquet, B. Salce, G. Knebel, D. Braithwaite, D. Aoki, M. Uhlarz, and C. Pfleiderer. (P,T) Phase Diagram of the Ferromagnetic Superconductor URhGe. *Physica B*, 2005.
- [18] W. Häußler and U. Schmidt. Effective field integral subtraction by the combination of spin echo and resonance spin echo. *Journal of Physical Chemistry Chemical Physics*, 7/6:1245–1249, 2005.
- [19] C. Hugenschmidt, K. Schreckenbach, M. Stadlbauer, and B. Straßer. Low energy positrons of high intensity at the new positron beam facility NEPOMUC. *Nucl. Instr. Meth. A*, 554(1-3):384–391, 2005.
- [20] M. Janoschek, B. Roessli, L. Keller, S. N. Gvasaliya, K. Conder, and E. Pomjakushina. Reduction of the ordered magnetic moment in YMnO_3 with hydrostatic pressure. *J. Phys.: Condens. Matter*, 17:425–430, 2005.
- [21] H. Jobic, J. Karger, C. Krause, S. Brandani, A. Gunadi, A. Methivier, G. Ehlers, B. Farago, W. Häußler, and D. M. Ruthven. Diffusivities of n-alkanes in 5A zeolite measured by neutron spin echo, pulsed-field gradient NMR, and zero length column techniques. *Adsorption-Journal of the International Adsorption Society*, 11/Suppl.1:403–407, 2005.
- [22] N. Kardjilov, P. Böni, A. Hilger, M. Strobl, and W. Treimer. Characterization of a Focusing Parabolic Guide Using Neutron Radiography Method. *Nucl. Instr. Meth. A*, 542:248–252, 2005.
- [23] V. Kargl, P. Böni, A. Mirmelstein, B. Roessli, and D. Sheptyakov. Magnetic neutron diffraction in $\text{Ca}_{2+x}\text{Y}_{2-x}\text{Cu}_5\text{O}_{10}$. *Physica B*, 359-361:1255, 2005.
- [24] H. C. Kim, Younghun Jo, J.-G. Park, S. W. Cheong, M. Uhlarz, C. Pfleiderer, and H. v. Löhneysen. Magnetic State of Pyrochlore $\text{Gd}_2\text{Mo}_2\text{O}_7$ Studied by Pressure Dependent Magnetization Measurements. *Physica B*, 2005.
- [25] D. Lamago, R. Georgii, and P. Böni. Magnetic susceptibility and specific heat of the itinerant ferromagnet MnSi . *Physica B*, 359-361:1171–1173, 2005.

- [26] Eberhard Lehmann, Klaus Lorenz, Erich Steichele, and Peter Vontobel. Non-destructive testing with neutron phase contrast imaging. *Nucl. Instr. and Meth. in Phys. Res. A*, 542:95–99, 2005.
- [27] M. Mühlbauer, E. Calzada, and B. Schillinger. Development of a system for neutron radiography and tomography. *Nucl. Inst. Meth. A*, 542:324–328, 2005.
- [28] F. Obermair, C. Pfleiderer, P. Raychaudhuri, R. C. Perry, and Y. Maeno. Magnetic Field Dependence of the Specific Heat of $\text{Sr}_3\text{Ru}_2\text{O}_7$. *Physica B*, 2005.
- [29] A. I. Okorokov, S. V. Grigoriev, Y. O. Chetverikov, S. V. Maleyev, R. Georgii, P. Böni, D. Lamago, H. Eckerlebe, and K. Pranzas. The effect of the magnetic field on the spiral spin structure in MnSi studied by polarized SANS. *Physica B*, 356:259–263, 2005.
- [30] C. Pfleiderer. Why First Order Quantum Phase Transitions are Interesting. *J. Phys.: Condens. Matter*, 2005.
- [31] C. Pfleiderer, A. D. Huxley, and S. M. Hayden. On the Use of Cu:Be Clamp Cells in Magnetisation and Neutron Scattering Studies. *J. Phys.: Condens. Matter*, 2005.
- [32] C. Pfleiderer, L. Pintschovius, D. Reznick, and H. v. Löhneysen. Chirality of Magnetic-Field Aligned Helical Order in MnSi at High Pressure. *Physica B*, 2005.
- [33] C. Schanzer, V. R. Shah, T. Gutberlet, M. Gupta, P. Böni, and H. B. Braun. Magnetic depth profiling of FM/AF/FM trilayers by PNR. *Physica B*, 356:46, 2005.
- [34] B. Schillinger, H. Abele, J. Brunner, G. Frei, R. Gähler, A. Gildemeister, A. Hillenbach, E. Lehmann, and P. Vontobel. Detection systems for short-time stroboscopic neutron imaging and measurements on a rotating engine. *Nucl. Inst. Meth. A*, 542:142–147, 2005.
- [35] B. Schillinger and E. Calzada. Proposed combination of CAD data and discrete tomography for the detection of coking and lubricants in turbine blades or engines. In *Proceedings of the Workshop on Discrete Tomography and its Applications*, volume 20, pages 493–499. Electronic Notes in Discrete Mathematics, <http://www.sciencedirect.com/science/journal/15710653>, July 2005.
- [36] K. Schreckenbach. Nuclear and Particle Physics at the New Neutron Source FRM-II. *Nuclear Physics News*, 15(4), 2005.
- [37] V. R. Shah, C. Schanzer, P. Böni, and H. B. Braun. Interface and magnetic characterization of FM/AF/FM multilayers. In J. J. M. Franse, V. Eremenko, and V. Sirenko, editors, *Proceedings of the NATO Advanced Research Workshop: Smart materials for ranging systems*, pages 179–194. Kluwer Academic Press, Dordrecht/Boston/London published in co-operation with NATO Scientific Affairs Division, 2005.
- [38] V. R. Shah, C. Schanzer, P. Böni, and H. B. Braun. Magnetization reversal in FM/AF/FM trilayers: dependence of AF thickness. *Journal of Magnetism and Magnetic Materials*, 286:484–487, 2005.
- [39] M. Uhlarz, C. Pfleiderer, and S. M. Hayden. Quantum Phase Transitions in the Itinerant Ferromagnet ZrZn_2 . *Physica B*, 2005.
- [40] N. Volkov, G. Petrakovskii, P. Böni, E. Clementyev, K. Patrin, K. Sablina, E. Eremin, and V. Vasiliev. Magnetic and transport properties of $(\text{La}_{0.4}\text{Eu}_{0.6})_{0.7}\text{Pb}_{0.3}\text{MnO}_3$ single crystal: The key role of intrinsic inhomogeneity. *J. of Magnetism and Magnetic Materials*, 300, 2005.
- [41] F. Weber, A. Cosceev, C. Pfleiderer, A. Nateprov, A. Faißt, M. Uhlarz, and H. v. Löhneysen. Single-Crystal Studies of the Europium Pnictide: EuZn_2Sb_2 . *Physica B*, 2005.
- [42] E. A. Yelland, S. M. Hayden, S. J. C. Yates, C. Pfleiderer, M. Uhlarz, R. Vollmer, H. v. Löhneysen, N. R. Bernhoeft, R. P. Smith, S. S. Saxena, and N. Kimura. Surface Sensitive Superconductivity in ZrZn_2 . *Phys. Rev. B*, 72(214523), 2005. cond-mat/05023411.

8.5 Conference, Workshop and Seminar Contributions 2005

- [1] P. Böni. Chromium: The Unresolved Problem. Talk. *Seminar Condensed Matter Physics, Brookhaven National Laboratory*, September 1 2005. Upton, NY, USA.
- [2] P. Böni. Forschung am Lehrstuhl E21. Talk. *Informationsveranstaltung für Studenten*, December 1 2005. Physics Department, Technical University Munich, Garching, Germany.
- [3] P. Böni. Inelastische Neutronenstreuung: Magnetismus, Neutronenstreuung für Kristallographen. Talk. *Deutsche Kristallographische Gesellschaft*, September 29-30 2005. LMU/TUM, Munich, Germany.
- [4] P. Böni. Magnetismus in dünnen Filmen und Multischichten. Talk. *Edgar Lüscher Lectures 'Physik im Nanometerbereich'*, October 4-7 2005. Dillingen.
- [5] P. Böni. Mit Neutronen dem Magnetismus auf der Spur. Talk. *NaT-Working Garching*, January 12 2005. Technical University Munich, Garching, Germany.
- [6] P. Böni. Neutron Imaging Using Elliptic Guides. Talk. *International Workshop on Radiography*, October 13-14 2005. Paul Scherrer Institute, Villigen, Switzerland.
- [7] P. Böni. Neutron Optics - Phase Space Transformation. Talk. *NMI3 General Meeting 2005, Rutherford Appleton Laboratory*, September 28 2005. Didcot, UK.
- [8] P. Böni. Neutronenmethodik. Talk. *Evaluation BMBF Verbundforschung*, April 4 2005. Technical University Munich, Munich, Germany.
- [9] P. Böni. Polarized Neutrons. Talk. *School on Pulsed Neutron Sources, The Abdus Salam International Centre for Theoretical Physics*, Oct. 17-28 2005. Trieste, Italy.
- [10] E. Clementyev, P. Böni, and F. Demmel. Mapping of magnetic excitations in single-Q chromium. Talk. *SINQ Users Meeting*, Jan 2005. Villigen, Switzerland.
- [11] E., K. Lorenz, and B. Schillinger. Phase contrast radiography with X-rays and neutrons. Talk. *Coherence 2005*, May 2005. Porquerolles, France.
- [12] W. Häußler. Resonance Spin Echo at the FRM-II. RESEDA: present status and future planning. Talk. *Neutron Spin Echo Seminar, Universität Heidelberg*, November 2005. Heidelberg, Germany.
- [13] W. Häußler. The Resonance Spin Echo spectrometer RESEDA at the FRM-II - design and present status. Talk. *Neutron Spin Echo workshop 2005*, September 2005. Grenoble, France.
- [14] W. Häußler. Structure and Dynamics in Ferritin solutions measured by Neutron Spin Echo spectroscopy. Talk. *Klausurtagung FRM-II*, July 2005. Rothenfels, Germany.
- [15] W. Häußler, A. Patkowski, and A. Wilk. Neutron Spin Echo spectroscopy of Ferritin: Solution Structure and Dynamics of a model colloid. Poster. *Liquid Matter Conference 2005*, July 2005. Utrecht, Netherlands.
- [16] C. Hugenschmidt. Erste Experimente am FRM-II. Talk. *Kernphysikalisches Kolloquium Helmholtz-Institut für Strahlen- und Kernphysik*, April 2005. Universität Bonn, Germany.
- [17] C. Hugenschmidt. Investigation of the near surface region of chemically treated and Al-coated PMMA by Doppler-broadening spectroscopy. Talk. *PPC-7, 8th International Workshop on Positron and Positronium Chemistry*, September 2005. Coimbra, Portugal.
- [18] C. Hugenschmidt. NEPOMUC – Neutron Induced Positron Source Munich and First Positron Experiments. Plenary talk. *SLOPOS-10, 10th International Workshop on Slow Positron Beam Techniques for Solids and Surfaces*, March 2005. Doha, Qatar.
- [19] C. Hugenschmidt. Positron Physics and First Experiments at NEPOMUC. Talk. *Seminar Institut Laue Langevin*, October 2005. Grenoble, France.
- [20] C. Hugenschmidt. Positron Physics and First Experiments at NEPOMUC. Talk, November 2005. Petten, Netherlands.
- [21] M. Janoschek, S. Klimko, M. Medarde, R. Gähler, B. Roesslia, and P. Böni. MuPAD: A 3D Neutron Polarimeter for SINQ and FRM-II. Talk. *School on Polarized Neutrons for Material and Life Sciences*, June 2005. Anglet, France.
- [22] M. Janoschek, M. Medarde, J. Rodriguez-Carvajal, B. Roesslia, S. Klimko, and P. Böni. Spherical neutron polarimetry analysis with FullProf: soon a reality. Talk. *School on Polarized Neutrons for Material and Life Sciences*, June 2005. Anglet, France.
- [23] D. Lamago. Experimental investigation of spin and wavevector reorientation in itinerant magnets. Talk. *Klausurtagung FRM-II*, July 2005. Rothenfels, Germany.
- [24] E. Lehmann, K. Lorenz, B. Schillinger, and P. Vontobel. Phase contrast radiography with CCD and IP detectors. Talk. *International Workshop on „Neutron Imaging using Cold Neutrons and related topics“*, October 2005. PSI, Villigen, Switzerland.
- [25] K. Lorenz. From Qualitative to Quantitative Phase Contrast Imaging. Talk. *2nd FRM-II Workshop on Neutron Scattering*, July 2005. Rothenfels, Germany.
- [26] K. Lorenz, E. Steichele, and E. Lehmann. Non-destructive testing with neutron phase contrast imaging. Talk. *DPG Frühjahrstagung*, March 2005. Berlin, Germany.

- [27] S. Mühlbauer, R. Georgii, and P. Böni. SANS measurements of the Flux Line Lattice in Niobium - First Measurements on MIRA. Poster. *Frühjahrstagung der deutschen physikalischen Gesellschaft*, March 2005. Berlin, Germany.
- [28] S. Mühlbauer, M. Stadlbauer, P. Böni, C. Schanzer, J. Stahn, and U. Filges. Performance of an elliptically tapered neutron guide. Poster. *ICNS*, December 2005. Sydney, Australia.
- [29] C. Pfleiderer. Bericht über laufende Arbeiten. Talk. *Arbeitskreis intermetallische Verbindungen der DGKK*, October 13 2005. Universität Frankfurt.
- [30] C. Pfleiderer. Bulk Properties and Neutron Scattering of the Magnetic Phase Diagram of MnSi. Invited Talk. *SFB Workshop*, September 27 2005. Universität zu Köln.
- [31] C. Pfleiderer. Exotische Magnetische Strukturen. Invited Talk. *“Lüscher Lectures” über Physik im Nanometerbereich, Akademie für Lehrerfortbildung und Personalführung*, October 5 2005. Dillingen.
- [32] C. Pfleiderer. Novel Phases of Magnetic Metals. Colloquium Talk. *Großes Physikalisches Kolloquium*, December 9 2005. Universität Bonn.
- [33] C. Pfleiderer. Novel phases of magnetic metals. Colloquium Talk. *Großes Münchener Physik Kolloquium*, October 31 2005. Ludwigs Maximilian Universität, Munich.
- [34] C. Pfleiderer. Novel Phases of Magnetic Metals. Colloquium Talk. *Kolloquium von Universität Stuttgart und Max Planck Institute*, May 17 2005. Stuttgart.
- [35] C. Pfleiderer. On the Perspectives of Unravelling Emergent Behaviour of Complex Condensed Matter Systems. Invited Talk. *COST Workshop*, July 25 2005. Universität Wien.
- [36] C. Pfleiderer. Partial Magnetic Order in the Non-Fermi Liquid Phase of MnSi. Colloquium Talk. *Kolloquium des IFF*, November 28 2005. IFW Dresden.
- [37] C. Pfleiderer. Partial Order in the Non-Fermi Liquid Phase of MnSi. Invited Talk. *Workshop on Quantum Phase Transitions*, January 18-21 2005. Kavli Institute, University of California in Santa Barbara, USA.
- [38] C. Pfleiderer. Partial Order in the Non-Fermi Liquid Phase of MnSi (and comments on related materials). Invited Talk. *Workshop*, January 27-29 2005. University of Princeton, Princeton, USA.
- [39] C. Pfleiderer. Quantum Phase Transition in MnSi. Invited Talk. *IoP Workshop on Magnetism*, August 2-4 2005. Abingdon, Oxford, UK.
- [40] C. Pfleiderer. Quantum Phase Transitions in ZrZn₂. Invited Talk. *Workshop on Quantum Phase Transitions*, June 13 2005. Universität Karlsruhe.
- [41] C. Pfleiderer. Small Angle Neutron Scattering in MnSi at High Pressure. Talk. *Frühjahrstagung der deutschen physikalischen Gesellschaft*, March 4 2005. Berlin.
- [42] C. Pfleiderer. Superconducting Ferromagnets. Colloquium Talk. *SFB Kolloquium*, June 3 2005. Universität Regensburg.
- [43] C. Pfleiderer. The weird magnetism of MnSi. Colloquium Talk. *SFB Kolloquium*, October 25 2005. Universität Augsburg.
- [44] C. Pfleiderer. Why 1st order quantum phase transitions are interesting. Invited Talk. *Lawrence Livermore Laboratory*, January 24 2005. Stanford, USA.
- [45] C. Pfleiderer. Why 1st Order Quantum Phase Transitions are Interesting. Invited Talk. *Insitutsseminar*, January 10 2005. Physikalisches Institut, Universität Karlsruhe.
- [46] C. Pfleiderer. Why Quantum Phase Transitions in Magnetic Metals are Interesting. Invited Talk. *FRM-II Klausurtagung*, July 25-28 2005. Burg Rothenfels.
- [47] B. Schillinger and J. Brunner. Stroboscopic and continuous fast imaging with neutrons. Talk. *International Workshop “Imaging with cold neutrons”*, October 13-14 2005. PSI, Villigen, Switzerland.
- [48] K. Schreckenbach. Nukleare Inbetriebnahme des FRM-II. Talk. *Jahrestagung Kerntechnik 2005*, May 2005. Nürnberg.
- [49] K. Schreckenbach and H. Gerstenberg. Status Report on the Nuclear Start-up of the FRM-II. Talk. *RRFM 2005*, April 2005. Budapest, Hungary.
- [50] V. R. Shah. Synthesis and characterization of bulk and nanostructured magnetic materials. Invited talk. *Defense Metallurgical Research Laboratory*, July 19 2005. Hyderabad, India.
- [51] V. R. Shah, C. Schanzer, and P. Böni. Magnetic multilayers - interface to interlayer properties. Poster. *Nanotechnology Workshop (nanoTUM), Technical University Munich*, February 15 2005. Garching, Germany.
- [52] V. R. Shah, C. Schanzer, P. Böni, H. B. Braun, M. Gupta, T. Gutberlet, and M. Horisberger. PNR investigations on FM/AF/FM trilayers. Talk. *7th SINQ User Meeting*, January 27 2005. Villigen, PSI, Switzerland.
- [53] M. Stadlbauer, P. Böni, U. Filges, R. Gähler, T. Hürlimann, S. Mühlbauer, C. Schanzer, and J. Stahn. Simulations and First Experiments with an Elliptically Tapered Neutron Guide and Design and Simulation of Neutron Guides with Adiabatic Shape Transformation. Talk. *NMI3-Meeting*, September 2005. Oxford, UK.
- [54] M. Stadlbauer, P. Böni, U. Filges, S. Mühlbauer, C. Schanzer, and J. Stahn. Simulations and First Experiments with an Elliptically Tapered Neutron Guide. Talk. *NMI3-Meeting*, September 2005. Oxford, UK.
- [55] M. Stadlbauer, P. Böni, U. Filges, C. Schanzer, and J. Stahn. A Very Short Elliptic Neutron Guide - Simulations and Planned Experiments at FRM-II. Talk. *NMI3-Meeting*, May 2005. Paris, France.

- [56] M. Stadlbauer and C. Hugenschmidt. Charakterisierung der Elementumgebung von Defekten mit Hilfe der koinzidenten Doppler-Spektroskopie. Talk. *KFSI-Treffen*, October 2005. Neubiberg.
- [57] M. Stadlbauer and C. Hugenschmidt. Element-Specific Defect Investigation on Alloys with Coincident Doppler Broadening Spectroscopy. Talk. *FRM-II Klausurtagung*, July 2005. Rothenfels.
- [58] M. Stadlbauer, C. Hugenschmidt, and K. Schreckenbach. CDBS - Coincident Doppler Broadening Spectroscopy. Poster. *MiniWorkshop on Positron Physics*, September 2005. Garching.
- [59] M. Stadlbauer, C. Hugenschmidt, and K. Schreckenbach. Charakterisierung der Elementumgebung von Defekten mit Hilfe der koinzidenten Positronen-Doppler-Spektroskopie. Talk. *Lehrstuhlseminar Universität der Bundeswehr*, December 2005. Neubiberg.
- [60] M. Stadlbauer, C. Hugenschmidt, and B. Strasser. Messungen an thermisch belastetem Messing mit einem ortsauflösenden Doppler-Koinzidenzspektrometer am intensiven positronenstrahl nepomuc. Talk. *DPG Frühjahrstagung*, March 2005. Berlin.
- [61] M. Stadlbauer, C. Hugenschmidt, B. Straßer, and K. Schreckenbach. Spatially Resolved Investigation of Thermally Treated Brass with a Coincident Doppler-Spectrometer. Poster, *SLOPOS-10, 10th International Workshop on Slow Positron Beam Techniques for Solids and Surfaces*, March 2005. Doha, Qatar.
- [62] N. Wieschalla. Fuel for FRM-II. Talk. *PSI-Seminar, Lehrstuhl E12*, January 2005. Technical University Munich, Germany.
- [63] N. Wieschalla. Korrelationsfunktionen. Talk. *E21 Seminar*, June 2005. Technical University Munich, Germany.
- [64] N. Wieschalla. Methods of foil production of U-Mo monolithic. Talk. *CERCA*, January 2005. Romans-sur-Isere, France.
- [65] N. Wieschalla. Optical Analysis of irradiated U-Mo fuel. Talk. *CERCA*, January 2005. Romans-sur-Isere, France.
- [66] N. Wieschalla, A. Bergmaier, P. Böni, K. Böning, G. Dollinger, R. Grossmann, W. Petry, A. Röhrmoser, and J. Schneider. Heavy Ion Irradiation of UMo/Al Dispersion Fuel. Talk. *Reduced Enrichment for Research and Test Reactors*, November 2005. Boston, USA.

8.6 Filed Patents 2005

N. Wieschalla, P. Böni New manufacturing technique for U-Mo monolithic (patent reference no. DE 10 2005 055 692)

8.7 Committee Memberships

- P. Böni**
- Instrument Subcommittee, Institut Laue-Langevin, Grenoble, France
 - Reviewer of experimental proposals, GKSS, Geesthacht, Germany
 - Projektbegleitender Beirat FRM-II, Garching
 - Instrumentierungsausschuss FRM-II, Garching
 - TUM-Beirat für den FRM-II, Garching
 - Coordinator of Work Package on Neutron Optics, Joint Research Project JRA3: NMI3 FP6
 - Conference on Polarized Neutrons in Condensed Matter Research PNCMI 2004, Washington: Scientific Advisory Committee
 - 8th International Conference on the Physics of X-Ray Multilayer Structures PXRMS'06, member of program committee
- K. Schreckenbach**
- Chairman of the "Arbeitsgemeinschaft Forschungsreaktoren" (German research reactor operation group)
 - Chairman of the "Expert Advisory Committee" at the Institut Laue Langevin, Grenoble.
- B. Schillinger**
- Board member of the International Society for Neutron Radiography
 - Vice President of the European Society for Neutron Radiology
 - Conference Board Member for the 8th World Conference on Neutron Radiography, October 2006, NIST, Gaithersburg, USA

8.8 Accomplished PhD Theses

- Johannes Brunner** Quantitative time resolved neutron imaging methods at the high flux neutron source FRM-II
- Florian Grünauer** Design, optimization, and implementation of the new neutron radiography facility at FRM-II
- Jay Padiyath (at PSI)** Analysis of Sputtered Multilayers and Design of a Neutron Monochromator
- Christian Schanzer** Investigation of interlayer exchange coupling in ferro-/antiferro-/ferromagnetic trilayers

8.9 Accomplished Master's Theses

- Martin Mühlbauer** Bau eines Entwicklungssystems für Radiographie und Tomographie mit Neutronen (Building μ TOS)
- Sebastian Mühlbauer** Das Flussgitter in Niob – Messungen mit polarisierten und unpolarisierten Neutronen
- Michael Schulz** Aufbau einer Röntgenanlage für Radiographie und Tomographie am Experiment ANTARES am FRM-II
- Christian Piochacz** Entwicklung und Aufbau eines Transmissionsremoderators für Positronen
- Sebastian Stüber** Spin Wave Damping in the Isotropic Heisenberg Antiferromagnet RbMnF_3

8.10 Accomplished Bachelor Theses

- Tobias Hürlimann** Design of an adiabatic phase space transformer for neutrons

8.11 E21 Members

Phone/Fax: +49-89-289-

PH: Physics Department, RS: Reactor Station

Name	Phone	Fax	Room	email
Arend Nikolas, Dipl. Phys.	-12180	-14997	RS, 124	Nikolas.Arend@frm2.tum.de
Axtner Markus	-12125	-14997	RS, 140	maxtner@frm2.tum.de
Böni Peter, Prof. Dr.	-14711	-14713	PH 1, 2215	Peter.Boeni@frm2.tum.de
Böning Klaus, Prof. Dr.	-12150	-12191	FRM-II, UBA 0325	Klaus.Boening@frm2.tum.de
Brunner Thomas, Diplomand	-12179	-14997	RS, 103	Thomas.Brunner@frm2.tum.de
Bundschuh Ralph, Dipl. Phys.	+49-89- 636-48015	+49-89- 636-53810	Klinik für Nuklearmedizin Ismaninger Str. 22 81675 München	Ralph.Bundschuh@ph.tum.de
Engelhardt Martin, Dipl. Phys.	+49-89- 636-45791	+49-89- 636-53810	–	zfp.student@mchp.siemens.de
Gläser Wolfgang, Prof. emerit.	-12476	-12474	PH 1, 2279	wglaeser@ph.tum.de
Hils Thomas, Dr.	-14721	–	Flachbau, 17	thomas.hils@hils-consult.de
Janoschek Marc, Dipl. Phys.	–	–	–	marc.janoschek@psi.ch
Jones Sylvia, Secretary	-14712	-14713	PH 1, 2217	Sylvia.Jones@frm2.tum.de
Jungwirth Rainer, Diplomand	-12515	–	PH 1, 2373	Rainer.Jungwirth@frm2.tum.de
Krimmel Sven, Dipl. Phys.	+49-89- 636-45791	+49-89- 636-53810	–	xray.external@mchp.siemens.de
Lamago Daniel, Dipl. Phys.	-14740	-14997	PH 1, 2207	Daniel.Lamago@frm2.tum.de
Legl Stefan, Diplomand	-14907	-14997	Flachbau 14	Stefan.Legl@frm2.tum.de
Lorenz Klaus, Dipl. Phys.	-14741	-14997	RS, 146b	Klaus.Lorenz@frm2.tum.de
Mantwill Andreas, Mechaniker	-14887	–	–	–
Mayer Jakob, Diplomand	-12137	–	Flachbau 11	Jakob.Mayer@frm2.tum.de
Mühlbauer Martin, Dipl. Phys.	-14718	-14997	RS, 146b	Martin.Muehlbauer@frm2.tum.de
Mühlbauer Sebastian, Dipl. Phys.	-12515	–	PH 1, 2373	Sebastian.Muehlbauer@frm2.tum.de
Neubauer Andreas, Diplomand	-12515	–	PH 1, 2373	Andreas.Neubauer@frm2.tum.de
Niklowitz Philipp, Dr.	-14722	-14997	PH 1, 2207	Philipp.Niklowitz@frm2.tum.de
Pfleiderer Christian, Prof. Dr.	-14712	-14713	PH 1, 2205	Christian.Pfleiderer@frm2.tum.de
Piochacz Christian, Dipl. Phys.	-12179	-14997	RS, 103	Christian.Piochacz@frm2.tum.de
Reingen Gabriel, Mechaniker	-12656	–	PH 1, 1321	–
Russ Barbara, Dipl. Ing.	-14717	-14713	PH 1, 2207	Barbara.Russ@frm2.tum.de
Schreckenbach Klaus, Prof. Dr.	-12183	-12191	PH 1, 2201	Klaus.Schreckenbach@frm2.tum.de
Schulz Michael, Dipl. Phys.	-14718	-14997	RS, 146b	Michael.Schulz@frm2.tum.de
Stadlbauer Martin, Dipl. Phys.	-14631	-14997	RS, 103	Martin.Stadlbauer@frm2.tum.de
Streibl Dominik, Diplomand	-14775	-14997	RS, 124a	Dominik.Streibl@frm2.tum.de
Valloppilly Shah, Dr.	-14723	-14713	PH 1, 2205	shah@frm2.tum.de
Wieschalla Nico, Dipl. Phys.	-12111	-14997	RS, 124	Nico.Wieschalla@frm2.tum.de

8.12 Associated Members at FRM-II

Phone/Fax: +49-89-289-

PH: Physics Department, RS: Reactor Station

Name	Phone	Fax	Room	email
Calzada Elbio, Dipl. Ing.	-14611	-14997	RS, 126	Elbio.Calzada@frm2.tum.de
Georgii Robert, Dr.	-14986	-14989	NL-Halle, UYH 0336	Robert.Georgii@frm2.tum.de
Häußler Wolfgang, Dr.	-14921	-14989	NL-Halle, UYH 0334	Wolfgang.Haeussler@frm2.tum.de
Hugenschmidt Christoph, Dr.	-14609	-14997	RS, 103	Christoph.Hugenschmidt@frm2.tum.de
Morkel Christoph, Dr. habil.	-12157		FRM-II, UBA 0324	Christoph.Morkel@frm2.tum.de
Röhrmoser Anton, Dr.	-14890	-14995	FRM-II, UYH 0328	Anton.Roehrmoser@frm2.tum.de
Schillinger Burkhard, Dr.	-12185	-14997	RS, 127	Burkhard.Schillinger@frm2.tum.de
Schwikowski Reinhard, Techniker	-14915	-14995	NL-Halle, UYH 0336	Reinhard.Schwikowski@frm2.tum.de

PH: Physics Department

RS: Reactor Station

8.13 Guests

Phone/Fax: +49-89-289-

PH: Physics Department, RS: Reactor Station

Name	Phone	Fax	Room	email
Gähler Roland, Dr. habil.	+33-4-7620-7189	+33-4-7648-3906	–	gahler@ill.fr
Keller Thomas, Dr.	-12164	-14997	RS, 106	Thomas.Keller@frm2.tum.de
Li Hongyun	-14718	-14997	RS, 146b	Hongyun.Li@frm2.tum.de
Ning Qi	-12299	-14997	Flachbau 13	Ning.Qi@frm2.tum.de

PH: Physics Department

RS: Reactor Station

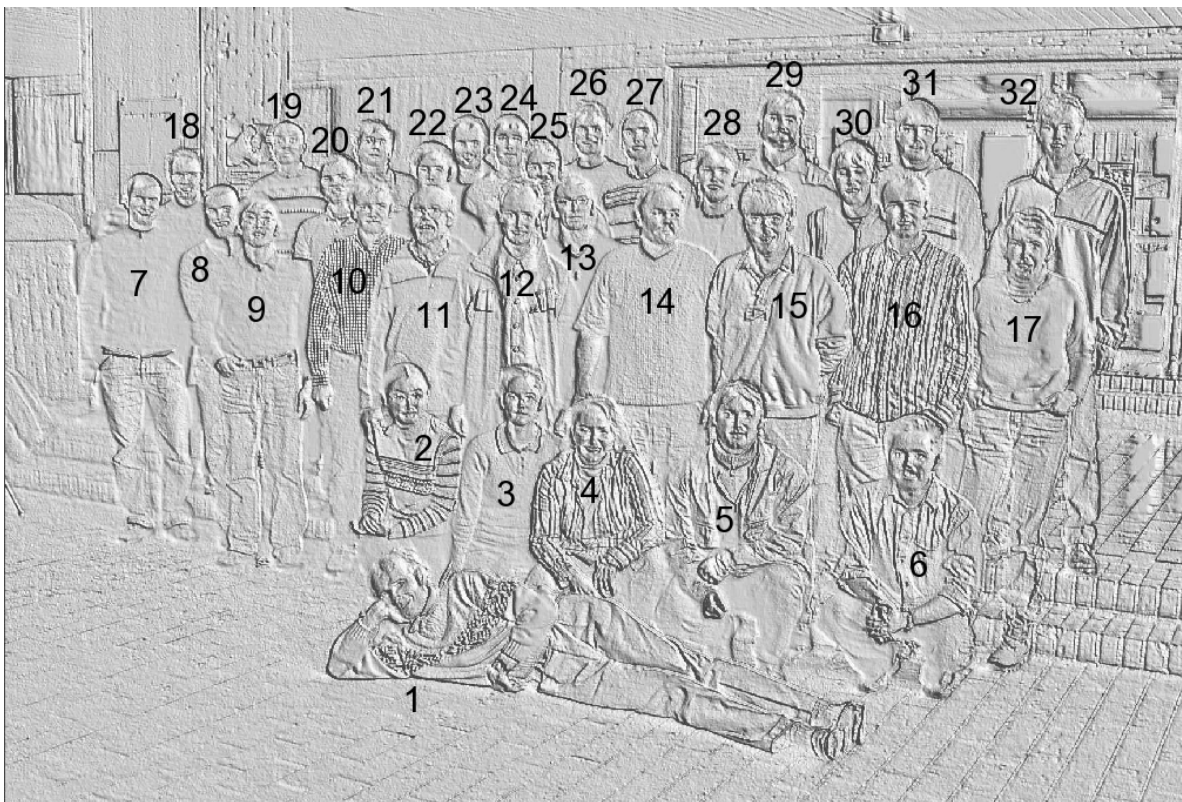
8.14 Guest Scientists

Name	Institute	Duration of stay
Klimko Sergey, Dr.	Institute Laue-Langevin (ILL), France	August 2005 – October 2005

8.15 Guided Tours at FRM-II

The FRM-II is open for everybody to come and visit the scientific and experimental facilities (Experimental Hall and Neutron Guide Hall). Therefore, Guided Tours are organized by a specially established division, the „Besucherdienst“, and conducted by the scientists and the technical personnel of FRM-II.

In 2005, the members of E21 guided approx. 140 officially registered tours and several others at various occasions, thus contributing a significant amount of time and personal effort to help making the Neutron Source FRM-II a publically transparent and accepted research facility.



1	P. Böni	9	Hongyun Li	17	B. Russ	25	E. Calzada
2	Qi Ning	10	C. Hugenschmidt	18	N. Arend	26	T. Brunner
3	V. Kargl	11	R. Repper	19	D. Lamago	27	P. Niklowitz
4	S. Jones	12	N. Wieschalla	20	C. Piochacz	28	S. Mühlbauer
5	W. Häußler	13	T. Hils	21	R. Georgii	29	B. Schillinger
6	S. Valloppilly	14	A. Mantwill	22	S. Legl	30	A. Neubauer
7	M. Janoschek	15	R. Schwikowski	23	D. Streibl	31	C. Pfeleiderer
8	M. Stadlbauer	16	R. Jungwirth	24	J. Mayer	32	K. Lorenz

Missing: M. Axtner, J. Brunner, K. Böning, E. Clementyev, B. Gohla-Neudecker, F. Grünauer, T. Keller, M. Mühlbauer, C. Schanzer, K. Schreckenbach, M. Schulz, S. Stüber, H. Wagensonner

E21 Gallery

Das Jahr 2005 beginnt nicht schlecht, zur körperlichen Ertüchtigung geht es zum Skifahren nach Achenkirch...



...und wie man sehen kann, wir haben Experten in der Gruppe!



Weiter geht es immer bergauf bei E21, das Ziel: der Ross- und Buchstein.

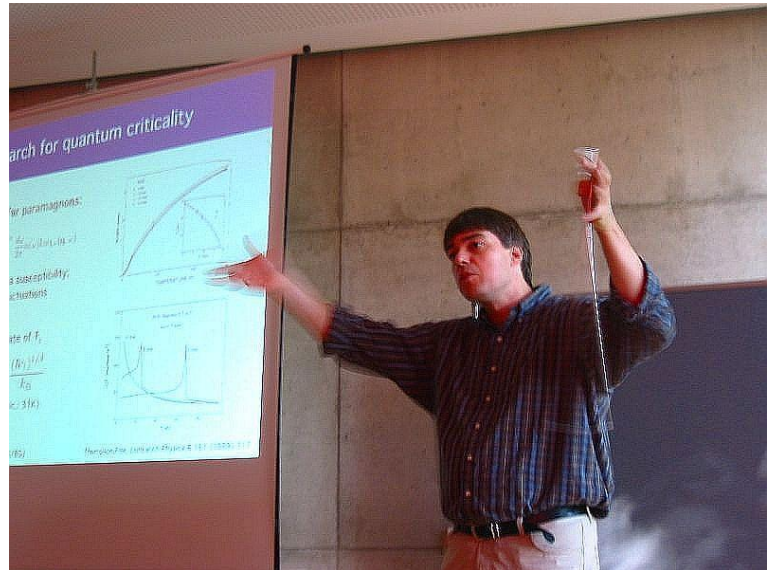
Start am Morgen...



...und so sehen die Experten diesmal aus.

Burg Rothenfels, Juli 2005

„Die Lösung liegt in der dritten Dimension. Wenn wir einige Instrumente anheben und stapeln, dann haben wir genügend Platz!“



Ein gemeinsamer Kegelabend in Garching, zum Jahresausklang.

